ROYAUME DU MAROC
Université Mohammed V - RABAT -
جامعة محمد الخامس – الرباط –
Faculté des sciences
كلية العلوم
CENTRE D'ETUDES DOCTORALES - SCIENCES ET TECHNOLOGIES

N° d'ordre : 3300

THESE

En vue de l'obtention du : **DOCTORAT**

Structure de Recherche : Équipe de Sciences de la Matière et du Rayonnement (ESMaR)
Discipline : Physique
Spécialité : Physique médicale

Présenté et soutenu le 06/03/2020

Par:

Abdelkrim ZEGHARI

Modeling and Simulation of Medical Linear Accelerators Using Monte Carlo BEAMnrc code and Radiotherapy Applications

JURY

Yassine HASSOUNI	PES, Faculté des Sciences, Université Mohammed V-Rabat	Président
Rajaâ CHERKAOUI El MOURSLI	PES, Faculté des Sciences, Université Mohammed V-Rabat	Directrice de thèse
Driss BENCHEKROUN	PES, Faculté des Sciences, Université HASSAN II-Casabanca	Rapporteur/ Examinateur
Yahya TAYALATI	PES, Faculté des Sciences, Université Mohammed V-Rabat	Rapporteur/ Examinateur
Mustapha BOUGTEB	PES, Faculté des Sciences et Techniques, Université Hassan Premier- Settat	Rapporteur/ Examinateur
Abdelmajid MAGHNOUJ	PES, Faculté des Sciences, Université Mohamed Ben Abdellah-Fez	Examinateur

Année Universitaire : **2019/2020**

... To the memory of my mother Aicha... who always believed in me. Miss you. ....To the memory of my father Abdesslam ... To my brothers! ... To my wife! Love you!

...

Acknowledgements

This thesis is realized under direction of my supervisor, Professor Rajaa CHERKAOUI El Moursli, at the " Research Group of Matter and Radiation Science (ESMaR: Équipe de Sciences de la Matière et de Rayonnement)" Faculty of Sciences, Mohamed V University, Rabat.

Firstly, i wish to express my deepest gratitude to my supervisor, Professor Rajaa CHERKAOUI EL MOURSLI. Without her positive attitude towards my initiative on the subject, her advice throughout my research work and her support whenever necessary, this work would never have been completed.

For this dissertation, I would like to thank my reading committee members for their time, interest, and helpful comments:

I would like to thank professor Yassine HASSOUNI from Faculty of Sciences, Mohamed V University, Rabat for accepting to judge my thesis work and being president in my thesis defense.

I would like to thank professor Driss BENCHEKROUN from faculty of Science Ain Chock, Hassan II university, Casablanca for reviewing my thesis report and accepting to judge my thesis work.

I would like to thank the lab director professor Yahya TAYALATI from Faculty of Sciences, Mohamed V University, Rabat for reviewing my thesis report and accepting to judge my thesis work and your encouragement your enlightened advices and your assistance during this PhD period.

I would like to thank professor Mustapha BOUGTEB from Faculty of Science and Technology, Hassan I University, Settat for accepting to judge my thesis work.

I would like to thank professor Abdelmajid MAGHNOUJ from Faculty of Science, Mohamed Ben Abdellah University, fez for accepting to judge my thesis work.

I thank all the members of the ESMaR for their warm welcome and their encouragement their enlightened advice and their effective help us allowed to structure and carry out this project. Also, to everyone else that I might have forgotten. I would especially like to thank Rahal Saadi, Mohamed Majed, and Zakaria. I would also like to thank colleagues and staff who inspired and encouraged me and created a positive work environment.

Last but not the least, I would like to thank my family: To the soul of my mother and my father, to grand father Fatma, to my aunt Roukaya, to my brothers Hoceine and sister Fouazia and family, without you i wouldn't be me and i wouldn't have done this - thank you. Finally, to Bouthaina, my wife, you are the light of my life and fuel for my soul, to all family members for all their love and encouragement.

I did not forget my brother Mhammed and her wife Najoua who helped me and supported me throughout my study. Thank you very much for everything. May Allah keep you my Brother.

Thank you.

Abstract

This work is intended to develop a Monte Carlo simulation which can be used in the calculation and analysis of distribution doses. In this context, we have used the MC BEAMnrc code. This code is originally designed for application of dosimetry in medical physics.

The Monte Carlo BEAMnrc code for medical linear accelerator: 12 MV SATURNE 43, has been validated with a good agreement, within 1.5%/1.5mm for gamma index.

The variance reduction techniques implemented in BEAMnrc/DOSXYZnrc codes in parallel calculation increase importantly the efficiency about 19000 times compared to analog simulation by gaining the time of simulation and reducing the statistical errors.

Two models on flattening filter and free flattening filter modes for medical linear accelerator SATURNE 43 with energy of 12 MV photon mode using the BEAMnrc Monte Carlo user code has been developped. Our results found that percentage depth dose at the depth of maximum dose for free flattening filter mode had an increase by a factor of 3.94-fold increase in the dose rate and a decrease in out of field doses for unflattened beams with 10×10 cm^2 field size.

Finally the dose deposition has been calculated in homogeneous and heterogeneous phantom.

Keywords: SATURNE 43; BEAMnrc; Percent depth dose; gamma index; free flattening filter; VRT; MC.

Résumé

L'objectif de ce travail est de développer une simulation Monte Carlo pour etre utilisée dans le calcul et l'analyse de distribution de doses. Dans ce contexte, nous avons utilisé le code Monte Carlo BEAMnrc. Ce code est a l'origine concu pour l'application de la dosimétrie en physique médicale.

Le code Monte Carlo BEAMnrc a été validé pour l'accélérateur linéaire médical: 12 MV SATURNE 43 avec precision de 1.5%/1.5mm pour gamma indice.

Les techniques de réduction de la variance implémentees dans les deux codes BEAMnrc/DOSXYZnrc ont étée utiliséees pour augmenter considérablement l'efficacité en gagnant le temps de calcul de simulation et en réduisant les erreurs statistiques.

Nous avons également calculé et comparé les distributions de doses pour deux modéles : le premier modéle en utilisant pour la téte de l'accélérateur médical linéaire, un filtre égalisateur et pour le deuxiéme modéle, aucun filtre égalisateur. Nos résultats ont montré que la Distribution de dose en profondeur, a la profondeur de la dose maximale, pour le cas de la téte de l'accélérateur médical linéaire, sans le filtre égalisateur avait une augmentation du débit de dose et une diminution des doses hors champ pour les faisceaux non aplatis (absence du filtre égalisateur) dans le champ de 10×10 cm^2.

Enfin, la distribution de la dose a été calculée dans le cas du fantome d'eau homogene et dans le cas d'existence d'hétérogéneité. Une comparaison de ces deux cas de distributions de dose a été réalisée.

Mots-clés : SATURNE 43; Monte Carlo; Distribution de Dose; gamma indice; BEAMnrc; Sans Filtre Egalisateur; Téchniques de Réduction de la Variance.

Résumé détaillé

Dans ce travail de thèse, on investi à la validation de Monte Carlo BEAMnrc code pour la simulation de la téte de l'accélérateur médical linéaire SATURNE 43. Ce qui inclut le calcul de distrubutions de la dose et le développement du modél validé dans l'étude d'autres caractéristiques dosimétriques de l'accélérateur et la comparaison avec les données expérimentales.

En effet, la physique de la radiothérapie bénéficie énormément des avantages que la méthode de Monte Carlo peut offrir dans l'étude de l'interaction rayonnement matière. Ainsi, durant les trois dernières décennies, plusieurs codes basés sur la méthode de Monte Carlo se sont développés. Nous citons PENELOPE, BEAMnrc,..etc. Récemment et suite à ce développement des codes et à l'amélioration des performances des moyens de calcul, la dernière décennie a connu l'apparition, dans le domaine de la radiothérapie, de ce qu'on appelle la planification Monte Carlo du traitement.

Actuellement, en physique médicale, en particulier dans la radiothérapie, il y a des dispositifs spéciaux utilisés dans le traitement de tumeurs cancéreuses; ces dispositifs sont appelés des accélérateurs médicaux linéaires.

La première version de EGSnrc/BEAMnrc a été développée en 1987 dans le cadre du Projet OMEGA destiné à la réalisation d'un système de planification du traitement 3-D à des fins de radiothérapie.

En effet, depuis quelques décennies, les simulations Monte Carlo pour le transport de rayonnement ont été largement utilisées en dosimétrie et en physique médicale comme alternative aux calculs analytiques. Des résultats très précis sont maintenant obtenus avec ces techniques grâce aux techniques de reduction de la variance et developements des puissants ordinateurs distribuées avec simulation en paralléle. Ces fonctionnalités ont participé à la croissance et à l'évolution rapide de BEAMnrc/DOSXYZnrc dans les applications de physique médical (les accélérateurs linéaires), BEAMnrc dans ses versions récentes joue maintenant un rôle clé dans la conception de nouveaux dispositifs des accélérateurs médicaux linéaires, dans l'optimisation dans les calculs de dose pour la radiothérapie.

C'est dans cette perspective que mon travail de thèse a été consacré principalement au développement d'un modèle de calcul utilisant le code Monte Carlo EGSnrc/BEAMnrc pour la simulation de l'accélérateur médical linéaire SATURNE 43 en mode photon 12 MV. Le modèle développé comprend les principaux composants de la tete de l'accélérateur et un fantôme d'eau.

Les performances des données expérimentales mesurées sont reproduites avec précision par BEAMnrc/DOSXYZnrc, en particulier les données expérimentales concernant la distribution de dose en profondeur, la distribution de dose en latéral.

Le modèle de simulation a été validé avec succès par comparaison avec les distributions expérimentales. Un bon accord entre les simulations et les mesures a été observé au niveau de la distribution de dose en profondeur, de la distribution de dose en lateral, profondeur maximal, index de qualite.

Les techniques de reduction de la variance implementées dans les deux codes BEAMnrc/DOSXYZnrc ont ete utilisees pour augmenter considerablement l'efficacite en gagnant le temps de calcul de simulation et en reduisant les erreurs statistiques.

Nous avons egalement calculé et comparé les distributions de doses et du flux des photons pour deux modeles : avec le premier modéle en utilisant la tete de l'accélérateur médical lineaire complet, et pour le deuxieme modéle, le filtre égalisateur a été retiré de la téte du SATURNE 43. Nos resultats ont montre que la Distribution de dose en profondeur, a la profondeur de la dose maximale, pour le cas de la téte de l'accélérateur médical linéaire, sans le filtre égalisateur avait montré une augmentation du débit de dose et du flux des photons et une diminution des doses hors champ pour les faisceaux non aplatis (absence du filtre égalisateur) dans le champ de 10×10 cm^2.

Grâce au code BEAMnrc, l'accélérateur médical linéaire, SATURNE 43 en mode photon 12 MV, a été simulé et cette simulation a été validé avec un gamma indice 1,5%/1.5mm.

Après une introduction générale, le chapitre I fournit les principales notions de radiothérapie telles que: les différentes téchniques utilisées en radiothérapie externe. Après cela, nous présentons une description générale des accélérateurs médicaux. Le chapitre se concentrera sur l'histoire du linac, la fonctionnalité et les principaux composants d'un accélérateur médical moderne et les principes de fonctionnement des accélérateurs médicaux linéaires. Dans le chapitre II, nous avons généralement décrit les paramètres et les quantités de faisceaux décrits dans le domaine de la radiothérapie, tels que la dose de profil, le pourcentage de dose en profondeur, l'indice de qualité, etc. Ensuite, nous présentons l'interaction des photons avec la matière, l'interaction des particules chargées avec la matière et les propriétés dosimétriques des faisceaux de photons et des particules chargées. Le chapitre III est dédié à la description des principes des simulations de Monte Carlo, Erreurs et incertitudes en radiothérapie, et les critéres de validité et quelques recommendations de validation des résultats obtenus. Ensuite, nous présentons un aperçu des codes Monte Carlo comme EGSnrc, BEAMnrc et DOSXYZnrc, et les bases pour comprendre les concepts d'une simulation Monte-Carlo et nous décrivons les différentes techniques de réduction de variance mises en œuvre dans les codes BEAMnrc et DOSXYZnrc. Dans le chapitre IV, les calculs de simulation et leur validation par comparaison avec des données expérimentales fournit par le national laboratoire Henri Bequerel en France, ou nous avons utilisé une nouvelle méthodologie pour ajuster les paramètres du faisceau de photons 12 MV produit par l'accélérateur SATURNE 43. Enfin, dans le chapitre V, une fois ces paramètres définis, nous avons étudié les différentes techniques de réduction de la variance mises en œuvre dans les deux codes BEAMnrc/DOSXYZnrc pour gagner en efficacité et spécifiquement lorsque nous avons utilisé la simulation en parallèle. Après cela, nous avons étudié l'effet du filtre d'aplatissement pour augmenter la dose au profondeur et diminue la dose hors champs. Enfin, nous avons appliqué le modèle créé à la détermination du pourcentage de dose en profondeur et du profil de dose dans un fantôme d'eau homogène et un fantôme d'eau hétérogène.

Les résultats obtenus peuvent être utiles pour la conception et l'amélioration des accélérateurs médicaux linéaires.

Mots-clés : SATURNE 43; BEAMnrc; gamma indice; distribution de dose; technique de reduction de la variance; accélérateur médical linéaire.

Contents

List of Figures

List of Tables

List of Abbreviations

BEAMnrc : A user-code for Monte Carlo simulations of medical accelerators linear
DOSXYZnrc : A user-code for Monte Carlo calculations of 3 dimensional dose distributions
EGS4 : Electron Gamma Shower version 4, a Monte Carlo code system
OMEGA : Ottawa Madison Electron Gamma Algorithm
PEGS4 : Preprocessor for EGS4
MCNPX : Monte Carlo N-Particle eXtended
PENELOPE : PENetration and Energy LOss of Positrons and Electrons
LNHB : Laboratoire National Henri Becquerel
CEA : Commissariat à l'Energie Atomique et aux énergies alternatives
AAPM : American Association of Physicists in Medicine
IAEA : International Agency for Energy Atomic
ICRU : International Commission on Radiation Units and Measurements
ESTRO : European Society for Therapeutic Radiology and Oncology
NACP : Nordic Association of Clinical Physics
IEC : International Electrotechnical Commission
MC : Monte Carlo
IEC : International Electrotechnical Commission
IMRT : Intensity Modulated Radiation Therapy
MLC : Multi Leaf Collimator
kV : kiloVoltage
MV : MegaVoltage
SMLC : Segmented Multi Leaf Collimator
DMLC : Dynamic Multi Leaf Collimator
IMAT : Intensity Modulated Arc Therapy
TBI : Total Body Irradiation
SRT : Stereotactic RadioTherapy
TSEI : Total Skin Electron Irradiation
IORT : Intra-Operative RadioTherapy
IGRT : Image-Guided RadioTherapy
MVCT : MegaVoltage Computed Tomography
BIMP : Bureau International des Poids et Mesures
RGS : Respiratory Gating System
CT : Computed Tomography
Linac : Linear Accelerator
CM : Component Module used in BEAM to define a specific class of geometric shape
CPE : Charged Particle Equilibrium
ESAVE : maximum charged particle energy (in MeV) at which range rejection is considered in E
ESTEPE : the maximum fractional energy loss per electron step in EGS simulations
PCUT : Cutoff energy for Photons in Monte Carlo simulations using EGS4 code (MeV)
ECUT : Cutoff Energy for Electrons in Monte Carlo simulations using EGS4 code (MeV)

DP : Dose Profile
PDD : Percentage Depth Dose
FWHM : Full Width at Half Maximum
PHSP : PHase SPace
VRT : Variance Reduction Technique
DBS : Directional Bremsstrahlung Splitting
SBS : Selective Bremsstrahlung Splitting
UBS : Uniform Bremsstrahlung Splitting
FS : Field Size
SSD : Source-Surface-Distance
FF : Flattening Filter
FFF : Free Flattening Filter
TPR : Tissue Phantom Ratio
PMMA : Poly Methyl MethAcrylate

General introduction

The physics we will talk about came into being on Friday 9 November 1895 at the University of Wuerzburg, when Mr Wilhelm Roentgen had really payed attention to a mysterious phenomenon. The new invisible radiations so named x-rays were electrically neutral. The X-ray particles are more energy and much more penetrating in matter [1]. In medical imaging, x-rays have been used to visualise the structure of tissues in living bodies including cancer cells. Mrs Roentgen could verify this when she saw the bones of her own left hand, with the ring she wore on her finger, on a photographic plate developed by her husband [1] (figure 1).

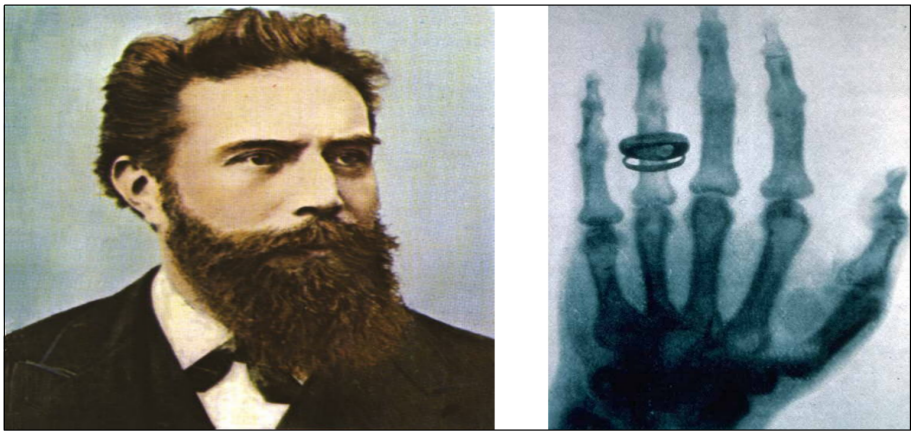

FIGURE 1: Left, Wilhelm Conrad Roentgen and right, the x-ray image of the hand produced in 23 January 1896. [2]

In 1928, the dosimetry was defined as the quantity of x-radiation for the second meeting of the International Commission on Radiation Units (ICRU) saying that: This international unit be the quantity of x-radiation [3]. The x-rays caused the first radiological accidents because of the incomplete knowledge about it properties [4]. This radiological accidents of ionizing radiation led in 1928 to the first meeting to create the International Committee for the Protection of X-rays and Radium, now known as the International Commission on Radiological Protection (ICRP). After that, in 1937 the unit of dosimetry was named the roentgen with the symbol r, and in 1962 ICRU was changed to R [5, 6].

The early treatment machines were built and developed in the 1930s and 1940s. This technology developement was carried and proceeded by cyclotron, betatron and microtron accelerators, which produced the higher electron energies. In 1930, the cyclotron was created and developed by E.O. Lawrence for acceleration of ions to a few megaelectronvolts [1]. Then in 1940, the betatron accelerator was developed by D.W. Kerst as a cyclic electron accelerator in the field of physics research [1]; however, its utilization in radiotherapy field was realized after that. In 1944, the microtron accelerator was built and developed by V.I. Veksler and is used in modern

radiotherapy. The microtron is an electron accelerator that combines the features of a linac with a cyclotron [7]. In 1953, The first patient was treated using a medical linear accelerator (linac) in London, so the use of these machines in clinical practice has been almost co-existent with the lifetime of physics in medicine and biology [8]. The accelerator with microwave have been become the standard linac in radiotherapy (Thwaites and Tuohy 2006) [9]. The advanced techniques associated with research in biology and physics have made it possible, among other things, to considerably improve tumor control in external radiotherapy while preserving peripheral healthy tissue. The irradiation of the patients, first defined by a time of exposure, then by a delivered dose and a fractionation, was optimized. Low-energy treatments using telecobalts (Figure 2-a) and linear accelerators as we know them today (Figure 2-b).

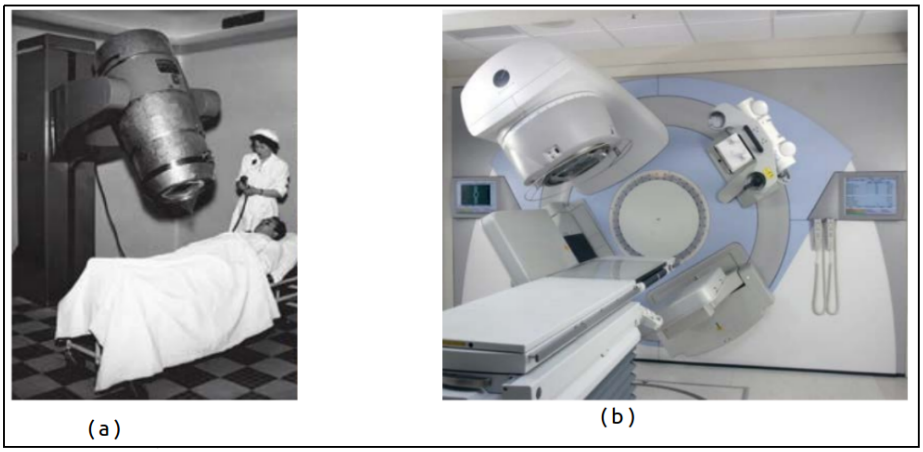

FIGURE 2: Evolution of treatment techniques in radiotherapy (a) Cobalt-60 treatment (b) Linear electron accelerator (Synergy, Elekta).

Furteremore, we note that Hadron therapy is also emerging and it has been proven to be suitable for treatment of some neoplasms [9,10].

The particles physics has made an important contribution to the development of research study in the different fields of biomedical, diagnosis, and therapy. This is particularly, since the discovery of x-rays and other types of radiation as protons and neutrons at the end of the 19th century for medical imaging, brachytherapy and radiotherapy [9,10]. Indeed, the curative role of ionizing and non-ionizing radiation in the treatment of cancers has been exploited since many years ago. Radiotherapy, also known as radiation therapy, is a treatment modality based on the use of high energy rays or radioactive substances, to damage tumoral cells and to halt their growth and division. Medicine has used radiation therapy as a treatment for cancer for more than 100 years, with its earliest roots traced from the discovery of x-rays in 1895 by Wilhelm Roentgen [1].

Data handling, simulation and computer tools developed by physicists have also found use in the medical physics field, for example in establishing personalized treatment plans for cancer patients and biomaterial to treat and kill cancerous cells. Particle physics collaborations, for example at CERN, have brought together part of thousands of scientists from every laboratories of the world to work on the largest and most complex experiments. This mode of working has become second nature for particle physicists, who have learned to work collectively towards a common

goal and who rely on consensus to take decisions. This can serve as a model for emerging multidisciplinary in medical physics applications, like radiotherapy and nuclear medicine. So, the transfer of technological innovations to the health care in nuclear medicine, was contributed to well understand their relevance for medical research community.

Cancer is now considered as one of the major diseases affecting people in the developing countries. Radiotherapy is considered as one of the major modalities for cancer treatment. Radiotherapy treatment planning has several stages and making it as a complex process which can represent many potential risks on patient. So that, requires various sources of data and informations about the patient and treatment equipment, interaction of various radiotherapy professionals such as physicians, physicists, and technicians. The dosimetry calculation made during the treatment planning differs from manufacturers to others according to the calculation protocols, the algorithms used, and the processing parameters introduced. It is important to ensure that the dose calculated by the treatment planning software corresponds to the measured dose, under all geometric conditions of the irradiation beam. Because of potential errors that may lead to either under-dosing that results from tumour recurrence or overdose that can lead to health complications after treatment. A dose check is recommended before any treatment.

The evolution of radiotherapy techniques allows a progress in the development of treatment plan. This treatment plan defined in a sophisticated way, all the beam parameters to be applied for patient to completely destroy his tumour, consisting of cancerous cells. So, the goal was to ensure the tumour sterilization and saving the healthy tissue. Therefore, the clinical application of such techniques requires a reliable estimate of the absorbed dose distributions to ensure the compromise of the need to sufficiently irradiate cancerous tissue and avoid to irradiate neighbouring healthy tissues. On that occasion, patient dosimetry then becomes the stage where treatment planning can be evaluated, experimentally verified, and finally validated. This step must be based on the processes of measuring and calculating the absorbed dose. The current techniques for performing the treatment schedules, involves the software known as Treatment Planning Systems (TPS). The purpose of this software TPS is to provide radiotherapists with a practical solution that can be used in clinical practice. The problem is that to obtain these results in sufficiently reasonable times, this software uses rapid analytical algorithms to optimize the speed but affecting the accuracy of calculations. Estimating the dose delivered with these TPS is sufficient for most treatments.

In parallel with the solutions used in TPS, there are other methods allowing to know in a very exact way, the dose distribution of a patient irradiation, like the methods of Monte Carlo (MC). MC methods are increasingly utilized for clinical treatment planning in situations, where conventional analytical methods are not sufficient. The MC codes implementated for radiotherapy are generally divided the calculation into two steps: the first step includes the simulation of the head of the processing machines, this part being fixed and independent of the associated planning with patient treatment, At the exit of the treatment head a phase space (PHSP) file can be registered and reused; The second step is to track the particles from the PHSP file previously recorded in the first step, This approach is adopted in our model application of the general MC BEAMnrc code in external radiotherapy.

The use of a MC technique for radiotherapy requires a high level of experimental verification and validation of the code regarding modelling of the treatment head by comparisons with depth yields and dose profiles absorbed at various depths of a water phantom.

All simulation results reported in this study were performed with the EGSnrc code based BEAMnrc and DOSXYZnrc packages for transport of electron, positron, and photon particles. EGSnrc is an improved and developed version of the EGS4 code. BEAMnrc code can be explored for the simulation of radiotherapy treatment units and can produce the matched data close to the realistic clinical beams. The BEAMnrc code has initially been designed to simulate radiation beams from any radiotherapy source (accelerators), including low-energy x-rays, Co-60 units, and both photon and electron beams. It has been extensively benchmarked against measured dose distributions for a variety of accelerators and good agreement was obtained for central-axis percentage depth dose and profile dose.

DOSXYZnrc is utilized to calculate the three dimensional (3D) absorbed dose distributions inside a water phantom formed of rectangular cartesian voxel. It can simulate the particle transport in a 3D volume and scores the deposited energy in all the designated voxels. The output of a DOSXYZnrc calculation is a file that stores the calculated 3D dose distribution data and the corresponding dose uncertainties. The calculated dose are normalized per incident history. STATDOSE is a utility program provided in the EGSnrc software package which can be used to analyze these 3D dose files.

Thesis outline

During this thesis, we were interested in the study of dosimetry parameter using medical linear accelerator 12 MV SATURNE 43. For the simulation of SATURNE 43 accelerator, the geometrical specifications as well as the experimental results were delivered by the LNHB (National Laboratory Henry Becquerel). The main aim of this thesis is to develop a MC simulation based on the BEAMnrc and DOSXYZnrc codes that can be used in the calculation and analysis of dose distributions that are essential for planning radiotherapy treatment. The traditional approach for this kind of study is to model, first, the different components of the linear accelerator head with BEAMnrc code. After that, we modeled the water phantom geometry with DOSXYZnrc code to calculate the percentage depth dose and profile dose.

The manuscript thus proposed is divided into five chapters:

Chapter 1: It provides the main notions of radiotherapy such as: a literature of diverse techniques used in external radiotherapy; a general description of medical linacs. So this chapter will focus on history, functionality, and main components of a modern medical linac.

Chapter 2: It represents the different interactions between mater and pincident beam of photons and charged particles. It describes the dosimetric properties of the beam of photons and charged particles. Then, this chapter describes the beam parameters and quantities described external photon beam in radiotherapy field such as profile dose, percentage depth dose, tissue phantom ratio...etc.

Chapter 3: In this chapter, we represent the Monte Carlo principles, errors and uncertainty in radiotherapy, and the gamma index method. After that, an overview

on the Monte Carlo codes as EGSnrc, BEAMnrc, and DOSXYZnrc. After that, we conclude this chapter by describing the different variance reduction techniques and approximate efficiency improving techniques implemented in BEAMnrc/DOSXYZnrc codes.

Chapter 4: In this chapter, we discuss a new methodology to adjust the initial parameters of 12 MV photon beam produced by SATURNE 43 accelerator, through the comparison of Monte Carlo dose distribution in a homogenous water phantom with expeimental results provided by LNHB in France.

Chapter 5: In this chapter, we investigate different variance reduction techniques and approximate efficiency improving techniques implemented in BEAMnrc and DOSXYZnrc to gain efficiency and specifically when these techniques are combined in parallel simulation. After that, we studied the effect of free flattening filter to the increase of the dose distribution on a homogeneous water phantom. Finally, we applied the first model of SATURNE 43 created for validation of percentage depth dose and profile dose in a homogeneous water phantom to a heterogeneous water phantom with four physic model configurations (A, B, C, and D).

Chapter 1

Radiotherapy Techniques and Particle Accelerators

1.1 Introduction

Radiotherapy is a branch of medical physics which contained a radiation therapy, therapeutic radiology or radiation oncology. It is in the process of a continuous change. Besides computer science development, other disciplines, like neurosurgery, radiological diagnostics, physics, mathematics as well as electronic engineering, had a strong impact on radiotherapy. It uses ionizing radiation to destruct cancerous cells. It can be applied as external radiotherapy where the dose is delivered by an external source of radiation (photons, protons, or other ions) or the radiation source is inserted inside the patient [11–13].

Radiation dose is designed to conform to the three-dimensional (3D) shape of the tumour to minimize radiation exposures to surrounding healthy tissues. Using intensity modulated radiation therapy (IMRT), in which a multileaf collimator (MLC) is used to change the intensity of the radiation beams [13–15]. Improvements in computation techniques, such as MC simulations, have made it possible to compute accurately the dose given to the tumor and the surrounding organs. MC calculations are widely accepted as being the most accurate way to predict the dose delivered to a patient [16,17]. Radiotherapy can be divided into two distinct types, depending on the location of the radiation source: for external radiotherapy, the source is located at a distance from the surface of the patient, as example, teletherapy units [18]; for internal radiotherapy the small sealed sources are inside the patient body (example source Cs-137, Ir-192...) [19, 20]. There are other modes of cancer therapy such as surgery, metabolic therapy and chemotherapy.

In the second part of this chapter, we describe the medical accelerators: in the last past 60 years the manufacturer have been developped the medical linacs through various steps from the first generation to the five generations. This linac generations have the following component: target; flattening filter; scattering foils; symmetric jaws; asymmetric jaws; ionization chamber; fixed wedge; dynamic wedge; MLC.

1.2 Radiotherapy techniques

1.2.1 Radiotherapy conformational 3D

Conformal radiotherapy, as proposed by Takahashi as early as 1965 [21], is more becoming reality in clinical practice. The conformal radiotherapy is an advanced technique and is based on 3-D target localization, 3-D treatment planning and 3-D dose delivery techniques. Treatment planning is achieved either with standard uniform intensity beams shaped to the target, or, with intensity modulated beams to improve target dose homogeneity and spare healthy tissue. The IMRT technique is currently the most advanced form of conformal radiotherapy and holds great promise for improving radiotherapy. IMRT treatments have been began to be used clinically since the 1960s with wedges and physical compensator. Modern clinical IMRT with MLC became possible in the latter part of the 1990s. IMRT treatments can be delivered with the MLC operating in one of three basic modes:

¶Segmented MLC or static IMRT; The intensity modulated fields are delivered with a sequence of small segments or subfields, which each subfield had an uniform intensity. The MLC dont move during the irradiation of the tumour.

¶Dynamic MLC or dynamic IMRT mode; The intensity modulated fields are delivered in a dynamic fashion with the leaves of the MLC moving under a computer control during the irradiation of the tumour.

¶Intensity modulated arc therapy (IMAT); The gantry rotates around a patient. IMAT should result in the most conformal dose distributions possible with standard linac hardware.

1.2.2 Total body irradiation(TBI)

TBI is a radio-therapeutic technique that produces a uniform dose within$\pm$10% of the prescribed dose to a patient's whole body [22]. The treatment concepts of whole body irradiation encompass all irradiations with large photon fields except for a sensitive organs which are partially or fully shielded. Megavoltage photon beams (linac); Co-60 rays or megavoltage X-rays, are used for this objective. TBI techniques can be divided to four sorts: High dose TBI in three days (total dose 1200 cGy); Low dose TBI, with dose delivery in 10-15 fractions of 10-15 cGy each; Half body irradiation, with a dose of 8 Gy delivered to the upper or lower half body in a single session; Total nodal irradiation delivered in 20 fractions a typical dose of 40 Gy. The TBI techniques use the statics beams with field sizes of 70×200 cm^2 encompassing the whole patient body, or moving beams in some sort of translational or rotational motion to cover the whole patient body, with smaller field sizes. TBI treatment techniques are carried out with modified conventional radiotherapy equipment.

1.2.3 Stereotactic radiosurgery

The history of stereotactic radiosurgery technique starts, after some experiments in the 1950s and 1960s. A few decades ago, the widespread existence of linacs had contributed to its investigations for single fraction stereotactic radiosurgery and radiotherapy [23]. Stereotactic irradiation or focal irradiation techniques that deliver

a prescribed dose to preselected and stereo-tactically localized lesions. Since 1990, beam shaping is predominantly being achieved by the use of high-definition MLC (micro-MLCs). The dose may be produced through a stereotactic implantation of radioactive sources or with one or several external radiation sources. Stereotactic external beam irradiation is classified into [24]: stereotactic radiosurgery (total dose is delivered in a single session) and stereotactic radiotherapy (total dose is delivered in multiple fractions).

1.2.4 Total skin electron irradiation (TSEI)

TSEI is a special technique used to irradiate the patient's whole skin [25]. All TSEI procedures are focused on electron linacs for conventional radiotherapy. During TSEI, some zones of the patient's skin (such as eyes) must be protected by shielding it and photon contamination generated should be known accurately. The clinical TSEI procedures are governed by three categories of specification: A physical specification (field size of 80 $\times$ 200 cm^2, dose uniformity at z_{max} for at least 80% of the central nominal field area, nominal SSD of 300-500 cm, beam energy at the waveguide exit window of 6-10 MeV, beam energy on the phantom surface of 4-7 MeV, photon contamination of the electron beam); A physical specification of the dose distribution resulting from the superposition of multiple stationary electron fields (dose rate at z_{max} on the central ray, bremsstrahlung contamination dose rate at the level of the umbilicus); Clinical specifications (dose fractionation regimen, total body photon dose irradiated the patient, prescription for all special shielding such as eyes, nails, ...etc.).

1.2.5 Intra-operative radiotherapy (IORT)

IORT is a special radiotherapeutic technique that delivers a radiation dose in a single session between 10 Gy and 20 Gy to a surgically irradiated internal organ. The first treatment units used IORT were superficial and orthovoltage X ray units. IORT used two combined conventional modalities surgery and radiotherapy to destroy cancer cells. Morever, IORT can be applied as part of a treatment protocol with a chemotherapy and external beam radiotherapy modalities [26]. Most current IORT techniques are focused on electron beams issued from megavoltage linacs, because electrons presente various benefits over x-rays for the objectives of IORT : electron dose is deposited over a precise range, thus protecting tissue downstream from the target; The dose can be delivered homogeneously throughout the target volume; There is not much difference in absorption of megavoltage electron beams between the tissue and bone.

1.2.6 Endocavitary rectal irradiation

Endocavitary rectal (endorectal) irradiation technique was introduced in the 1930s by Chaoul and subsequently ameliorated and experienced by others, most notably Papillon [27]. The principal physical requirement for the technique to be successful is that the X-ray beam should have a low energy, showing a PDD in tissue of 100% on the surface and about 50%, 30% and 10% at depths of 5, 10 and 25 mm, respectively.

Two techniques have been used for endorectal treatments: short SSD technique, with the SSD of the order of 4 cm; long SSD technique, with the SSD of the order of 20 cm.

1.2.7 Proton beams in radiotherapy

There is an important worldwide interest of the research centers on introducing of proton beams with energies ranging between 200 and 250 MeV to treat cancer in the medical field. Cancer treatment with proton beams have many advantages such as favorable depth dose properties, characteristic of high ionization density, and weak scattering. Considerable technological amelioration and development have been made in the utilization of protons beams [28]. Proton linear accelerators are capable to produce an adequate irradiation beam, with a similar principle of functioning as the electron accelerators already widely utilized in medical applications. However, with recent development technology and high cose for proton linear accelerator, proton circular accelerators play the best solution in the fields of atomic and nuclear physics research (Cyclotron, Synchrocyclotron, Synchrotron).

1.2.8 Image guided radiotherapy (IGRT)

currently, it has become possible to image patient anatomy just before generating a fraction of radiotherapy, thus gaining accurate knowledge and information on the location of the target volume. This technique of the dose delivered to the patient is defined as IGRT and has the advantage, that the relative localisations of the target volume and some reference point for each fraction are similar to the treatment plan [29]. All image-guided systems allow pretreatment depicting imaging directly after a patient is localized on the linac treatment table for therapy. The IGRT systems are based on immediate implementation and integration of the following systems: kilovoltage or megavoltage imaging system with an isocentric medical linac referred to as cone beam computed tomography (Elekta Synergy and Varian Trilogy models); Megavoltage computed tomography (MVCT) with a tomotherapy machine; 2-D or 3-D ultrasound imaging system integrated with an isocentric medical linac (Nomos BAT and BrainLab ExacTrac system); on-line imaging with paired orthogonal planar imagers with a miniature linac (CyberKnife system).

1.2.9 Adaptive radiotherapy

A full implementation of IGRT will create the notion of adaptive radiotherapy [30]. The current radiotherapy practice relatively wide margins are added to tumour volumes on compensating the respiratory movement influences on tumour dose deposition. 4-D imaging technology is required to take account of organ moving during treatment, which allows direct viewing of volumetric CT images changing over-time. The respiratory gating system (RGS), which is a particular accessory added to a linac to compensate automatically the respiratory motion influence on external beam radiotherapy. Varian developed an RGS that is a real time position management RGS and is applicable to any organ to respiration induced movement, such as the breast, lung and pancreas. The target mobilization is correlated with

external markers movement in simulation and these markers are then investigated in the treatment to control appropriate beam-on times to limit treatment to those time periods when the target is static.

1.3 Particle accelerators

Various types of accelerators have been built for basic research in nuclear and high energy physics, and most of them have been modified for at least some limited use in radiotherapy. In the last past 60 years the manufacturer have been developped the medical linacs by many steps from the first generation to the five generations, making an important amelioration in the machines extremely sophisticated in comparison with the machines of the 1960s [31]. Accelerators are classified into two families: Accelerators with circular trajectories and linacs, or accelerated particles move along a straight path.

1.3.1 Circular accelerator

In 1930, E.O. Lawrence developed the circular accelerators for acceleration of charged particles to a kinetic energy of a few megaelectronvolts (MeV) [32]. In the first time, the accelerators were used for basic nuclear physics researchs, after many years this accelerators had produced the radioisotopes in nuclear medicine as well as protons and neutrons beams for radiotherapy. When the charged particles are injected into a uniform magnetic field which had a direction perpendicular to that of particle's velocities, it undergoes the magnetic field in a circular trajectory in a perpendicular plane to this magnetic field. An accelerated charged particle emits energy in form of radiation when it changes direction. Figure (1.1) describes the effect of magnetic field on a charged particles.

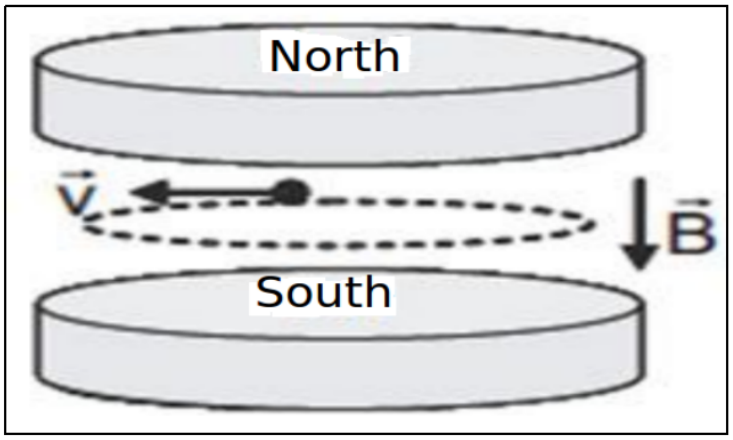

FIGURE 1.1: effect of magnetic field on a particle charged.

1.3.1.1 Cyclotrons

They consist of a single bending magnet whose diameter can reach several meters. The trajectory of the particles is spiral guided inside two evacuated half

cylindrical electrodes (as D shaped form) by a uniform magnetic field (1 T). Inside the electrodes there is no electric field and the particle drifts under the influence of the magnetic field in a semicircular orbit with a constant speed until it crosses the gap again. If the electric field has reversed its direction, the particle will again gain a small part of energy and drift in the other electrode along a semicircle of a larger radius resulting in a spiral orbit and an increase in kinetic energy after a large number of gap crossings. See the figure 1.2 below.

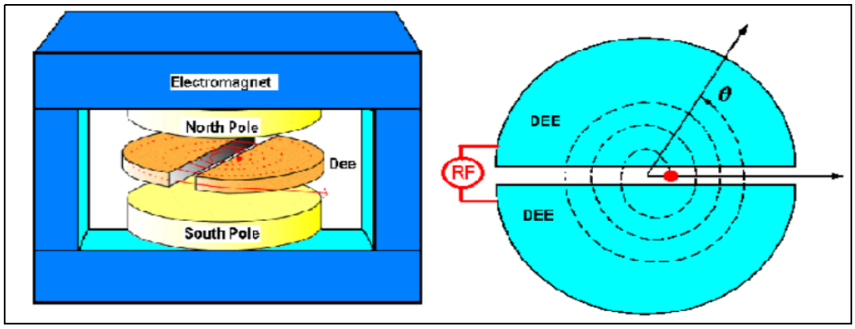

FIGURE 1.2: Schematic layout of a cyclotron, showing two dees, driven by an RF power source.

1.3.1.2 Betatron

D.W. Kerst was developed the betatron accelerator in 1940 as a cyclic accelerator in the filed of physics research [33]. The machine consists of a magnet field, that makes the electrons circulate in a toroidal vacuum chamber which placed into the gap between two magnet poles. The electrons are accelerated by the electric field induced by the changing magnetic flux in the magnet. The electron are kept in a circular orbit by the magnetic field. After 1950 the betatrons played an essentiel role in megavoltage radiotherapy. However, with the development of linacs made them into oblivion because of the various benefits presented by linacs over betatrons : the linacs are much higher beam output (up to 10 Gy/min for linacs versus 1 Gy/min for betatrons); the linacs have a larger field size than betatron.

1.3.2 Linear accelerator

Linear accelerators (also commonly called linac) are the oldest accelerators. They appeared in 1928 with the Wideroe linear accelerator in the United States [34]. There are several acceleration techniques used in linac [34,35].

1.3.2.1 Wideroe type accelerators

The beam passing through a series of cavities where there is an alternating electric field will be able to reach an energy of a few hundred MeV. Figure 1.3 shows the basic principle of a Wideroe accelerator [34].

Cylindrical electrodes are alternately connected to the poles of the high frequency generator. Their length is increasing from the source of ions to the target.

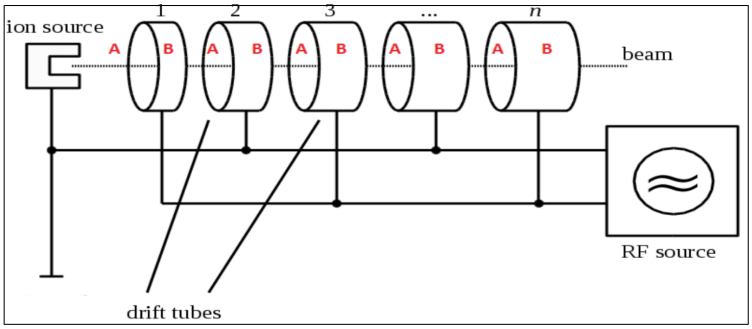

FIGURE 1.3: Schema of a Wideroe accelerator [34].

1.3.2.2 Electrostatic accelerators (Cockcroft-Walton, Van de Graaff)

A high static voltage is applied between two electrodes thus producing an electric field, the kinetic energy acquired by the particles is equal, in electron volts, to the potential difference [35].

1.3.2.3 Acceleratrice section of an electron linear accelerator

Electrons are the charged particles, that the principle of its acceleration is therefore similar to that of ions, through the use of an electromagnetic field. By accelerating electrons, they reach very fast constant speeds. From 2 MeV of kinetic energy, the electron speed was 98% of the celerity of light. Figure 1.4 shows the acceleratrice section forming the electron linac.

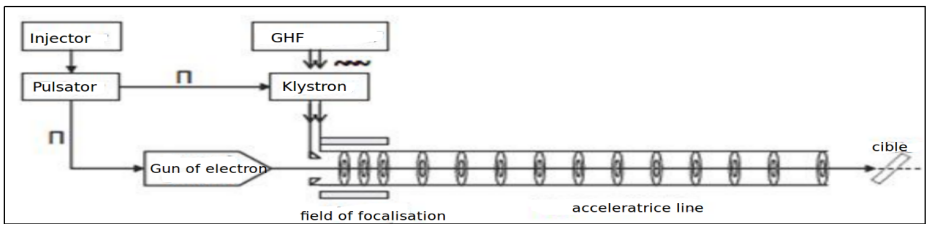

FIGURE 1.4: Schema of acceleratrice section of an electron linac.

The main components of linac are illustrated schematically in figure 1.5 with a brief description of beam production from the creation of radiofrequency signal through the acceleration of electrons in the waveguide to the final shaping of the radiation in the linac head. The beam produced by linac may be divided into two sections: the electron accelerating part and the beam transport part. The electron accelerating part is responsible for the creation of high energy (several MeV) electron pencil-beam, while the beam transport section transports the pencil-beam into a clinical photon or a clinical electron radiation beam.

The linac accelerates the charged particles by passing them through a series of oscillating electric potentials along a linear beamline. The head's linac are formed of general components . However, there are significant variations for the different commercial machines, depending on the final beam kinetic energy as well as on the particular design used by the manufacturer. The essential components of the recent medical linac are generally grouped into: injection system; RadioFrequency (RF)

power generation system; accelerating waveguide; beam transport system; beam collimation system; auxiliary system.

In a medical linac, electrons are generated by klystrons and electromagnets and accelerated through microwaves. These electrons bombard a metal target, usually tungsten, causing a shaped beam of x-rays. The numerous configurations for recent isocentric linacs are shown below in figure 1.5.

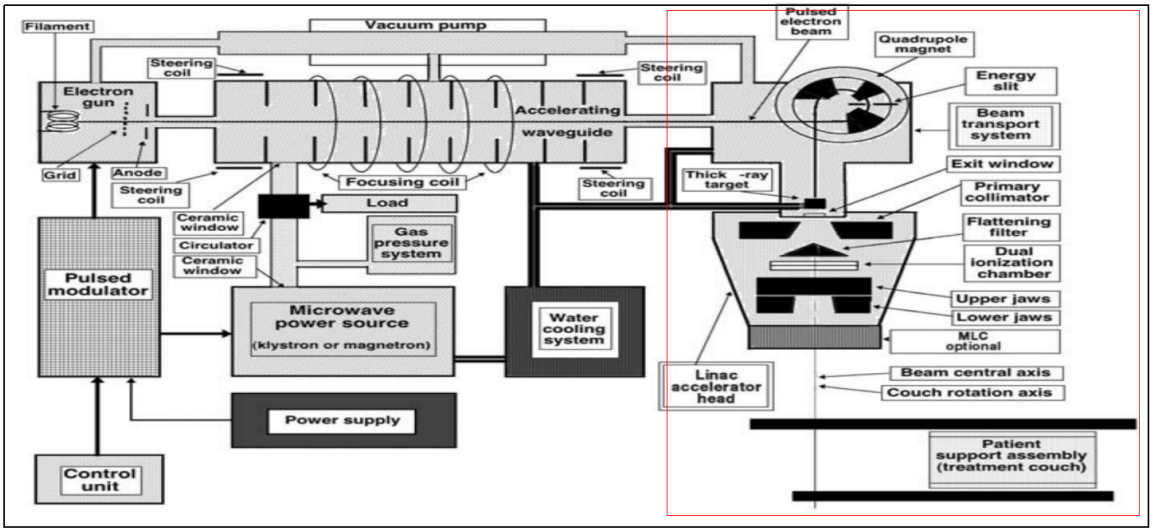

FIGURE 1.5: A complete design of medical linac fonctioning [36].

♣ Injection system

Injection system is the electron gun which is the source of electrons. The electron acceleration begins from an electron gun. The electrons start out attached to the molecules in a plate of barium aluminate or thorium. The electrons are emitted on heating the cathode from the electron guns. When the electrons arrive at the gate, they become attracted even more strongly by the anode. The anode is a torus-shaped to create an electromagnetic field that guides most of the electrons into the next part of the accelerator. There are two sources of electron gun in medical linacs:

¶diode: it consists of a heated filament cathode and a perforated grounded anode. The electrons are produced in the heated cathode and accelerated towards the perforated anode. The electrostatic fields is used to accelerate the electrons inside the diode gun.

¶triode (see figure 1.6): it contains a heated filament cathode and a perforated anode. The electrons are thermionically produced in a heated cathode.

Figure 1.7. shows a design configuration for isocentric medical linacs with the following difference: In figure 1.7.a, the electron gun and target are permanently embedded into the accelerating waveguide, and the RF power generator is mounted in the gantry. In figure 1.7.b, the accelerating waveguide is in the gantry parallel to the isocentre axis, the electrons are brought to the movable target through a beam transport system, and the RF power generator is located in the gantry stand. In figure 1.7.c, the accelerating waveguide and RF power generator are located in the gantry stand, the electrons are brought to movable target through a beam transport system.

FIGURE 1.6: Removable electron triode gun for a typical high energy linac [37].

♣ Radiofrequency power generation system

RF power generation system is necessary for pulsed operation inside the medical accelerators to accelerate the electrons to the desired kinetic energy through two major components:

¶ The principle of RF power source is the using of electron acceleration and deceleration in a vacuum for the production of high power RF fields. It contains two devices (magnetron and klystron): A magnetron contains an electron tube that accelerates the electrons, it is preferred for lower electron energies, 4 MeV to 6 MeV linacs. klystron is used in High Energy Physics (HEP) and 6 MeV medical linacs. It accelerates or decelerates the electrons in the input cavity.

¶ A pulsed modulator is responsible for the production of high voltage ($\sim$ 100 kV), high current ($\sim$ 100 A), short duration ($\sim$ 1 s) pulses required by the RF power source and the injection system.

♣ Accelerating waveguide

Waveguides are gas filled metallic structures used in the transmission of microwaves. Two types of waveguide used in linacs:

¶ RF power transmission waveguides; power transmission waveguides transmit the RF power from the power source to the accelerating waveguide.

¶ Accelerating waveguides; the electrons are accelerated inside the accelerating waveguide by means of an energy transfer from the high power RF fields.

Two types of accelerating waveguide for the acceleration of electrons:

¶ Traveling wave structure; favored by Elekta (formerly also ABB/Dynaray and Philips). These structures need to be physically longer to achieve the same output energy. The microwaves enter the accelerating waveguide on the gun and propagate towards the high energy end of the waveguide. After the first 30 cm, the waveguide are traveling at velocities close to c. This first part of the guide is called the buncher section. In the buncher, the electrons are brought together in space, phase and velocity as they acquire energy from the electromagnetic fields.

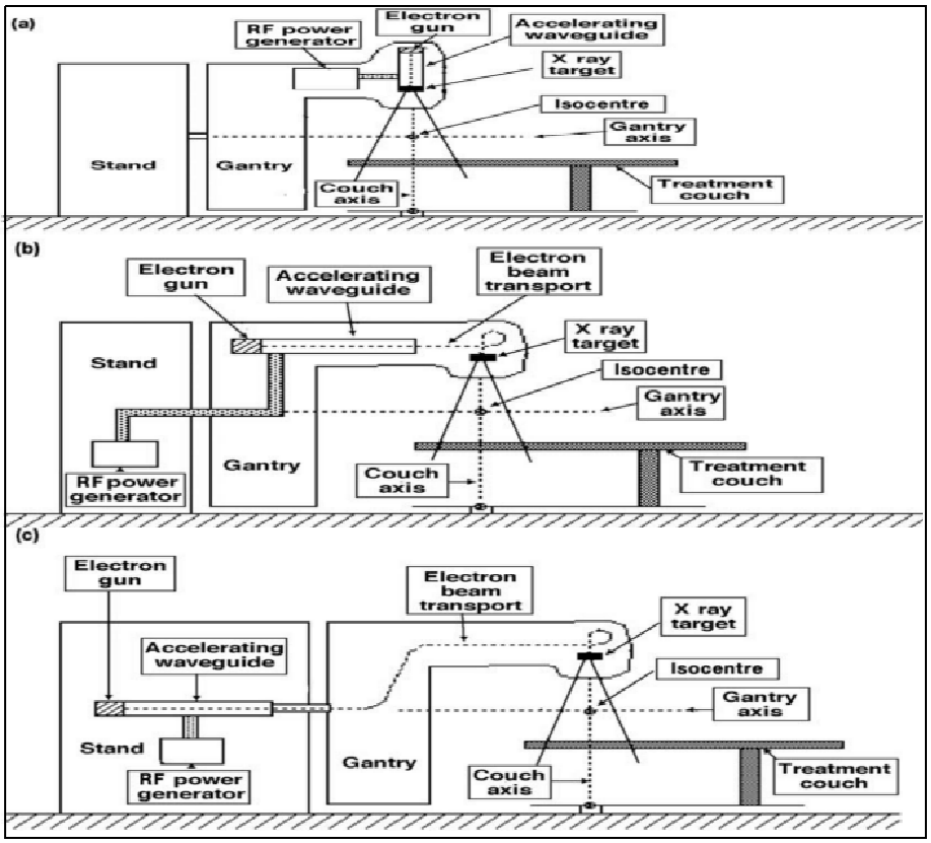

FIGURE 1.7: Design configurations for isocentric medical linacs [19].

¶ Standing wave structure; used by Mitsubishi, Siemens, and Varian . Each end of the accelerating waveguide is terminated with a conducting disc to reflect the microwave power, resulting in a buildup of standing waves in the waveguide.

Figure 1.8. shows the cavities which are clearly visible: the accelerating cavities are on the central axis; the coupling cavities are off-side. The electron gun is on the left, the target on the right.

♣ Microwave power transmission

The microwave power generated by the radio frequency generator is transported to the accelerating waveguide through rectangular uniform S-band waveguides that are evacuated or pressurized with a dielectric gas (Freon or sulfur hexafluoride, SF_6) to twice the atmospheric pressure. The circulator (isolator) is the main component that must be added into the radio frequency power transmission circuit between the RF generator and the accelerating waveguide, which transmits the RF power from the RF generator to the accelerating waveguide.

♣ An auxiliary system

The linac auxiliary system consist of four systems:

¶ A vacuum pumping system creating a typical vacuum pressure levels of 10^{-7} torr (1 torr = 1 mm Hg = 133.3 Pa, 1 atm = 760 torr). This is to avoid arc discharges

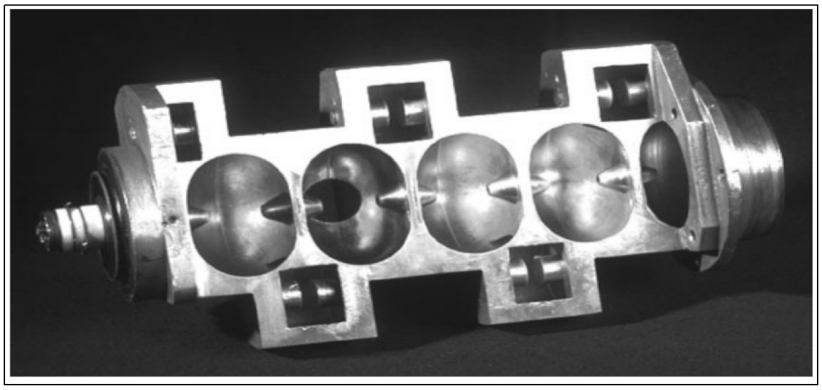

FIGURE 1.8: Cutaway view of a standing wave accelerating waveguide.

when exposed to high transient electric fields in the accelerating guide and the RF generator.

¶ A water cooling system: many accelerator components need cooling to shed heat: the accelerating guide, target, circulator and RF generator.

¶ Shielding against leakage radiation.

1.3.3 Linac treatment head

The linac is an important tool in external beam radiotherapy. The mains operations of the linac has been discussed in depth in the literature [38,39]. This section focuses on the general design of the head's linac components (figure 1.9) that produces high energy x-ray beam. x-ray energies generally range between 4 and 25 MV.

The components of the linac treatment head have an important influence in the production, shaping, localizing and monitoring of the clinical photon and electron beams. Electrons coming from the electron gun brought, in the form of a pencil beam, through the beam transport system into the linac treatment head, where the clinical photon and electron beams are generated.

1.3.3.1 Target and absorption layers

Targets of medical linacs are often considered as thick targets (usually tungsten or a copper-tungsten laminate). Its high atomic number makes it possible to create bremsstrahlung photons. However, it also allows the initial electrons to pass the targets. This is where the absorption layers come into play. The aim of absorption layers is to eliminate the electron contamination due to primary electrons. Unlike the target, the absorption layer is much thicker and is composed of graphite. For Siemens PRIMUS 6 and 23 MV, the target is a thin layer of gold. For 6 MV, the absorption layers of graphite was used alone in the target. For 23 MV, an additional layer of aluminum absorber must be inserted. This second absorber is positioned below the thick target. For Varian 6 MV the target is consisted of tungsten material and is located under the incident primary electron beam. It is the source of the generation of the photon fluence for the medical accelerator. A layer of copper is placed below the target ensuring the absorption of low energy electrons.

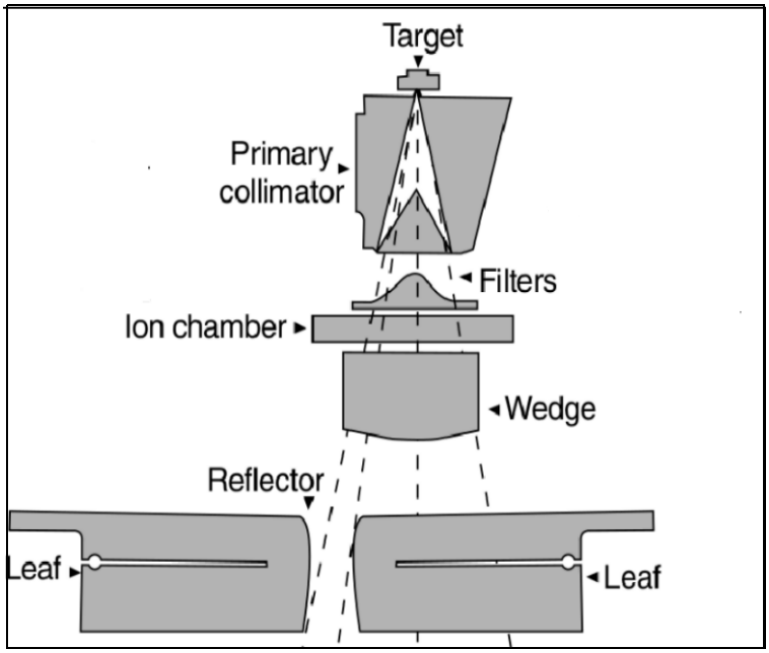

FIGURE 1.9: Diagram of Elekta MLC head's linac.

1.3.3.2 Primary collimator

Once the beam pasts the thick target, it enters the primary collimator. The aim of the primary collimator is to constrain the maximum field. The primary collimator is modeled by superimposing several cylindrical layers of different internal radius. These layers are composed of tungsten and are thick enough to protect the outside of the collimator from the internal radiation. The inner rays of these layers form a cone making a maximum cylindrical field of 50 cm in diameter at 100 cm from the source (outer surface of the target). According to IEC recommendations [40], the maximum leakage should not exceed 0.2% of the open beam value. For ELEKTA SL 6 and 10 MV, the maximum field size is 40 cm square. It is represented in the form of a cylinder. the air gap giving a conical distribution for the photon beam coming from the target which was obtained by the intersection of a cone and the inner part of the cylinder forming the primary collimator. For PRIMUS 6 and 23 MV, the primary collimator is modeled by superimposing several cylindrical layers of different internal radius. The inner radius of these layers form a cone making a maximum cylindrical field of 50 cm in diameter. For Varian 2100C, the primary collimator has the maximum field size and a maximum circle of 49 cm.

1.3.3.3 Flattening filter

When electrons with mega-voltage energies strike a target, the angular emission distribution of the photons is mainly directed forward. To obtain a uniform dose profile, a flattening filter must therefore be used. The absorbers assemble to the flattening filter that removes a large amount of the electrons contaminations and create new secondary electrons. Flattening filter component ais characterized by the following characters:

¶It is a conical shaped metal absorber, that absorbs more forward peaking photons than the ones in the periphery.

¶It shapes the x-rays in their cross sectional shape.

¶Creating a flattened beam of sufficient area, uniformity and symmetry.

¶Most materials composed the flattening filter are Tungsten, Steel, Lead, and Aluminum.

¶In dual-energy photon linacs, two flattening filters are required for the low and the higher photon energies.

For the Siemens configuration, the asymmetrical components of the flattening filter lead a small increasing in fluence and energy rate at the periphery of positive X localization. So this result requires the optimization of asymmetry of the source model or the modification of the flattening filter. For Elekta SL 6 MV photon beams; the flattening filter is placed at the output of the primary collimator. It is represented by the top section of the cone. In the case of Elekta SL10 MV photon beams, it is represented by a hardening filter beam that has a high thick and near the primary collimator. The density of materials is the same for both cases. For Siemens primus 6 and 23 MV, the flattening filters are made of steel.
The flattening filter for 23 MV has a tungsten lower part and has an asymmetric component in the X-axis. This asymmetry is defined in the Siemens specifications and introduces 1 mm spacings between these asymmetric layers.

1.3.3.4 Monitor ionization chambers

Monitor ionization chambers are used to monitor the dose delivered by the linac to patient. It can be usefully divided into:

¶Thick walled sealed ion chambers can be utilized only when photon beams are being monitored.

¶Thick walled unsealed ion chambers would have generally same characteristics as a thin walled unsealed chamber.

¶Thin walled unsealed ion chambers can be utilized to monitor both photon and electron beams.

¶Thin walled sealed ion chambers are not affected by humidity variations but flexing of the thin walls allows variations in the density of the gas filling.

1.3.3.5 Secondary collimator

The radiation beam must be constrained in some way to establish that only required part of the patient is irradiated. For that objective, the radiation beams must be collimated by adjusting the upper and lower collimator jaws. The jaws are made of High Z number, like Tungsten or Lead. The jaws can define a square, rectangular or circular shaped beam up to 40 cm. As the jaws are oriented perpendicular to each other X and Z axis. In all cases, the movements of the blocks are independent of each other. Modern linacs incorporate independent (asymmetric) jaws that can provide asymmetric fields that used when we want to block the part of the filed jaws without changing the position of the isocentre. For Elekta SL 75/25 18 MV, the collimator is modeled by a pair jaws in the X and Y directions which consist of a mixture of two materials (Lead and tungsten). For Siemens primus 6 and 23 MV;two tungsten blocks.

1.3.3.6 Mirror

Generally, mirror consists of the Mylar material, which is a dielectric that is used in some capacitors, transformers, and microphones. Mylar is used as a thermoplastic insulation because of its good dielectric strength, chemical resistance, and water impermeability. Mirror portion itself can be made up of an arbitrary number of layers with thicknesses and media. They are used to visualize the radiation field. For Varian 6 MV, The mirror made of a Mylar film inclined by an angle of 35^o to perform the necessary field size. For Siemens primus 6 and 23 MV, the mirror is used to visualize the radiation field.

1.3.3.7 Multi lame collimator (MLC)

MLC is an important tool for radiation therapy and a relatively recent technology implemented to linac. It is added as a substitute for supplying intensity modulated fields in conformal radiotherapy, either in step and shoot mode or in continuous dynamic mode. The collimator opening is determined by the position of individual leaf openings at the top of collimator, the thickness of the leaves in the Z direction, and two Z "focus" that determine angle of leaf side and end surface (table 1.1).

TABLE 1.1: Characteristics of MLC component by manufacturer's specifications for various linacs existent in 2006.

	Elekta	**Elekta modulator**	**Varian MLC-80**	**Varian MLC-120**	**Siemens 82 leaf**	**Siemens 160 leaf**
type	B	A	C	C	A	A
No. of leaf pairs	40	40	40	60	41	80
Leaf transmission	<2%	<1%	<2.5%	<2.5%	<1%	-
Interleaf leakage	<5%	<1.7%	<4%	<3%	<2%	-
Positional accuracy	1mm	0.5mm	1mm	1mm	1mm	0.5mm
Head to isocentre	<45cm	<45cm	<41.5cm	<41.5cm	42.8cm (including fixed block tray)	42.8cm (including fixed block tray)

Elekta synergy 6 MV linac (Elekta Oncology Systems, Crawley, UK) is equipped with Elekta Agility collimator, composed of 80 leaf pairs and two perpendicular diaphragms (table 1.1). Tungsten alloy is the essential material of choice for leaf construction. For Varian Millennium : linac is equipped with MLC consisting of 120 leaf pairs (table 1.1). Heath and Seuntjens developed a new component called the DYNVMLC [41], to fully model the MLC geometry. The VARMLC (figure 1.10a) and DYNVMLC (figure 1.10b) were compared with respect to interleaf leakage. They found that the differences in dose distributions may not appear important for a

single field but in case where multiple fields are used, like in IMRT, the summed differences become important in the low dose regions as VARMLC underestimates the leaf transmission. De Walle et al. [42] developed a new CM called MLCE to fully model the MLC to investigate the interleaf leakage and transmission (figure 1.11).

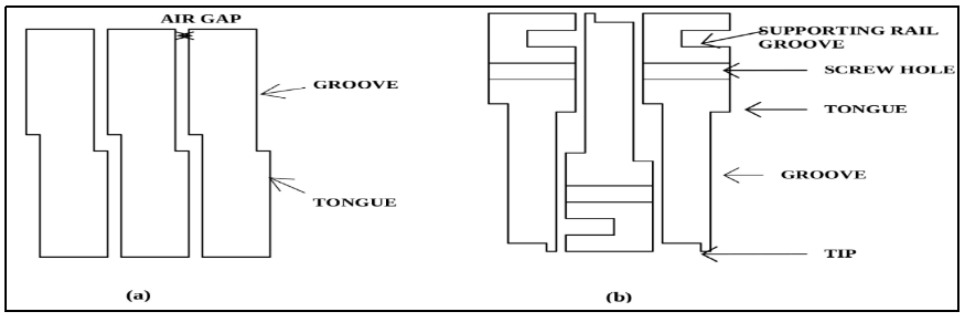

FIGURE 1.10: A simple description of leaf component (a) VARMLC and DYNVMLC (b) [41].

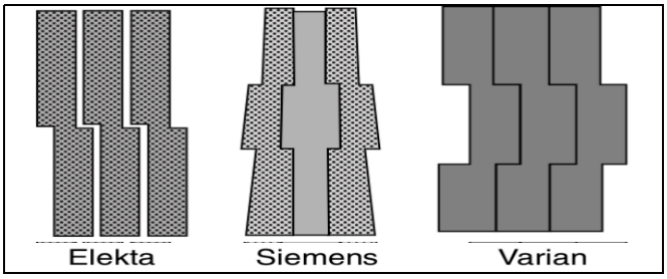

FIGURE 1.11: Stepped leaves to decrease leakage by various linac's manufacturers [43].

1.3.3.8 Wedge filters

Historically, in conventional radiotherapy, a physical or fixed wedges have been routinely implemented for dose shaping i.e. to alter the photon beam intensity and to provide oblique isodose distribution in patients. Due to the development of the technology, Varian (Varian Medical Systems, Palo Alto, CA) was the pioneer in the clinical introduction of the dynamic wedge. This feature was available in 1991 in the Varian 2100C linac based on the work of Leavitt et al. [44]. Although the dynamic wedge was a novel addition to linac, there was a desire for further improvement in its capabilities. This development was incorporated by Varian in their modern linacs with the implementation of enhanced dynamic wedges (EDWs).

Chapter 2

Radiation Transport and Physical Parameters of Photon Beams

2.1 Introduction

In this chapter, We covered the interactions of photon and parameters characteristic of photons interactions with matter that the Compton and photoelectric effects are the dominants mechanisms. This will allow us to develop our understanding of the mechanisms of the photon interactions with the matter during the treatment. Pair production, Compton incoherent scattering, photoelectric absorption, and Rayleigh scattering will be presented according to the atomic number Z of the absorber and the energies used in radiotherapy between 4 and 25 MeV for linac. When traversing any material, the photon has a certain probability of interacting with that medium. These interactions can be classified according to: nature of interactions (photon-electron or photon-nucleus); type of the event produced (absorption, diffusion or production of the pairs).

In the second part, we presented the interaction of electrons and parameters characteristic of electron interactions with the atoms of the medium traversed, electron-electron or electron-nucleus. So there are two probable interaction mechanisms for electrons in the energy range from a few hundred eV up to 25 MeV. In the first case, an interaction between an electron and bound atomic electron, we will speak of collision (ionization and excitation). In the second case, we have an interaction between an electron and nucleus (Bremsstrahlung or radiative losses).

In the last part, we described the external beam quantity used in radiotherapy. The external radiation beam is used to irradiate the patient. We note that, external beam radiotherapy can be used by three beams modes : the photon beams with most percent; some percent with the electron beams; a small percent for heavier particles such as protons, neutrons or heavier. All the photon beams are described by the same physical parameters. This part deals with beams parameters and quantities described external photon beam in radiotherapy field.

2.2 Photon interactions

2.2.1 Pair production

A photon interacts with the nucleus of an atom to produce an electron-positron pair [45–48] with a combined kinetic energy equal to $h\nu - 2m_e c^2$ (energy greater

than or equal to $2m_ec^2 = 1.022MeV$ i.e the minimum energy required for the effect to happen). This interaction is most likely for higher energy simulations. The probability for pair production is zero for photon energies below the threshold energy and increases rapidly with photon energy above the threshold energy level. The Schema for pair production of electron-positron pairs is given in figure 2.1.

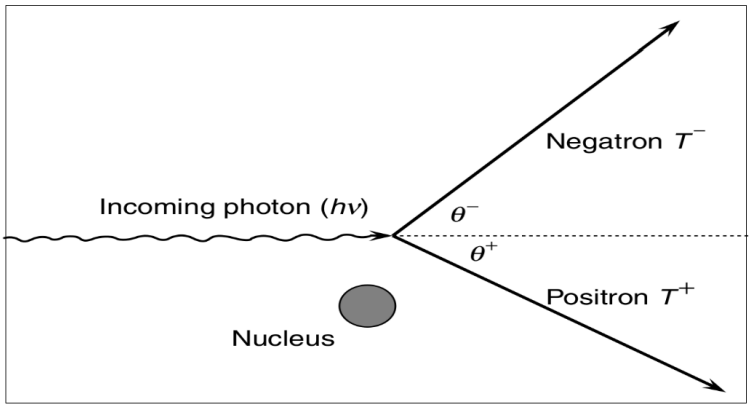

FIGURE 2.1: Representation of the pair production process.

Two electrons are ejected in the forward direction. The mean angle of departure from the photon direction, $\overline{\theta}$ at energies well above 1.02 MeV is expressed as:

$$\overline{\theta} = \frac{m_ec^2}{T^-} \tag{2.1}$$

and

$$T^- = 1/2(h\nu - 1.02) \tag{2.2}$$

The process of pair production may also occur in the electric field of an atomic electron, that a triplet production can occur if a atomic electron rejected receives sufficient energy to exceed the binding energy so that there are 3 secondary electrons produced in the interaction (an electron–positron pair and the orbital electron). The threshold for this effect is equal to $4m_ec^2$= 2.04 MeV.

2.2.2 Compton scattering

Compton scattering was observed by A. H. Compton [49] when a photon imparts only part of its energy to an orbital electron which is essentially free, see figure 2.2.

Figure 2.2. presents the incoming photon of energy hν scattered to produce a scattered photon with energy h$\nu^{'}$ and a recoil electron.

The incoming photon energy hν loses part of its energy to the recoil (Compton) electron and is scattered as photon h$\nu^{'}$ through a scattering angle θ. It is expressed as:

$$\lambda^{'} = \lambda + \lambda_c(1 - cos\theta) = \lambda + h\frac{(1 - cos\theta)}{m_ec} \tag{2.3}$$

where λ_c is Compton wavelength of the target particle and have a value equal to $\lambda_c = \frac{h}{m_ec}$ = 0.024 Å. The angle Φ between the directions of the incident photon and

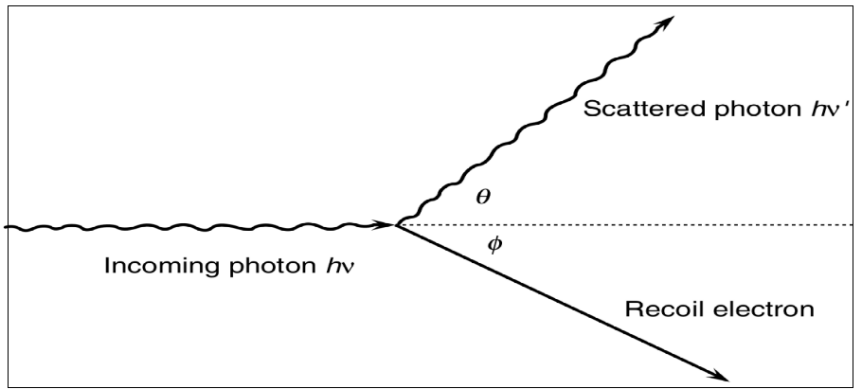

FIGURE 2.2: Schema of an incoming photon of energy hν scatters to produce a scattered photon of energy hν$'$ and a recoil electron.

the electron (figure 2.2) is given by:

$$cot(\Phi) = (1 + \frac{h\nu}{m_e c^2})\frac{tan\theta}{2} \tag{2.4}$$

This equation shows that $\Phi \leq \Pi/2$, and the recoil electron is never emitted in the backward direction.

2.2.3 Coherent scattering (Thomson-Rayleigh)

The Thomson-Rayleigh [50] effect reflects the diffusion of a photon without any change of energy. The incident photon crossing the periphery electrons of the atom shows an elastic collision with theses electrons. The photon didn't loss any fraction of energy and is diffused with a weak angle. Thomson-Rayleigh effect only occurs for low photon energy values. Its probability decreases very rapidly when energy increases. In human tissues, the relative importance of the Thomson-Rayleigh effect in comparison with other types of interactions is negligible, its contribution to total attenuation is order of a few percent.

2.2.4 Photoelectric interaction

Photoelectric effect is the absorption of a photon by an atomic electron and resulting the emission of an electron from the atom [51]. The photoelectric process can only produced if the energy of the incoming photon is greater than the binding energy of the electron. In this process, note that the photon energy is totally absorbed. On the basis of the principle of energy conservation, we can deduce that an average energy transferred from the incoming photon to ejected electrons is used to extract the inner electron and a relation was established to relate this conservation as follows:

$$E_{cin} = W - h\nu \tag{2.5}$$

Where, $h\nu$ is the energy of the incoming photon, E_{cin} is the excess energy of the ejected electron, W is the binding energy of the inner electron of the atomic shell. A schematic representation of the photoelectric effect is shown in figure 2.3.

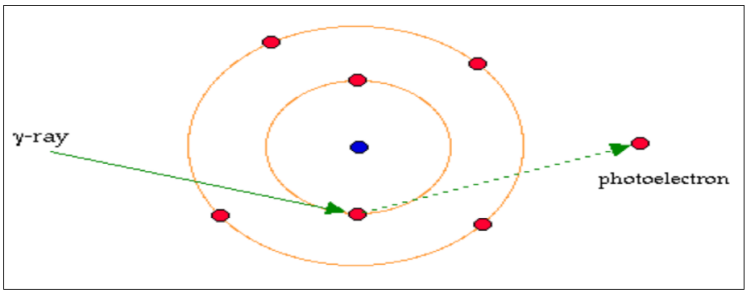

FIGURE 2.3: Shematisation of the photoelectric effect.

Sometimes, for mediums of small Z, the atom, left in an excited state with a vacancy in the ionized shell when an electron in the upper layers takes the place of the ejected electron, relaxes via the emission of fluorescent photons and Auger and Coster-Kronig electrons.

2.2.5 Cross sections of photon interactions

The interaction of photons with matter is through four processes as we have seen in the previous sections: Rayleigh scattering; photoelectric effect; Compton scattering; and pair production. Each one of these modes of interactions is associated with an effective cross section σ data, which calculated as a function of atomic number Z of the absorber medium and energy of the incident photons E. The relative importance of these four modes as a function of E and Z is shown in figure 2.4.

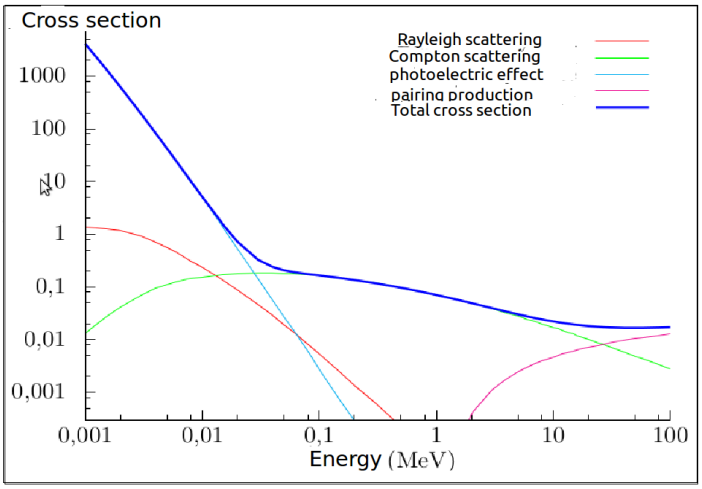

FIGURE 2.4: Domain of the four interactions process.

The probabilities associated with radiation particle interactions in a medium can be expressed as differential cross sections which are probability density functions.

2.2.5.1 Photoelectric process

Photoelectrons are atomic electrons emitted when energy is absorbed from an incident photon as we have seen in the previous section. In practice, the cross sections for the photoelectric effect for K shell may be parameterized as:

$$\sigma_{Kph} = \frac{8\pi r_0^2}{3}.\frac{Z^2}{137^4}.4\sqrt{2}\epsilon^{-7/2} \tag{2.6}$$

Where, r_0 = 2,818 fm electron radius at rest, $\epsilon = \frac{E}{E_0}$ (E_0 = 511 KeV).
In general, the cross-section σ_{ph} for photoelectric can be expressed as:

$$\sigma_{ph} \propto \frac{Z^{4.35}}{E^3} \tag{2.7}$$

In general, the cross-section σ_{ph} for photoelectric absorption increases strongly with decreasing photon energy.

2.2.5.2 Compton process

If the binding to the atom is neglected and the electron is considered to be at rest, the differential Compton cross-section for the process is given by the Klein-Nishina formula:

$$\frac{d\sigma_{KN}}{d\cos(\theta]} = \pi r_0^2 Z X_{KN}, X_{KN} = (\frac{K_c}{K})^2[\frac{K_c}{K} + \frac{K}{K_c} - \sin^2\theta] \tag{2.8}$$

Where; θ, is the polar angle of the scattered photon with respect to the initial direction, K is the energy of the incoming photon, K_c is the energy of a photon scattered at an angle θ by free electrons at rest and is expressed as:

$$K_c = \frac{K}{1 + K(1 - \cos\theta)} \tag{2.9}$$

The binding effects and Doppler broadening was included in EGSnrc according to the impulse approximation [52].

2.2.5.3 Pair production process

The cross section for pair production is zero below the threshold. It rapidly increases with increasing energy and, well above threshold, varies approximately as the relation below:

$$\sigma_{a,Pair} \propto Z^2 \tag{2.10}$$

The cross-section for triplet production, at energies above the threshold, approximately varies as Z :

$$\sigma_{a,Pair} \propto Z \tag{2.11}$$

Triplet production is as important as pair production for the hydrogen atom (Z=1), but it has less importance in compared to pair production, with increasing atomic numbers because of the screening of the electric fields of the target entities by the surrounding atomic electrons.

2.2.6 Parameters characteristic of incident photon attenuation.

2.2.6.1 Linear attenuation law

Photons incident on an absorber will either interact in it by producing secondary electrons and/or scattered photons) or else pass through it without interacting. The attenuation of photons in matter depends on the nature of the medium as well as energy of incident photons. The law of attenuation of a monoenergetic beam in a homogeneous medium is given by the following relation:

$$\phi(x) = \phi_0 exp(-\mu x) \tag{2.12}$$

Where, ϕ_0 is the photon flux of the incident beam, $\phi(x)$ is the flux of photons leaving an absorber medium of thickness x, μ is the linear attenuation coefficient.

The linear attenuation coefficient is the probability per unit length for interaction and is related to the total atomic cross section, σ_{tot}, through the following relation:

$$\mu = n\sigma_{tot} \tag{2.13}$$

Where, n is the number of nucleid or atomic electrons per cm^3.

2.2.6.2 Mass attenuation coefficient

The linear attenuation coefficient μ depends on the nature of the medium. If we consider that μ_{water} is the linear attenuation coefficient of water and μ_{air} that of air, the measurements show that $\mu_{water} > \mu_{air}$. In this cas, It is practicable to introduce the density parameter of the medium through to have the same value for the same body regardless of its case.

$\mu/\rho(\text{cm}^2.g^{-1})$ is the probability of interaction per unit mass of the medium traversed.

2.2.6.3 Half attenuation layer

The half attenuation layer (HVL) is the thickness needed to reduce the incident radiation intensity by a factor of two.

$$I_{x1/2} = \frac{I_0}{2} \tag{2.14}$$

The exponential attenuation is parametrized by :

$$I(x) = I_0 exp(-\mu x) \tag{2.15}$$

Where, $exp(-\mu x)$ is the fraction of photons transmitted, I_x transmitted intensity of photon beam, I_0 initial intensity of photon beam, x thickness of absorber.

This relationship highlights the similarity between the radioactive decay law of nuclei and the attenuation of photon beam.

Therefore, by using the relation $I_{x1/2} = \frac{I_0}{2}$ in the previous equation we assured the following relation:

$$HVL = x_{1/2} = \frac{ln2}{\mu} \tag{2.16}$$

These equation demonstrates the relationship between the HVL and the linear attenuation coefficient for monoenergetic photons.

2.3 Electron interaction

2.3.1 Ionisation and excitation

The incident electron transfers some of its kinetic energy to the atomic electron; depending on the value of the quantity of energy transferred, one or other of these reactions will take place. Depending on whether or not ΔE is sufficient to eject the electron from its orbit, two phenomena can occur:

♣ If $\Delta E \geq W_L$: the energy transfer may be sufficient to overcome the binding energy of the orbital electrons, ultimately ejecting them from the atom (figure 2.5). Electrons ejected from the atoms with a kinetic energy (ΔE - W_L) by the incident charged particles are called primary electrons, which may have sufficient kinetic energy to produce ionization in the absorber. Also, theses ejected electrons, called the secondaries electrons, can, in turn, create other ionizations if its kinetic energy is sufficient.

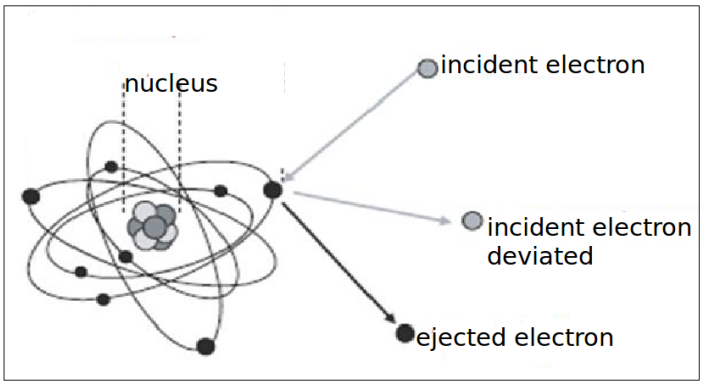

FIGURE 2.5: Ionization processes.

♣ If $\Delta E < W_L$: energy transfer ΔE can not produce any ionization. the electron transfers all or part of its energy to the orbital electrons, raising it to higher energy shells. That can carry the target electron at a higher energy level, with excitation of the target atom (figure 2.6).

The processes of excitation and ionization will continue until the incident particle and all electrons come to rest. Both these processes may rupture chemical bonds in the molecules of the absorber, forming various chemical entities.

2.3.2 Bremsstrahlung

When energetic charged particles, particularly electrons, pass through matter, the electrons interact with the nuclei of the atoms constituting the medium traversed and come close to the atom nucleus, they lose energy as a result of deceleration in the Coulomb field of atomic nuclei and change its trajectory. This change of trajectory and loss in energy appears as an x-ray that is called bremsstrahlung (German

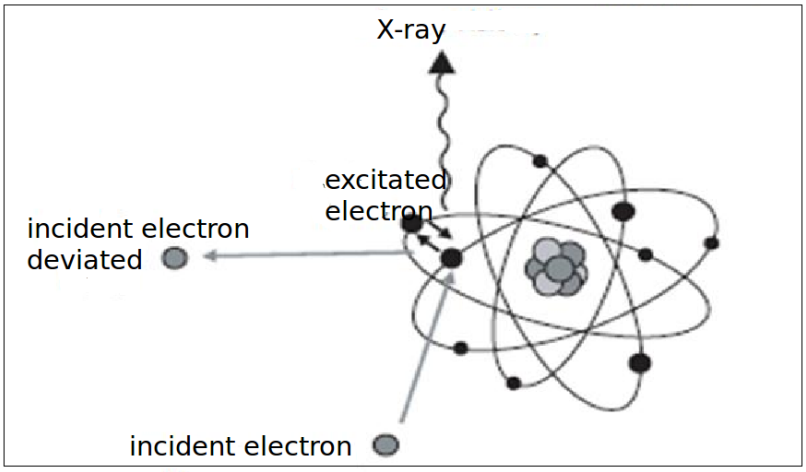

FIGURE 2.6: Excitation process.

for "braking" or "slowing down" radiation) (figure 2.7). This phenomenon concerns only the electrons of very high energies and these bremsstrahlung radiations are generated by striking a tungsten target.

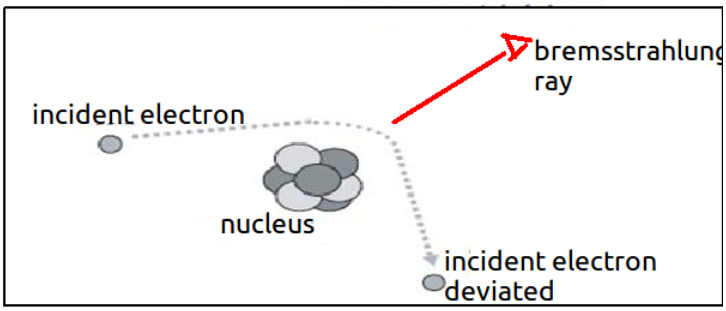

FIGURE 2.7: Processus of Bremsstrahlung.

Bremsstrahlung production is augmented when the kinetic energy of incident particle raises. The bremsstrahlung production is proportional to Z^2 of the atom absorber. It is very significant in heavy metals such as lead and tungsten. Also, Bremsstrahlung is inversely proportional to the mass of the charged particles and therefore is insignificant for heavy particles (alpha particles and protons).

2.3.3 Parameters characteristic of electron interactions

Three important quantities associated with electron during its passage through matter are : linear energy transfer, ionization, and range in the absorber.

2.3.3.1 Linear energy transfer

Through the matter, the charged particles (electrons) loss their energy according to different types of interactions: the elastic and inelastic interactions are done with the orbital electrons and the atomic nuclei of the passing medium. To measure the

energy loss of charged particles, the linear energy transfer (LET) quantity is used which represents the energy loss, per unit of trajectory length of incident particles. The expression of TLE in relativistic mechanics, is given by the formula of Bethe:

$$TLE = |\frac{dE}{dx}| = \frac{z^2.e^2}{4\pi\epsilon^2 m_e V^2}[log(\frac{2m_e V^2}{I}) - log(1 - \frac{v^2}{c^2}) - \frac{v^2}{c^2} - \frac{c_k}{z}] \tag{2.17}$$

Where, z is the charge of the incident particle, V is the electron velocity, m_e is the mass of the electron at rest, e is a primitive charge, ϵ is the permittivity of the vacuum and is equal to 8,854.10^{-10} F.cm^{-1}, c is a speed of light in the vacuum and is equal to 3.10^8 m.s^{-1}, N is the number of target nuclei per unit volume of the absorbing medium, Z is the atomic number of absorbing madium, C_k is a correction term that depends on energy and Z when the complete structure of the nuclei of matter is taken into account, I is the average value of the ionization potential taking into account the ionization and the excitation of the slowing atoms (in eV):

$$I = 9.1Z(1 + 1.9Z^{2/3}) \tag{2.18}$$

2.3.3.2 Specific Ionization

Specific ionization (SI) is defined as the total number of ion pairs created per unit length of the path of the incident beam. In ionization, an average energy of W is required to create an ion pair in the absorber. The value of W is about 35 eV in air and less in oxygen and xenon gases. Specific ionization decreases with increasing energy of the charged particle because of the decreased probability of interaction at high energies. Toward the end of the path, the charged particle shows a sharp increase in ionization. This peak ionization is called Bragg ionization.

2.3.3.3 Range

Range (R) of a charged particle in an absorber is the straight line distance traversed by the particle in the direction of the particle. The range of a particle depends on the mass, charge, and kinetic energy of the particle and also on the density of the absorber. Electrons interact with orbital electrons of the same mass and are deflected considerably. This makes it paths be tortuous. In this case, the true range is less than the total path traveled by the particle. There are many empirical relationships for calculating the range value as a function of the energy of the incident electrons and the nature of the material traversed:

$$R = 0.412\frac{E^n}{\rho} \tag{2.19}$$

And

$$n = 1,265 - 0,0954lnE \tag{2.20}$$

Where, R is the straight-line distance traversed by the particle (cm), E electron energy (MeV), ρ is the density of the material (g.cm^{-3}).

2.4 Photon beam quantity

Radiation dosimetry deals with two distinctly different entities: one describes the photon radiation beam itself in terms of number and energy of photons constituting the photon beam and the other describes the energy quantity of the photon beam may be deposited in a given medium such as water or biological material.

2.4.1 Photon fluence and photon fluence rate

The photon fluence Φ is defined as the quotient dN by dA, where dN is the number of photons that enter a sphere of cross-sectional area dA:

$$\Phi = \frac{dN}{dA} \tag{2.21}$$

The photon fluence rate is defined as the photon fluence $d\Phi$ per unit time dt:

$$\dot{\Phi} = \frac{d\Phi}{dt} \tag{2.22}$$

2.4.2 Energy fluence and energy fluence rate

The energy fluence Ψ describes the energy fluence in a photon beam and is defined as the amount of energy dE crossing a cross sectional area dA by the relation:

$$\Psi = \frac{dE}{dA} \tag{2.23}$$

For a monoenergetic beam, dE is the number of photons dN times their energy $h\nu$, and the energy fluence Ψ in terms of photon fluence Φ is :

$$\Psi = \Phi.h\nu \tag{2.24}$$

The energy fluence rate $\dot{\Psi}$ is defined as the energy fluence $d\Psi$ per unit time dt [53]:

$$\dot{\Psi} = \frac{d\Psi}{dt} \tag{2.25}$$

2.4.3 Absorbed dose

The absorbed dose D is the energy transferred E to the material (tissues) per unit mass dm in a finite volume V [54, 55]. The absorbed dose D (Gy) is defined as:

$$D = \frac{E}{dm} \tag{2.26}$$

The gray unit represents 1 joule of energy deposited in a kilogram of matter [53]:

$$1Gy = 1(J.Kg^{-1}) \tag{2.27}$$

The most usable unit is the Rad (rd) which is given by the following relation [53]:

$$1rd = 10^{-2}(J.Kg^{-1}) \tag{2.28}$$

2.4.4 Absorbed dose rate

The absorbed dose rate is the absorbed dose per unit of time [55] and it is expressed in Gray per second, or more practically in Rad per hour.

$$\dot{D} = \frac{D}{dt} \tag{2.29}$$

2.4.5 Kerma

Kerma (Kinetic Energy Released in Matter) is a non-stochastic quantity and was introduced by the ICRU. It quantifies the average amount of energy transferred from indirectly ionizing radiation (photons) to directly ionizing radiation (electrons) through different photon interactions (photoelectric effect, Compton effect, pair production, etc...). The Kerma $(J.Kg^{-1})$ quantity is given by the following relation:

$$K = \frac{dE_{cin}}{dm} \tag{2.30}$$

The physical amount presents the mean energy transferred dE_{cin} from indirectly ionizing radiation (photons) to charged particles (electrons) of the medium dm. The Kerma is divided into collision Kerma (energy transferred to secondary electrons that is lost in collisions) and radiative Kerma (energy transferred to electrons that is lost through radiative processes). So, the kerma is written as:

$$K = K_{col} + K_{rad} \tag{2.31}$$

A relationship between collision kerma and total kerma K can be written as:

$$K_{col} = K(1 - g) \tag{2.32}$$

g is a factor that represents the mean fraction of the energy transferred to the electrons lost by radiative processes.

2.4.6 Mass stopping power

Mass stopping power is defined as the linear stopping power(rate of energy loss per unit path length (dE/dx) of charged particle) divided by the density of the absorbing medium. Two types of stopping power are known: collision (ionization), resulting from interactions of charged particles with atomic orbital electrons; and radiative, resulting from interactions of charged particles with atomic nuclei. The Bethe theory of the mass soft and hard collision stopping power for charged particles is defined with the equation:

$$\frac{S_{col}}{\rho} = \frac{4\pi N_A Z}{A}.\frac{r_e^2 m_e c^2}{\beta^2}[ln(\frac{2m_e v^2}{I}) - ln(1-\beta^2) - \beta^2 - \frac{C}{Z}] \tag{2.33}$$

Where, β^2 = v/c, m_e electron mass, N_A Avocadro constante, v projectile speed, r_e is the classical electron radius (2.82 fm), Z is the projectile charge in units of electron charge, I is the mean excitation potential of the medium, C/Z is the shell correction.

For electrons and positrons, energy transfers due to soft collisions are combined with those due to hard collisions using the Moller (for electrons) and Bhabba (for positrons) cross-sections for free electrons. The mass collisional stopping power for electrons and positrons, according to ICRU Report No.37, is:

$$\frac{S_{col}}{\rho} = \frac{N_A Z}{A}.\frac{\pi r_0^2 2 m_e c^2}{\beta^2}[ln(\frac{E_K}{I})^2 + ln(1+\frac{\tau}{2}) + F^{\pm}(\tau) - \delta] \tag{2.34}$$

with F^- given for electrons as:

$$F^-(\tau) = (1-\beta^2)[1 + \frac{\tau^2}{8} - (2\tau+1)ln2] \tag{2.35}$$

and F^+ given for positrons as:

$$F^+(\tau) = 2ln2 - \frac{\beta^2}{12}[23 + \frac{14}{(\tau+2)} + \frac{1}{(\tau+2)^2} + \frac{4}{(\tau+2)^3}] \tag{2.36}$$

In this equation, $\tau = \frac{E_K}{m_e c^2}$ and β = v/c.

The mass radiative stopping power is the rate of energy loss by the electrons or positrons that results in the production of bremsstrahlung. The Bethe-Heitler theory of the mass radiative stopping power is [53]:

$$\frac{S_{rad}}{\rho} = \frac{\sigma_0 N_A Z^2}{A}.(E_k + m_e c^2) Br^- \tag{2.37}$$

Where; $\sigma_0 = \alpha \frac{e^2}{(4\pi\epsilon_0 m_e c^2)^2} = 5.80 \times 10^{-28} \text{cm}^2/\text{atom}$, α is the fine structure constant, Br is a function of Z, E_K $5.33 \leq E_K \leq 15$ for energies in the range from less than 0.5 MeV to 100 MeV.

2.4.7 Linear Energy Transfer

The linear energy transfer (LET) L_Δ of a material, for charged particles, is defined as the quotient of dE_Δ by dx [53]:

$$L_\Delta = \frac{dE_\Delta}{dx} \tag{2.38}$$

Where, dE_Δ is the energy lost by a charged particle due to soft and hard collisions minus the total kinetic energy of the charged particles released with kinetic energies in excess of Δ. Where dx is the traversing distance by a charged particle.

2.5 External radiation treatment parameters and spatial distribution of the dose

The goal of external radiotherapy is to use ionizing radiation to treat a tumour. In reality, the beam is modified during its transport inside the matter; it is therefore, necessary to determine the dose deposited in depth as a function of the volume used for irradiation.

2.5.1 Radiation field size

As the irradiation field size rises the scattering volume. This rises causing the dose to increase at the entrance. Radiation beam utilized in radiotherapy are produced with the following fields size: square, rectangular, circular, and irregular fields size. Rectangular and square fields are mainly created with the collimator components, where the circular fields are created with special collimator on treatment machine and irregular fields with asymmetry jaws and multi-leaf collimator (MLCs). For any arbitrary radiation fields size an equivalent square or circular field size may be specified with similar beam parameters that are very important in the radiation dosimetries. An arbitrary rectangular field with sides H and L will be approximately equivalent to a square radiation field with sides H_{eq} when both fields have the same area/perimeter ratio [56]:

$$H_{eq} = \frac{2H.L}{(H+L)} \tag{2.39}$$

A circular field with radius R_{eq} when both fields have the same area will be equivalent to a square field size with sides H_{eq} [55]:

$$R_{eq} = H_{eq}.(\pi)^{1/2} \tag{2.40}$$

2.5.2 Source Surface Distance (SSD)

The SSD is the distance from bremsstrahlung target to a depth where field size is defined and can be related wtith the dose as illustrated in the following relation:

$$D_d = D_{max}\frac{f(d,A).(SSD+d_{max})^2}{(SSD+d)^2} \tag{2.41}$$

Where; D_d is the dose at depth d and D_{max} is the maximum dose at d_{max}.

$f(d,A)$ is the beam attenuation and is an approximately exponential function of the depth d on A field size.

The relation (2.41) demonstrates that, the relative dose increase when increasing SSD. All recent linac manufacturers use 100 cm for their SSD (i.e. the distance from the isocentre to the x-ray target).

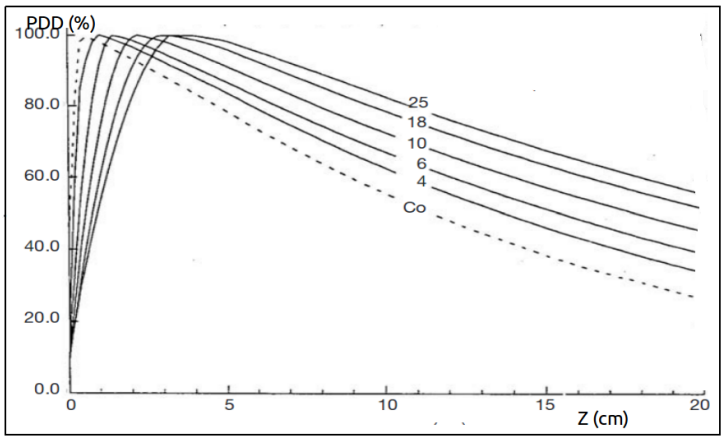

FIGURE 2.8: PDD Curves of PDD for a $10 \times 10\ cm^2$ field at an SSD of 100 cm in a water phantom for various megavoltage photon beams from ^{60}Co to 25 MV [55]

2.5.3 Photon beam energy

An example of PDD distributions for $10 \times 10\ cm^2$ fields and various megavoltage photon beams is given in figure 2.8 and table 2.1. The figure 2.8 and table 2.1 show that the size of the buildup region increases with beam energy.

TABLE 2.1: PDD for various photon beams in a water phantom on $10 \times 10\ cm^2$, SSD of 100 cm and depth 10 cm [55].

Photon beam energy hv (MV)	^{60}Co	4	6	10	18	25
PDD(%)	59	65	67	74	80	82

2.5.4 Percentage depth dose

The percentage depth dose (PDD) is the ratio of the dose at a depth z to the dose at reference depth. This reference depth may be taken where the absorbed dose is maximum or at the depth of 10 cm.

The figure 2.9 shows that:

¶ Low energy photons (^{60}Co, 1.17 and 1.33 MeV) are attenuated in the first centimeters.

¶ When the energy of the electromagnetic waves X or γ increases, the superficial tissues are less exposed to the maximum energy and a high dose can be delivered at significant depths.

¶ The electrons deposit it energies near the skin.

¶ The protons have a very long course before depositing their maximum dose.

In addition to that, after the depth of maximum PDD, the attenuation decreases causing to the decrease of PDD when photon energy increases. The scattering volume increases with the irradiation field size resulting the increase of dose at the entrance. When the skin source distance decreases, the maximum dose approaches the surface and its value increases while the PDD decreases.

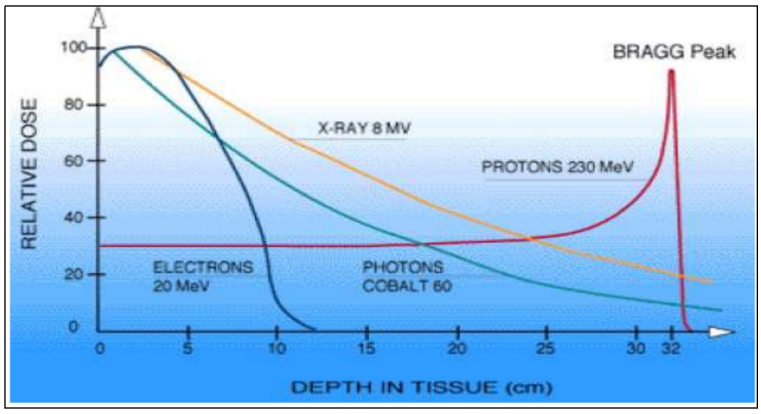

FIGURE 2.9: Curves of relative depth dose transmission and corresponding ionization.

2.5.4.1 Surface dose

The surface dose is defined as the position when the ionizing radiation enters the patient on the surface, where it delivers a certain surface dose D_{max}. In megavoltage linacs, the surface dose changes with the beam energy and field size and is usually lower than the maximum dose D_{max} (see figure 2.10). Many components of the accelerators have contributed to the surface dose quantity as: system collimator; flattening filter; and air (photons scattered); patient or phantom surface (photons backscattered); air and shielding structures (high energy electron contamination).

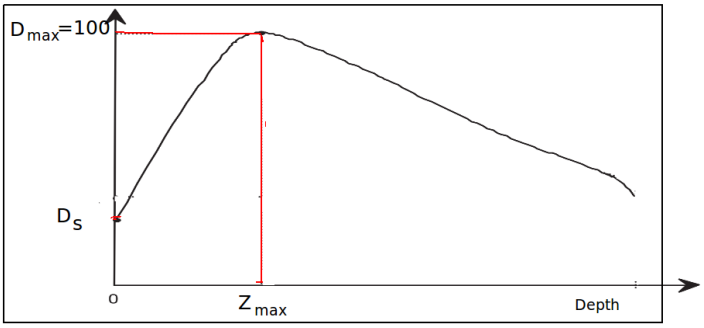

FIGURE 2.10: PDD of a megavoltage photon beam passing through a phantom of homogeneous tissue-equivalent material. D_s is the surface dose. D_{max} is the dose maximum.

2.5.4.2 Buildup region

The buildup region is defined as the region between the surface dose D_s (z = 0) and maximum dose D_{max} (z = z_{max}) in megavoltage photon beams (figure 2.10). The dose buildup region results from the kinetic energy deposited in the patient by the long range of energetic secondary charged particles (electrons and positrons) that first are released inside patient by various photon interactions (photoelectric effect, Compton effect, pair production effect). In the buildup region for photon beam, immediately beneath the entrance of patient, there is incomplete charged particle

equilibrium [57,58]. As the depth z increases, the condition of the charged particle equilibium is probablly attained at z= z_{max}.

2.5.4.3 Depth of maximum dose z_{max}

The depth of maximum dose z_{max} beneath the patient's surface is defined at depth which the dose is taken a maximal value (see figure 2.10). The depth of maximum dose z_{max} depends on two parameters (beam energy and beam field size). Nominal values of z_{max} varies with beam energy (see table 2.2).

TABLE 2.2: Nominal z_{max} for maximum PDD with various photon beams in a water phantom on 10 $\times$10cm^2 and SSD of 100 cm [55].

Photon beam energy hv (MV)	^{60}Co	4	6	10	18	25
Nominal z_{max} (mm)	5	10	15	25	35	50

2.5.5 Beam quality index or tissue phantom ratio

Measured absorbed dose produced by linacs are used as a beam quality index and checked as part of initial acceptance procedure in the dosimetry recommendations [59–61]. Most dosimetry protocols [62–65], based on standards of absorbed dose to water, have recommended the Tissue Phantom Ratio ($TPR_{20,10}$), as the specifier of the quality of high-energy photon beams to be considered a more appropriate choice for radiotherapy beams. The $TPR_{20,10}$ is defined as the ratio of water absorbed doses on the beam axis at the depths of 20 cm and 10 cm in a water phantom, obtained with a SSD of 100 cm and a 10 $\times$ 10 cm^2 field size. The parameter $TPR_{20,10}$ is a measure of the effective attenuation coefficient, and describes approximately the exponential decrease of a photon depth-dose curve and is expressed as :

$$TPR_{20,10} = 1.2661.PDD_{20,10} - 0.0595 \tag{2.42}$$

Where $PDD_{20,10}$ is the ratio of the percent depth-doses at 20 cm and 10 cm depths for a field size of 10 $\times$ 10 cm^2 defined at the phantom surface with an SSD of 100 cm.

2.5.6 Profil dose

The field size of the irradiation treatment is determined by the opening of the jaws. One way to control field size dimensions is to make a profile X and Y axis vertically to the beam central axis at a given depth. These profiles are normalized to the center value. The dose profile can control the homogeneity, the symmetry as well as the penumbra of the photon beams.

The DP regions consist of three distinct regions (figure 2.11); a central region (homogeneous and symmetrical zone), a penumbra region (physical penumbra), and a umbra region corresponding to the transmission through the collimator.

¶ The central region (region 1) is defined as the profile extending from the beam central axis to within 1-1.5 cm from the geometric field edges of the beam. The width

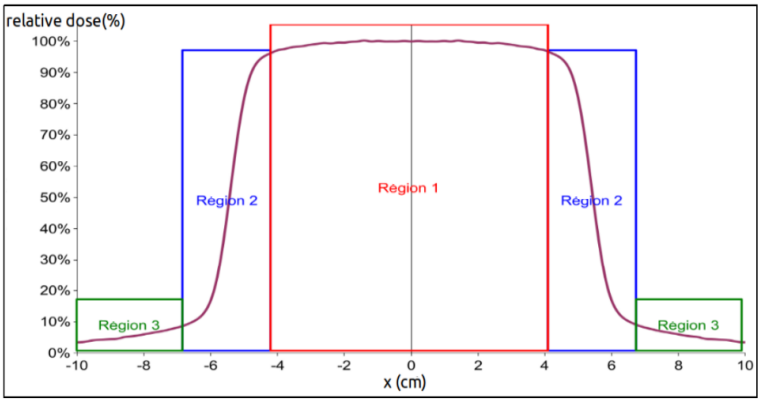

FIGURE 2.11: The DP region on $10 \times 10\ cm^2$ field size.

at half height of this region represents the actual size of the field. In the center of this region, the photon are the most energetic.

¶ The penumbra region (region 2) is defined by the region between the 20% and the 80% of the profile dose and it is caracterized by that the dose changes rapidly inside this region. The total penumbra dose (the physical penumbra) is contributed from the three individual penumbras: transmission(collimator jaws); geometric (source size, SSD, source to collimator distance) and scatter(patient scatter, beam energy).

¶ Umbra region (region 3) is the region outside the radiation field. The umbra dose in this region have generally low values. The collimator and head shielding are the main contributors to the umbra dose.

Chapter 3

Monte Carlo Technique

3.1 Introduction

The evolution of algorithm and computer technologies led to the development of differents MC codes in favor of particles transport. One of the primary codes to transport the particles was called SHOWER1 code, which was written at Stanford Linear Accelerator Centre (SLAC) at Stanford University in the early-to-mid 1960s. Developement of the different codes in the early days have improved remarkably over time, which have extensively conducted to the implementation of the MC codes to have accurate studies in medical physics. As examples of these codes: Electron Gamma Shower (EGSnrc) code was developed by National Research Council of Canada (NRC) [52, 66]; MC N-Particle (MCNP)code originated from ETRAN code, and an extended version MCNPX code by Los Alamos National Laboratory [67]; GEANT4 code from an international collaboration; and Penetration and Energy Loss of Positrons and Electrons (Penelope) code from University of Barcelona [68]. Many studies investigated the differences between theses codes [69, 70].

This chapter presents the fundamentals to understanding the mechanism of the MC method. It also describes the differents user codes based on EGSnrc such as BEAMnrc [71] and DOSXYZnrc codes [72], which were developed to be utilized in radiotherapy applications [73]. Furthermore, this chapter discusses the variance reduction techniques (VRT) and the approximate efficiency improving techniques (AEIT) implemented in BEAMnrc/DOSXYZnrc codes. Finally, it presents errors and uncertainties in MC calculation and some criteres validation of MC calculation in comparing to experimentals reasults.

3.2 Monte Carlo simulation in medical physics

3.2.1 Monte Carlo simulation and its functioning

The MC method is a type of stochastic algorithm used to simulate the reaction of a mathematical or physical system. It is a numerical method focused on random number generator. The utilization of MC simulations for the transport of radiation particles began in the 1940s with the development of nuclear reactor. The idea of using random simulations is directly due to the complexity of radiative interactions in a specific environment. In radiotherapy, the system of interest consists of the patient and the equipment. MC simulations are routinely utilized to determine the properties of treatment beams. This information is needed as input data for any

model-based treatment planning system. Today, the use of algorithm has evolved into the field of medical physics. The implementation of algorithm in MC simulation for medical physics applications, between 1970-1980, proved to be a precise solution and have a great flexibility [74,75]. The flexibility of MC simulation comes from its very structure. When we apply the principle of the simulation to the transport of the particles, it is possible to extract data on all the parameters used in the simulation. For example, it is possible to derive photon source spectra. This type of data is often difficult or impossible to derive from experimental measurements.

There are many steps in MC simulation of radiation transport in matter: Firstly, MC algorithms simulation starts with the initialization of pseudo random number generator. The second step is the application of physical models using the random number generator to choose a physical interaction from the cross section tables. Without going into details, we group the algorithm into three distinct steps: (1) Depending on the type of particles, different interaction probabilities are calculated. (2) The particle is transported to a new point of interaction. This transport follows the energy modifications, initial direction of particles as well as the generation of secondary particles. (3) Finally, once these calculations are done, various calculated data are registered (energies, direction, positions ...). These simulation processes are recursive and start again. The calculation stops only when there is any particle in the geometry.

3.2.2 Transport algorithm of electrons

The simplest way to transport an electron is to ignore its deflections due to multiple diffusion along their steps. The electron can be transported along a line in the same direction as the beginning of the step. To accept this approximation, the size of the step must be small enough. However, a very small step leads to unacceptable simulation times. During transport of a charged particle, the global effects taken into account are: the displacement, the energy loss and the change of direction. The different theories used by the MC codes make it possible to determine the energy loss as well as the angular deflection of charged particles.

The electron-step algorithm used in EGSnrc code determines the algorithm that will be used to calculate lateral and longitudinal corrections which accounts for the elastic scattering in a condensed history electron step. The transport of both particles electrons and positrons employing EGSnrc code includes two algorithms, HOWFAR and HOWNEAR [72]. They are implemented to predict the position of the next interaction of the particle. Each of these interactions corresponds to a calculation step. This is to take into account the fact that an electron interacts several times with the medium between each calculation step. Poon and Verhaegen [77] have established a difference for electron in percentage depth dose with energies of 1 MeV and 10 MeV on a water phantom by 10% and 6%, respectively. The results due to the multiple scattering algorithm, between GEANT4 and BEAMnrc.

3.2.3 Dose calculation algorithms for photons particles

Before focusing with MC calculations, it is important to make a general overview of the dose calculation algorithms for photons particles. The largest dose calculation

algorithms developed for photons are non-stochastic. The convolution/superposition algorithm didn't assume that the energy of the charged particles is deposited locally at the interaction site. In addition, it allows a specific correction for the missed equilibrium produced by the lateral diffusion of the particles. For that reason, the superposition/convolution algorithm is considered more accurate in comparison to other algorithms (except MC). Moreover, for heterogeneous phantoms calculations, the superposition/convolution algorithm corrects inhomogeneities by utilizing the effective density. This type of correction is not ideal and generates dosimetric errors close to interfaces with heterogeneities [78]. In this situations, the MC simulation is the best choice and solution. The photons propagate rectilinearly between each interaction. The transport of photons through the medium uses only the HOWFAR algorithm in EGSnrc MC code. This calculates the position of the interaction from the attenuation factor in the material. Once the position of the interaction has been calculated, a probability distribution based on different interaction cross-sections is then set up.

3.3 EGSnrc user code

The Electron Gamma Shower system (EGS, updated to EGSnrc) is one of the most widely used MC codes for simulating coupled electron-photon transport. This code is useful in simulating electrons and photons with energies in excess of a few keV up to several hundred GeV, and has been widely benchmarked. The extended low energy simulation abilities gave the code utility to other disciplines, such as the medical physics community [79]. The code was released to the public as an open source package in 1985 as purpose of academic research and not for commercial utilization. The current version of the code, EGSnrc user package, made numerous improvements to the radiation transport that are listed in the manual [52]. Figure 3.1 shows a summary history development of EGSnrc code.

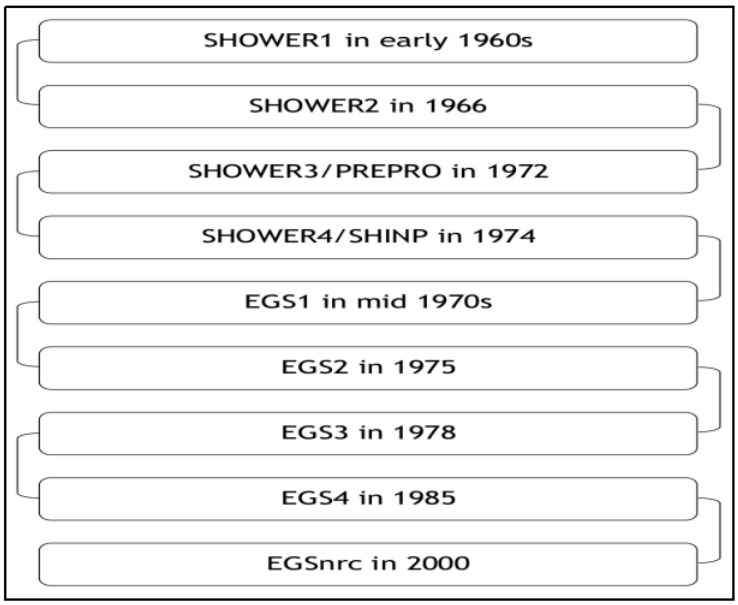

FIGURE 3.1: The development of EGSnrc code.

The MC calculation is initialized in EGSnrc from input files. All the data needed for the calculation must be recorded in these files:

¶Initial source properties

¶Particle propagation geometry

¶Geometry of the dose measurement

¶Pameters specific to the calculation machine

¶Physics processes

The following physics processes are taken into account in EGSnrc:

¶ For charged particles: bremsstrahlung production, positron annihilation at rest and in flight, Coulomb scattering from nuclei, electron-electron (Møller) and positron-electron (Bhabha) scatterings.

¶ For photons: pair production, Compton scattering, Coherent (Rayleigh), photoelectric effect.

¶ Relaxation of excited atoms leading to fluorescent photons as well as Auger and Coster-Kronig electrons.

EGSnrc is a general purpose package for MC simulations of coupled electron, positron and photon transport that employs the condensed history technique. A number of user codes for example; BEAMnrc, DOSXYZnrc, and EGS_ chamber. . . etc, have been developed based on core of the EGS code for interaction modelling EGSnrc, each designed for a specific purpose. There has been further simplification in the development of a graphical user interfaces to model a given geometry accurately. In this project, three different user codes were used, namely BEAMnrc [71], DOSXYZnrc [72] and BEAMDP [80]. In 2003, I.Kawrakow et al [81] developed EGSnrcMP (multi-platform) which is a new environment means that EGSnrc Works on Windows & Unix/Linux systems. The current version at the time of this project EGSnrc V4 2.4.0, was considered physically valid for photons, electrons, and positrons.

3.3.1 BEAMnrc user code

The BEAM user package has been updated to BEAMnrc version, to correspond with update of EGS4 to EGSnrc version. First, BEAMnrc was developed in collaboration between NRC and University of Wisconsin in 1990s in a collaborative project named Ottawa Madison Electron Gamma Algorithm (OMEGA). Original BEAMnrc code came as a solution to the difficulties presented in building the complex geometry of a linac using the EGSnrc user code. In 1995, D.W.O. Rogers developed and updated BEAMnrc code to simulate all types of modern clinical accelerators [82]. That code was made available publicly for research and educational purposes. This has given medical physics researchers worldwide the opportunity to utilize this code, and hence the increase of MC studies, especially in the radiotherapy field. Its structure is based on the module components (CM) representing the accessory of the linac. The dimensions and the physico-chemical composition of each CM are fixed from the engineering plans, provided by the manufacturer. It allows the modeling of photon beams, electrons and energy positrons between 1 keV and 1 GeV as well as the 3D dosimetry.

Particles are created by thermionic emission in the electron gun and accelerated through a waveguide downstream of the target. These two structures are ignored by

the BEAMnrc code. Really, the origin of the electrons is not modeled. The simulation with BEAMnrc MC code goes through three main steps:

♣ Step 1: The simulation with BEAMnrc goes through the definition of several parameters, like statistic, physic, and geometric parameters (materials, dimension (x, y, z) directions, positions of component), more than 20 precoded components were implemented in BEAMnrc to simplify modelling components of the system of interest. Each CM is utilized for a specific purpose, for example, CMs known as XTUBE and SLABS are used to simulate a x-ray target (anode) and a filter of a specific thickness and material, respectively. Also some CMs are used to model complex geometries such as DYNJAWS, which is utilized to simulate the dynamic jaws used during a radiotherapy treatment. The input file also contains information and parameters specified by the user for the simulation. For example, it includes the number of histories to be simulated, parameters of the VRTs, values for PCUT and ECUT, and database (cross section data).

♣ Step 2: Subsequently, a compilation is necessary to allow the verification of the geometric model, thus allows the generation of the files necessary for the execution of the code, like the file mortjob.mortan which comprises the definition of various simulation parameters. The simulation can be executed through two modes: batch or interactive; the interactive mode allows visualization of the simulation progress, it is useful in the case of a small number of stories to simulate, and can be used with both Windows and Linux operating systems; the batch mode is faster mode and recommended for the simulation of a large number of history, this mode allows execution in parallel mode which is used multiple calculation units like the case of the cluster or the grid computer.

♣ Step 3: At the end of execution, the user can have multiple output files as shown in figure 3.2. The PHSP is a plane chosen by the user to score and register energy, direction and particles coordinates in a PHSP file, this file is subsequently used as a virtual source in the DOSXYZnrc code. In the case of a lack of storage capacity, a shared library from BEAMnrc code is created. The shared library allows making BEAMnrc the source for the simulation, and running another code such as DOSXYZnrc simultaneously without a need to record an intermediate PHSP file. However, this needs longer simulation time [83]. Therefore, the method of using the PHSP file as a source was employed in this thesis. The PHSP file can also be analyzed by another code called BEAMDP to extract information from the PHSP file from the simulation [103]. Other files can be registered to have the dose and statistical uncertainty in the different components of head's linac, these files have an extension (.egslst).

A number of multiple source routines implemented with the BEAMnrc code are available, that each source had its own characteristics. We presented two source with the required input parameters that we used in this study:

¶ ISOURC=19 Elliptical beam with Gaussian distributions in two directions X and Y(figure 3.3). This source is an elliptical beam where the ellipse is defined by gaussian intensity distributions in X and Y directions. The shape of the ellipse is defined by RBEAM and RBEAMY which define the FWHM of the gaussian intensity distributions in the X and Y directions, respectively. UINC which define the X-axis direction cosine, VINC is the Y-axis direction cosine, and the WINC which is the Z-axis direction cosine.

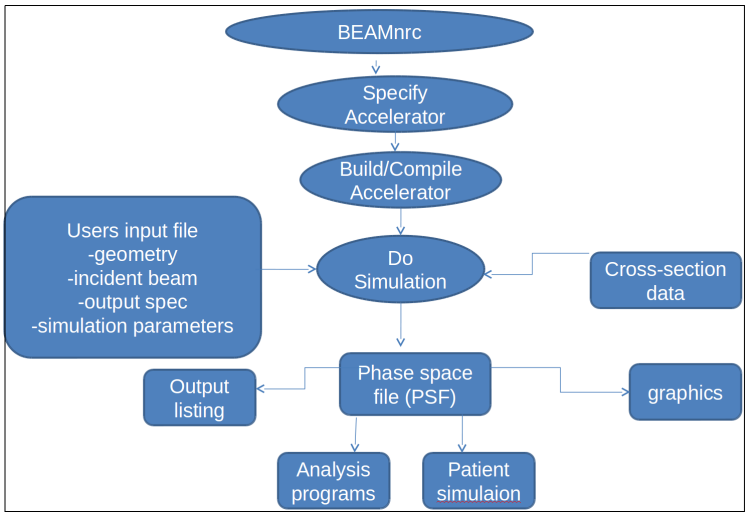

FIGURE 3.2: The main steps involved to run the the BEAMnrc system.

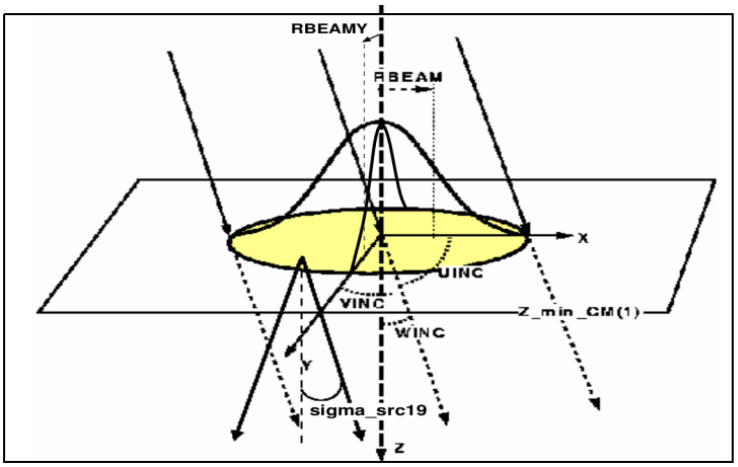

FIGURE 3.3: Elliptical Beam with Gaussian Distributions in X and Y (ISOURC=19).

¶ ISOURC = 21 This PHSP source allows the BEAMnrc code to generate a PHSP file at any scoring plane to be used as a source. They are particularly useful for doing repeated simulations of which can be located at the bottom of any CM of an accelerator model.

3.3.2 Phase space files

Standard phase space file

Standard PHSP file contains the following information: total number of particles registered in the file, total number of photons stored in the file, maximum kinetic energy of the particles stored in the file, charge, minimum electron kinetic energy, number of particles incident from original source, particle total energy, particle X-position, particle Y-position, X-direction cosine, Y-direction cosine, particle's weight, Z-position of last interaction for photons and is Z-position of where an electron or its ancestor was set in motion by a photon.

IAEA format phase space data

BEAMnrc has the capability to read/write phase space data in IAEA format. This IAEA format PHSP could be used as source in other MC codes such as GEANT4, PENELOPE, FLUKA ...etc. This allows the user to add to or make use of data from the IAEA's online accelerator phase space database generated by other MC codes. Phase space data in IAEA format is contained in 2 files: the data file (with extension .IAEAphsp) and the header file (with extension .IAEAheader).

The IAEA header file output by BEAMnrc contains the following data: size of the .IAEAphsp file in bytes; data that is stored in the .IAEAphsp file; value of the Z of the scoring plane; length of a phase space record in bytes; number of primary histories used to generate the phase space data; total number of particles represented in phase space data; number of photons represented in phase space data; total weight, min. weight, max. weight; average total energy, min. total energy and max. total energy for each particle type; min. and max. X and Y of all particles scored.

3.3.3 DOSXYZnrc user code

DOSXYZnrc is part of the BEAM/OMEGA system developed by the NRC (National Research Council Canada). DOSXYZnrc calculates 3D absorbed dose in phantoms of simple geometries designed in the simulation of dose deposition in a rectilinear voxel phantom or in complex geometries extracted from CT images. The code can be submitted on parallel computing platforms such as Clusters or computer grids.

The steps required for DOSXYZnrc simulations are similar to those followed in BEAMnrc. The figure 3.4 shows the necessary files and steps to run a simulation in DOSXYZnrc code.

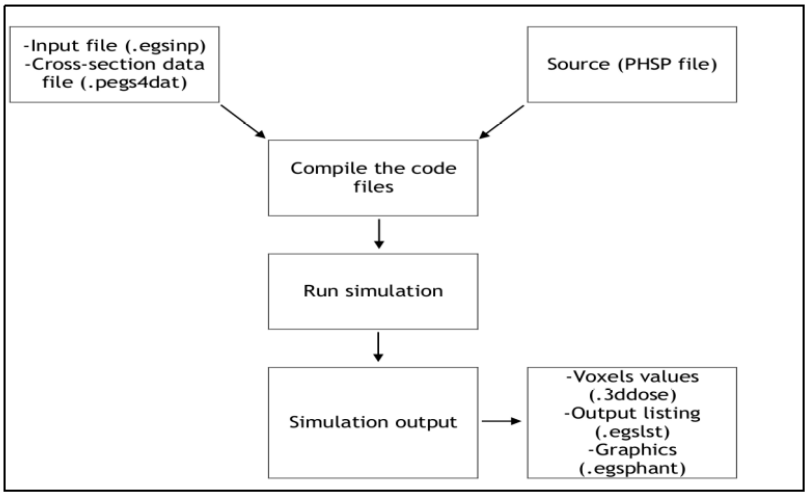

FIGURE 3.4: A schematic flowchart illustrating the steps for DOSXYZnrc simulation.

For DOSXYZnrc input file, the user must define the input file which includes the phantom geometry, the size of the voxels, the source of particles such as the PHSP file,...etc. The number of simulation histories is an important parameter to consider in any DOSXYZnrc simulation. Principally, if the number of histories is too low then

the uncertainties associated with the doses per voxel become relatively large. This can lead to high uncertainties in the penumbra regions.

A number of various source routines are available with the DOSXYZnrc code, each with its own characteristics and required input parameters. In this thesis, we will described some parameter of the phase space source (ISOURCE = 2) which was used for this study:

♣ ISOURCE = 2: PHSP Source incident from any direction delivers the particles from a PHSP file generated during a BEAMnrc simulation at any scoring plane of a linac geometry to a phantom.

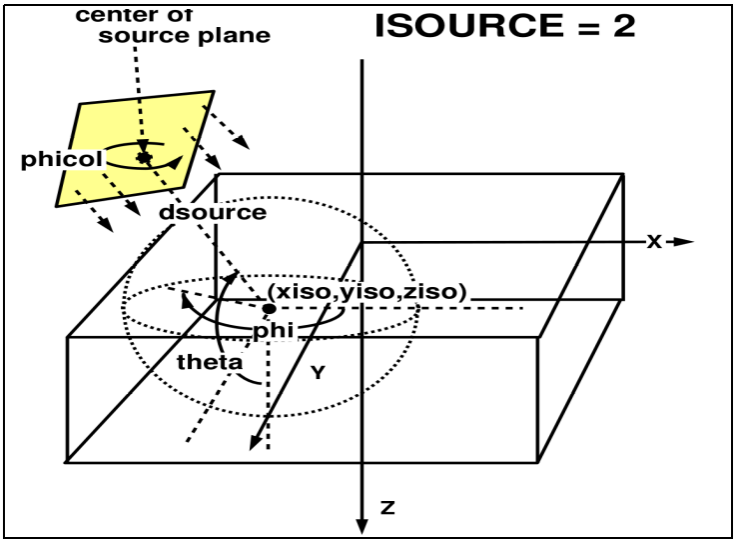

FIGURE 3.5: Phase-space source incident from any direction (isource=2).

Input parameters for a phase-space source (ISOURCE = 2) are (see figure 3.5): x, y, and z coordinates of the isocenter normally located within the phantom, angle between the +z direction and a line joining the center of the beam, angle between the +x direction and the projection on the xy plane of the line joining the center of the beam, absolute distance from the isocenter to the source center, angle by which the source is rotated in the source plane perpendicular to the beam direction, the medium number for the region surrounding the phantom, and the dimensions of the region surrounding the phantom.

In addition to the standard BEAMnrc PHSP files described above, DOSXYZnrc can also use IAEA-format phase space data as a source. Phase space data in IAEA format comprises both a header (extension.IAEAheader) file and a phase space data (extension.IAEAphsp) file.

The DOSXYZnrc outputs are given in a file in (.3ddose) extension. The results can also be listed in the (.egslst) file. The (.3ddose) file is, then, analyzed by a code called STATDOSE [84] or a specific code developed by the user such as a Matlab code. DOSXYZnrc allows the user to output the phantom geometry in a file in (.egsphant) extension. This file can then be used with the (.3ddose) file to show the dose distribution inside the phantom using dosxyz_show code [85].

3.3.4 PEGS4 data: 521icru or 700icru

PEGS4 is the program which prepares much of the material dependent cross section data (see figure 3.6) sets required by EGSnrc to do the simulations with other pakage EGSnrc code as BEAMnrc, DOSXYZnrc, DOSRZnrc, SPRRZnrc...etc.

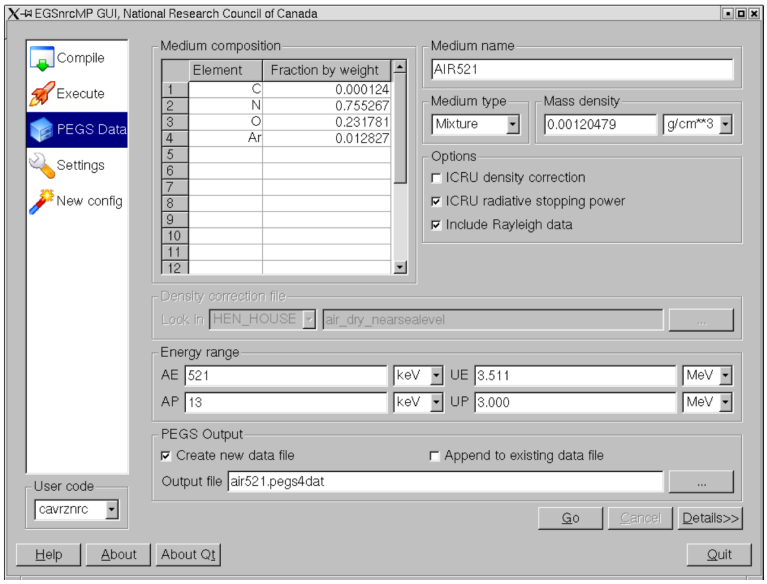

FIGURE 3.6: Egs_gui parameter to run PEGS4 to create an air data set.

Two defaults PEGS4 data sets containing commonly used materials are "521icru.pegs4dat" and "700icru.pegs4dat". The difference between the data sets is the cutoff energy for electrons used in generating the PEGS4 data sets, being 521 keV and 700 keV for "521icru.pegs4dat" and "700icru.pegs4dat" respectively. Both data sets use a cutoff energy of 10 keV for photons. The data sets are related to the BEAMnrc/DOSXYZnrc parameters global electron cutoff energy, ECUT, and global photon cutoff energy, PCUT. ECUT and PCUT define the cutoff energy for electron and photon transports in BEAMnrc/DOSXYZnrc code. As soon as an electron and photon total energy fall below the ECUT and PCUT respectively, their histories are terminated and their energies are deposited locally. AE and AP are parameters that determine the cutoff energy for the production of secondary electrons and photons, respectively. The global electron cutoff (ECUT) and photon cutoff (PCUT) must be greater than or equal to corresponding values for AE and AP.

3.3.5 BEAMDP (BEAM Data Processor) code

BEAMDP (BEAM Data Processor) is an interactive program, developed with OMEGA (Ottawa Madison Electron Gamma Algorithm) project [80]. BEAMDP can be used as a general-purpose BEAM utility program to analyze a PHSP data file for beam characterization models and derive the following characteristics: energy fluence; spectral distribution; energy fluence distribution; mean energy distribution; planar fluence; angular distributions; and the distribution of particle weights... etc., from an existing PHSP data file generated by BEAMnrc code simulation in a scoring plan.

3.4 Variance Reduction Techniques

A reliable estimate for the efficiency of a MC simulation requires a correct estimate of the statistical uncertainties. The efficiency (ϵ) for a given MC simulation is estimated by the following relation:

$$\epsilon = \frac{1}{T.s^2} \tag{3.1}$$

T is the time required to simulate N histories.

Obtaining a small value of the statistical uncertainty s and minimizing the time of simulation T are required to improve the efficiency of the simulation. The VRTs are employed for that purpose to speed up the simulation, and therefore achieve a high efficiency. There are different VRTs available in BEAMnrc/DOSXYZnrc codes.

These different VRTs could be used alone or combined in parallel calcul to achieve a high efficiency.

3.4.1 Range Rejection technique

Range rejection introduces the following approximation " in terminating a charged particles history and depositing all of its energy in the current region, it is suposed that any bremsstrahlung photons that would have been created by the particle, do not leave the current region". We can diminish inaccuracies resulting from this approximation using the input variable ESAVE_GLOBAL defining the maximum charged particle energy (MeV) at which range rejection is considered. The basic method is to calculate the range of a charged particle and terminate its history if it cannot leave the current region with energy > ECUTRR. ECUTRR is the range rejection cutoff energy which may vary from region to region depending on the type of range rejection used. To determine the range to ECUTRR, BEAMnrc calculates the range from ECUTRR to AE (the cutoff energy for the production of secondary electrons and photons) for each region at the beginning of the simulation. Then, before each charged particle step during a simulation, this value is subtracted from the particle's range to AE. Range rejection is used to save computing time during simulations.

3.4.2 Photon Forcing technique

Photon Forcing is useful for improving statistics of scattered photons when photon interactions are sparse (in thin slabs of material or in material with low density). Briefly, a photon forced to interact in a component module is "split" into a scattered photon whose weight is equal to the probability of interaction and an unscattered photon carrying the remaining weight. The unscattered photon proceeds as if an interaction did not take place, and it cannot be forced to interact any more within the specified forcing zone.

The feature of passing forcing parameters to secondary photons is particularly useful to get good statistics for bremsstrahlung photon interactions. This feature makes Photon Forcing a powerful tool for improving statistics when used combined with bremsstrahlung splitting. Note that forcing in restricted regions with low mass

can lead to a few electrons created outside the forcing region having much larger weights than those created inside the forcing region and thereby distorting results. One of the main purposes of implementing this option was to study the generation of contaminant electrons in a photon beam.

3.4.3 Uniform Bremsstrahlung Splitting (UBS)

UBS technique are applied to the higher order of bremsstrahlung and annihilation photons if Russian Roulette is on. Each bremsstrahlung event produces NBRSPL photons, each having a weight equal to NBRSPL times the weight of the electron that underwent the bremsstrahlung event. The splitting number, NBRSPL, is not applied to higher order bremsstrahlung and annihilation photons unless Russian Roulette is turned on. This prevents wasting simulation time.

3.4.4 Selective remsstrahlung splitting (SBS)

SBS used a variable splitting number, NBR, which reflects the probability that all bremsstrahlung is created on the front surface will enter the field defined by FS (field size) and SSD (distance from the front of the bremsstrahlung target at which the above FS is defined). FS bigger side of the treatment field plus 10 cm. E.g., 20 for a $10 \times 10\ cm^2$ field, this is used to define the relevant angle for the SBS routine. If Russian Roulette is on, it has found that NBRSPL maximum splitting number for SBS should be between 200 and 1000 to be used for higher-order bremsstrahlung and annihilation photons [80]. This should be set to $0.1\times$ NBRSPL to obtain the optimum gain in efficiency. SBS is more efficient than UBS (by a factor of 3-4) [80].

3.4.5 Directional Bremsstrahlung Splitting (DBS)

DBS was introduced into BEAMnrc in 2004 and results in even greater efficiency than SBS and UBS [86]. DBS began from the same philosophy as SBS, in which bremsstrahlung photons aimed into the treatment field are split at the time of the creation. The principal concept behind the bremsstrahlung splitting technique is to increase the number of photons in the field of interest in order to minimize the statistical uncertainty value and complete the simulation during a shorter time. DBS is not only employed for brem photons, but also used to split photons resulting from other interactions such as annihilation (Mainegra-Hing and Kawrakow, 2011) [52]. Three main parameters should be provided by the user to utilize the DBS technique for photon splitting : (1) the splitting number (NBRSPL), (2) the radius of the field of splitting (FS), and (3) the source to surface distance (SSD) at the FS. When a photon is produced, DBS splits it into NBRSPL photons with a statistical weight of (w = 1/N) in the final result. This technique is considered as the opposite of the splitting technique. It is based on using a value known as a survival threshold, or a survival probability, equal to (1/N). The introduction of this technique signifies that the majority of the simulation time is spent on transporting the particles that contribute to the quantity of interest, and doesn't wasting more time in simulating the other particles.

Comparison of these techniques (UBS, SBS, or DBS), It had established that DBS to be the efficient technique at low and high energies [86, 87]. The results have demonstrated that using DBS in a photon beam can result in fluence efficiencies up to 8 times higher than with SBS (up to 20 times higher than with UBS) and in dose efficiencies up 6 times higher than with SBS (up to 26 times higher than with UBS) [87].

3.4.6 Charged Particle Russian Roulette

When using UBS or SBS, following all of the secondary charged particles created by the "split" photons increases the CPU time required for simulations. If the main interest is the bremsstrahlung photons themselves, one can reduce the CPU time while still preserving the bremsstrahlung splitting advantages by using a Russian Roulette technique with any charged particles generated by the split photons.
Russian Roulette is implemented by giving secondary charged particles resulting from split photons a survival threshold. The survival threshold is the inverse of the photon splitting number. Thus, in case of UBS, the threshold is equal to NBRSPL, while in case of SBS, the survival threshold is NBR. Secondary charged particles subject to Russian Roulette are electrons resulting from Compton events, photoelectric events, and electrons-positrons resulting from pair production.
Splitting of higher-order bremsstrahlung and annihilation photons does not greatly increase computing time when Russian Roulette is on because most of the secondary charged particles have been eliminated.

3.4.7 Bremsstrahlung Cross Section Enhancement (BCSE)

The Bremsstrahlung Cross Section Enhancement (BCSE) variance reduction technique is introduced into BEAMnrc in the Fall of 2007 to improve the efficiency of simulations that involve x-ray production from bremsstrahlung targets (e.g. x-ray tubes and clinical linear accelerators) [88], both in the kilovoltage and megavoltage range. BCSE is compatible with all other variance reduction techniques already used in BEAMnrc (e.g. range rejection, UBS and DBS). BCSE can be used alone or in conjunction with UBS or DBS; however, the largest efficiency gains are achieved when BCSE is optimally combined with UBS or DBS. The efficiency gains can be up to five orders of magnitude over those obtained with analog simulations, and up to a full order of magnitude over those obtained with optimized splitting alone.

3.4.8 Photon Splitting technique

Photon splitting technique was implemented in DOSXYZnrc code. This technique has the same concept as that for the DBS technique. A user-defined splitting number (ns) is used to split the photon ns times when it enters the DOSXYZnrc geometry. Thus, split photons are given a weight of (w = 1/ns). The use of DBS in BEAMnrc and photon splitting in DOSXYZnrc was found to increase the simulation efficiency by a factor of up to 6.5 and ~ 2 for high and low energies, respectively [83, 89].

3.4.9 HOWFARLESS technique

The HOWFARLESS algorithm is only used in DOSXYZnrc code, and it is utilized for simulations carried out with phantoms made of a homogeneous medium [90]. As mentioned previously, the phantoms modeled with DOSXYZnrc code are formed of voxels of specific size. The phantom is formed of the outer boundaries (phantom size), and the inner boundaries (voxel size). A HOWFARLESS algorithm is based on transporting the charged particle without a restriction to the inner boundaries, i.e. ignoring the voxels boundaries, and only considering the extreme outer boundaries. Thus, the charged particle is transported in steps freely without the need to stop at each inner boundary. The simulation efficiency was found to increase by a factor of 2.9-5.4 when the HOWFARLESS technique was used with a BCA called EXACT, and by 51% - 89% with PRESTA-I BCA [90].

3.5 Errors and comparison of dose distributions in radiotherapy

3.5.1 Errors and uncertainties in MC calculation

Physicists are generally comfortable with the proposition that they routinely and unavoidably make errors in their measurements and calculations. The both terms uncertainty and error are often used interchangeably and have different meanings (ISO, 1995) [91]. The recommendations of the BIPM were approved by the Comite International des Poids et Mesures. When we make a measurement, we virtually do an error. So, an error is determined as the difference between the measured value of a measurable and the true value. Uncertainties of measurements are expressed as relative standard uncertainties, and the evaluation of standard uncertainties is classified into two types:

♣ Type A uncertainties are inherently random and are obtained by a statistical analysis of a series of observations.

♣ Type B uncertainties are determined through other than statistical, but often subjective, methods and account for systematic effects in the determination of a quantity.

The calculations results by MC are generally divided to two types of uncertainty A and B. The global uncertainty is expressed by the following expression [91]:

$$\sigma = \sqrt{\sigma_A^2 + \sigma_B^2} \tag{3.2}$$

Uncertainties non-statistical of type B are difficult to evaluate. They may be due to the accuracy of the physical models and cross sections data used in the code and programming errors. It is difficult to have an exact idea of the impact of these errors on the result of a given simulation, depending on the energy, the particle type, and the material studied. Salvat et al. (2006) given an idea of systematic uncertainties related to the cross section error for PENELOPE diffusion models [92]. In addition, various MC code evaluation tests [92–94] have shown excellent agreement between simulations and the experimental data thus confirm the diffusion models reliability implemented in the MC codes. The statistical uncertainties of type A, inherent to

MC calculations, are evaluated according to the conventional methods. If Q is the calculated value determined from a MC simulation with N histories, the mean value of Q is given by:

$$\bar{Q} = \frac{1}{N}\sum_{i=1}^{N} q_i \tag{3.3}$$

q_i is the calculated value for the i-th history. The statistical uncertainty σ_Q corresponding to the standard deviation divided by the mean is determined by the following relation [95]:

$$\sigma_{\bar{Q}} = \sqrt{\frac{1}{N} var(q)} = \sqrt{(\frac{1}{N})^2 \sum_{i=1}^{N} (q_i^2 - \bar{Q}^2)} \tag{3.4}$$

3.5.2 Radiotherapy errors (human, mechanical or computer)

The measured or calculated values of almost all quantities of interest in radiation oncology cannot be known exactly, but have some degree of uncertainty associated with them. The accidents in radiotherapy technique have been observed since the beginning of utilizing this technique [96]. Since then, the irradiation techniques have become increasingly sophisticated, and therefore more difficult to control. These complexities can cause new errors and induce differences between the described dose distribution and that produced. The implementation of multiple procedures quality controls and recommendations, detect potential errors. Task Group 100 and 142 of the AAPM [97, 98] are particularly important here. According to Klein et al. [98], the most frequent errors would be geometric (patient positioning, shape of the field). Table 3.1 provides a summary of errors that may be occurred.

TABLE 3.1: Potential errors in external radiotherapy.

Category	**Description**
Prescription	-Dose(total dose, fraction dose) -Contouring error (wrong location, bad rating)
Patient	- Incorrect patient immobilization and/or positioning, errors due to patient and organ motion, changes in patient during therapy.
Linac	-Accessory missing, not adapted or misused (filter, bolus, cache) - Shape of the field size (wrong position of jaws) - Collimator rotation - Rotation of the table - Choice of the energy of the beam - Different dose of the prescribed dose - Beam calibration error (energy, symmetry, homogeneity)
Plan of treatment	- choice of beam direction and field shapes,dose algorithms, plan evaluation.
Treatment delivery	- Incorrect treatment machine configuration, incorrect dose delivery

3.5.3 Comparisons of dose distributions in radiotherapy

Dose distributions, 2D or 3D, can be compared in different ways. The simplest method is to calculate the difference of the dose at any point and to compare it to a tolerance criteria. The difference of the dose and the DTA("Distance To Agreement") can be used together as criteria for the acceptability of calculated dose distribution. Venselaar et al. [99] proposed the acceptability criteria varying with region of the dose distribution. According to Bakai et al. [100] the parameters based on the dose criteria provide only a qualitative information, they allow to identify the regions of the calculated dose distributions without meeting the acceptability criteria, they didn't allow to give a quantitative evaluation of these dose distributions, so the tools based both on dose and distance criteria give quantitative information. Van Dyk et al. [101] are the first to propose quantitative evaluation methods to compare the measured and calculated dose distributions by TPS.

The concept of DTA has been developed by Low et al., and Hogstrom et al [102, 103]. The DTA is the distance between the measured and calculated points which have the same dose. The dose difference and the DTA are used as criteria for acceptability of a calculated dose distribution. The difference in dose and distance are two parameters to consider when irradiating a tumour:

♣ We try to irradiate homogeneously the tumor volume. It is a zone of low gradient dose and the difference in dose will be checked in this case.

♣ We must protect healthy tissue, so the important factor to take into account is the precise location of the tumor irradiation. It is a zone of strong gradient dose and the difference in distance will be verified in this case.

3.5.4 The γ-index

The gamma index is an evaluation tool based on the use of two acceptability criteria, the first Δd_{max} based on the distance and the second ΔD_{max} on the dose:

♣ In zone of low gradient dose, the differences of dose will be verified.

♣ In zone of high gradient dose, the differences in distance will be checked.

It is important to note that in our work the gamma index is only used when adjusting the parameters of the initial electrons by comparison, in a simple situation, between MC simulations and experimental measurements.

The γ index is used for the comparison of dose distributions. The γ-evaluation combines the difference dose criterion and the distance to agreeable (DTA) (D.A.Low et al [104, 105]). The function Γ is defined by:

$$\Gamma(x_r, x_e) = \sqrt{\frac{(x_e - x_r)^2}{\Delta d^2} + \frac{(D_e(x_e) - D_r(x_r))^2}{\Delta D^2}} \tag{3.5}$$

Where, D_r the reference dose (measurements), D_e is the dose to be evaluated (MC calculation), x_r is the abscissa of the reference point, x_e is the abscissa of the point to be evaluated, r is the abscissa of the reference point or the point to be evaluated, defined by x for 1D, (x,y) for 2D and (x,y,z) for 3D, $\Delta d = x_e - x_r$ and $\Delta D = D_e - D_r$.

$\Gamma(x_e, x_r)$ calculates the Euclidean distance (Euclidean normalized by ΔD and Δd) between two points of the reference distribution and the evaluated distribution. For example, for electron beams in a homogeneous medium, the usual criteria are set at

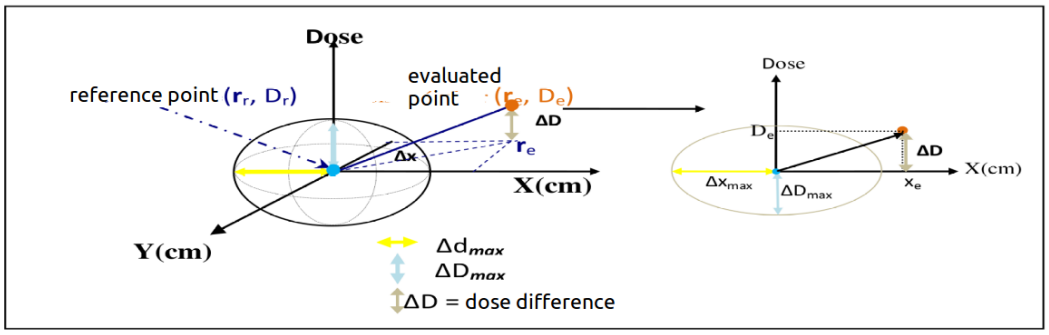

FIGURE 3.7: Schematic representation of the Gamma Index concept according to Low et al. [104].

2% for ΔD and 2mm for the DTA. The equation $\Gamma(x_e, x_r) = 1$ gives the surface of the ellipse which represents the acceptance criterion. If the measuring point is inside this ellipse, then the point is accepted (figure 3.7). We define the function γ by:

$$\gamma(x_e) = min\Gamma(x_e, x_r) \tag{3.6}$$

The computation of the function γ at a point of the distribution to be evaluated therefore consists in finding out which point of the reference distribution minimizes the distance $\Gamma(x_e, x_r)$.

If $\gamma(x_e) < 1$, then the point $(x_e, D(x_e))$ is considered acceptable. Otherwise it is located outside the ellipse of acceptability. It should be noted that the Gamma value is always positive. From this formalism we used an excel program to calculate the function γ. The program also calculates the interpolated γ function which makes it possible to avoid 'false negatives'due to the poor spatial resolution of the reference distribution in high gradient zones.

The gamma index is an international standard test used by the majority radiotherapy centres in the world between simulation and experiments results to validate the MC simulation in comparison with other validation test.

3.5.5 Relative difference of the absolute dose

To compare the dose distribution between measured (reference dose) and calculated dose (to be evaluated) Venselaar et al. [99] use the notion of relative difference of the absolute dose. They propose normalization in terms of local dose.

By normalizing the dose distributions to a local dose, a large differences in the doses was seen in low dose regions. To solve this problem, Venselaar et al. [99] propose, for these low dose regions, to normalize the difference dose at the same depth (as that of the point of interest) of the reference dose on the beam axis of the irradiation. In these low dose regions, an equation is given as:

$$\eta(\%) = 100\frac{(D_e - D_r)}{D_{r,axis}} \tag{3.7}$$

Where, $D_{r,axis}$ is the reference dose at the point of the same depth but located on the axis of incident beam, D_e is the dose to be evaluated, D_r is the reference dose.

Venselaar et al. propose to segment the dose calculated into several geometric regions (figure 3.8), which each geometric region having the different acceptability criteria (see table 3.2).

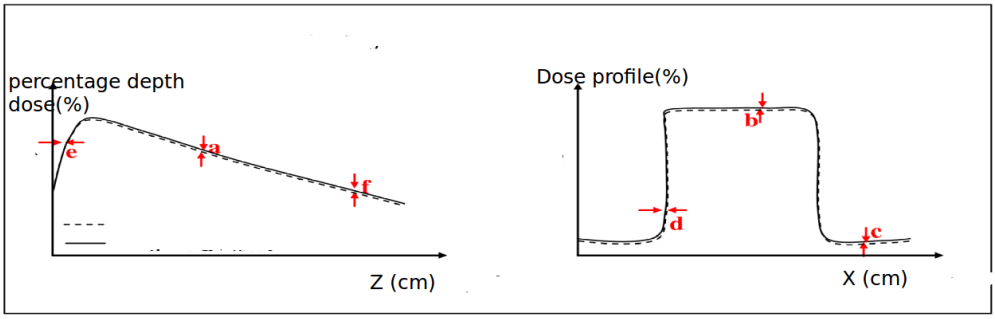

FIGURE 3.8: Regions and acceptability criteria for dose distributions.

3.5.6 Recommendations of the dose validation

Many literatures recommendations existed regarding the criteria in dose difference and DTA to validate the MC dose calculation [99, 105–107] for calculations with a simple irradiation field in a homogeneous phantom. For more complex fields or heterogeneous phantoms, generally more tolerant criteria are recommended as by Van Dyk et al. [106]. The most demanding criteria are those of the ICRU [107], which recommended the accurate calculation to be 2% in terms of relative difference and 2mm in DTA (see table 3.3). However, Venselaar et al. [99] (see table 3.2) propose much more flexible criteria in low dose areas (outside the beam in particular)to be 3%. Therefore, the same absolute difference dose had similar clinical consequences in the high and low dose regions, but this difference is expressed to the relative dose at the considered point (it is more important in the low dose regions). Difference can be calculated to the relative dose on the axis. However, we will like to present the difference in the relative dose at the point considered for the consistency and caution, but it must be kept in mind that if the dose is low (see table 3.4), a relatively large relative difference does not necessarily have to be worrying. Proposed dose calculations in commercial phantoms are validated during installation for a given treatment device. Audits are regularly verified the modeling of the device in TPS to give the correct calculations in relation to the measurements.

TABLE 3.2: Acceptability criteria according to Venselaar et al. [99].

region	**Simple and homogeneous geometry**	**complex and homogeneous geometry (filter, bolus MLC..etc**
central axis	2%	3%
build up and penumbra regions	2mm or 10%	3mm or 15%
Exterior of beam axis	3%	3%
out field of beam	3%	4%

TABLE 3.3: Acceptability criteria for relative dose calculations in photon external radiotherapy, proposed by different authors. The percentages are expressed in relation to the local dose.

Reference	**Low dose gradient (%)**	**High dose gradient(%)**
[Mc Cullough and Krueger 1980] [108]	3	4
[ICRU 1987] [107]	2	2
[Dahlin et al. 1983] [109]	3	3
[Brahme et al. 1988] [110] - central axis - Outside central beam axis	 1.5 3	 3 3
[Fraass et al. 1998] [111](AAPM TG-53)(square fields, homogeneous phantoms) - central axis - Outside central beam axis - penumbra region - Outside beam edges	 1 1.5 - 2	 - - 2 -
[Venselaar et al. 2001] [99] simples geometries (homogeneous phantom) - central beam axis - inside beam - penumbra region - outside beam	 2 3 - 3	 - - 2 -

TABLE 3.4: Tolerance acceptability criteria for relative dose calculations in photon external radiotherapy for low and high dose gradients in different field regions [112, 113].

Region	**Homogenous simple geometry**	**Complex geometry (wedge, asymmetry, MLC)**	**More complex geometry**
Central beam axis data high dose, low dose gradient	2%	3%	4%
Build-up region of central axis beam, penumbra region of the profile high dose, high dose gradient	2mm or 10%	3mm or 10%	3mm or 10%
Outside central beam axis region high dose, low dose gradient	3%	3%	4%
Outside beam edges-low dose, low dose gradient	30%	40%	50%
Radiogical width-high dose, high dose gradient	2mm or 1%	2mm or 1%	2mm or 1%
Beam fringe-high dose, high dose gradient	2mm	3mm	4mm

Chapter 4

Modeling and Simulation of SATURNE 43 Linac

4.1 Modeling of SATURNE 43 and geometry views

4.1.1 Introduction

The SATURNE 43 accelerator modeled in that work, is a medical linac of National Laboratory Henri Becquerel (LNHB) at CEA (Commissariat of Energy Atomic) in France. This accelerator is well characterized, which makes it an experimental tool to meet the increased requirements on precise dose evaluation on new treatment modalities in radiotherapy. The geometrical data and the composition of different materials, necessary for validation and comparison between the data obtained using MC BEAMnrc code calculation and measurements [114]. Figure 4.1 gives an image of the accelerator SATURNE 43 of LNHB at CEA in France.

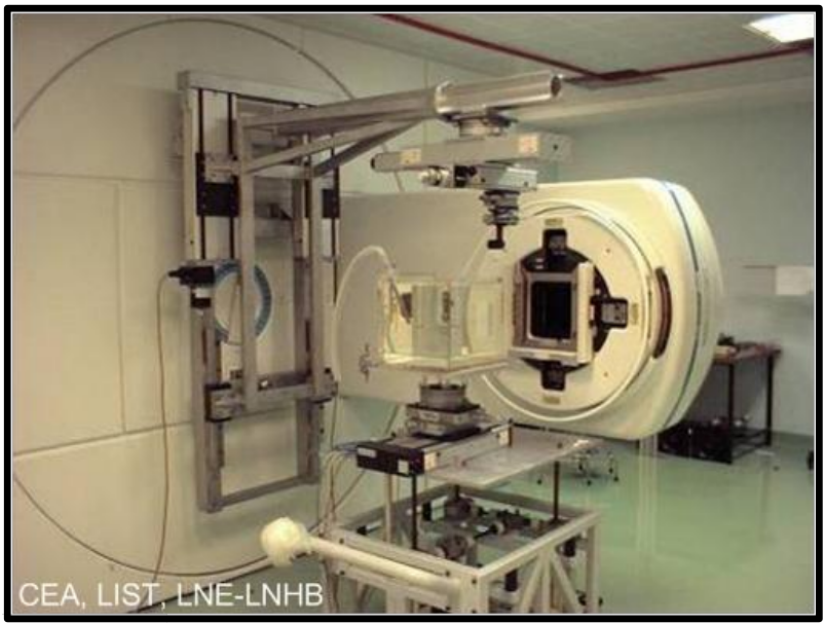

FIGURE 4.1: SATURNE 43 medical linac of LNHB in France.

4.1.2 Description of head's linac SATURNE 43

The head's linac of SATURNE 43 (Figure 4.1) contains the full system for producing and shaping the photon beam for treatment utilization. It is essentially composed of a tungsten target, a flattening filter, a monitor chamber and collimators that shape the field size of the irradiation beam. The detailed informations (dimensions and the positions) in the space of the different components of the head's linac SATURNE 43 are given in appendix B.

4.1.3 Modeling of SATURNE 43 with BEAMnrc

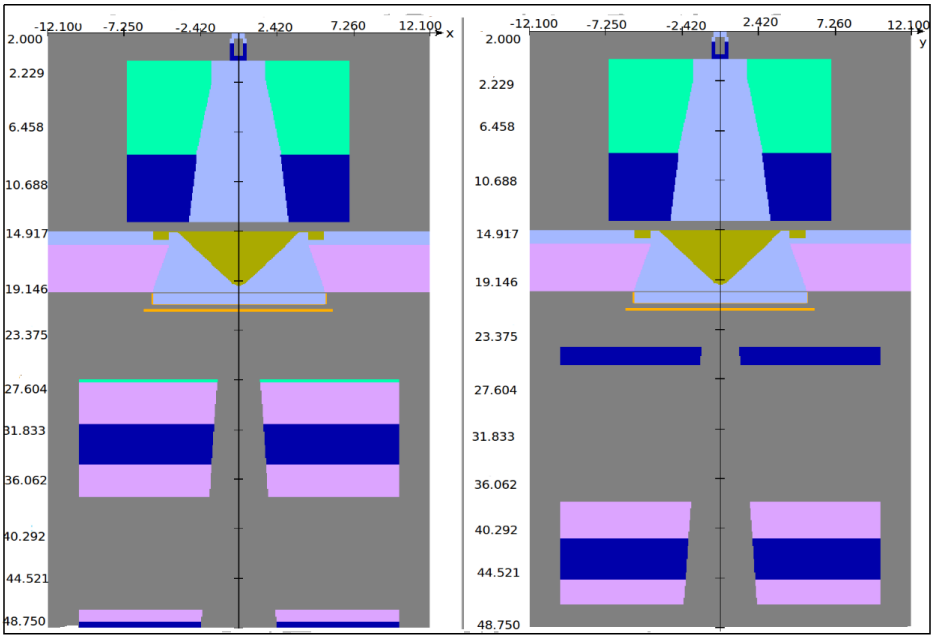

FIGURE 4.2: Visualization left-(XZ) and right-(YZ) sections of SATURNE 43 on 12 MV modeled with BEAMnrc code.

Figure 4.2 shows two global views of the model geometry of SATURNE 43 head's linac with BEAMnrc code in two sections XZ and YZ, respectively. The origin of our geometry is the upper face of the tungsten target.

In figures 4.3 and 4, we represent the model of SATURNE 43 with a $40 \times 40 \times 40$ cm^3 water phantom in two 2D and 3D views, respectively.

The geometry of the head's linac SATURNE 43 is given with a maximum details in the description of EURADOS [114]. The materials constituting the different components are also explained with good precision. Thus, the modeling of the head's SATURNE 43 with BEAMnrc code must represents an exact modeling of this accelerator.

In this work, the model of the accelerator SATURNE 43 was written in the format of the input data of the BEAMnrc code. The different geometric shapes are modeled using components implemented in BEAMnrc code. The BEAMnrc code have the advantage of the writing of the input file using the BEAM GUI which a user interface to facilitate modeling the geometry of linac.

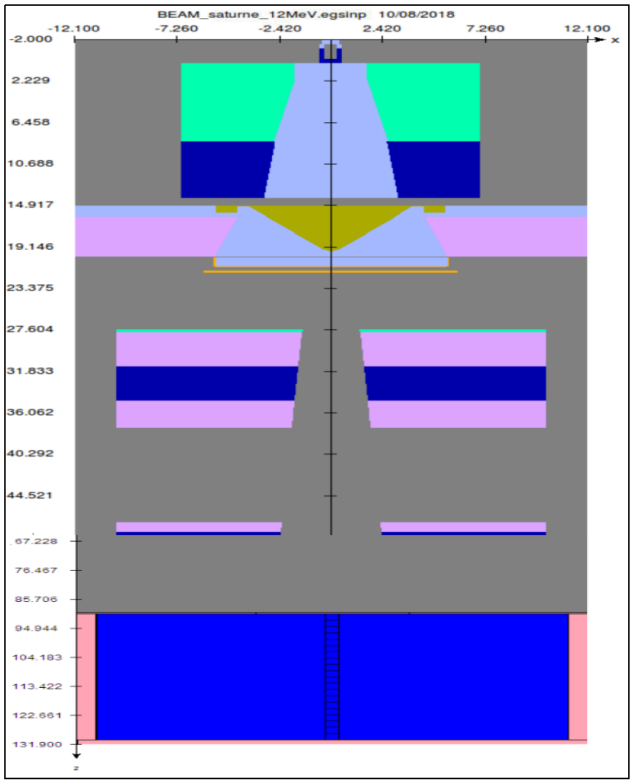

FIGURE 4.3: Visualization (XZ section) of the head's linac SATURNE 43 on 12 MV with a water phantom placed at 90 cm from Tungsten target modeled with BEAMnrc code.

In the following parts of this section, we will discuss the role and model of each component of the SATURNE 43 accelerator head and present the diagrams of the different parts of the model as reproduced using the interface graphical tool of the BEAMnrc code.

4.1.3.1 Tungsten target

In our simulation, we are interested in the production of bremsstrahlung x-ray beams produced in tungsten (material of high atomic number) target. Generally, tungsten is used with a large thickness to stop the accelerated primaries electrons favoring the production of bremsstrahlung photons. The stopping of the primaries electrons is important to avoid any contamination of the x-ray bremsstrahlung beam. The thickness of the target is then chosen according to the energy of the beam: 2 mm for beams of 4, 6 and 8 MV and 4 mm for beams of 10, 12, 15, 18, 20 and 25 MV. We modeled the target as a titanium window which allows to ensure the vacuum in the deflection coils according to the data provided by the manufacturer. Figures 7.5 and 6 show the model of the target and the titanium window of the SATURNE 43 accelerator.

4.1.3.2 Primary collimator

After the tungsten target, the generated photon beams are intercepted by a primary collimator component. The primary collimator have a conical shape, defined the

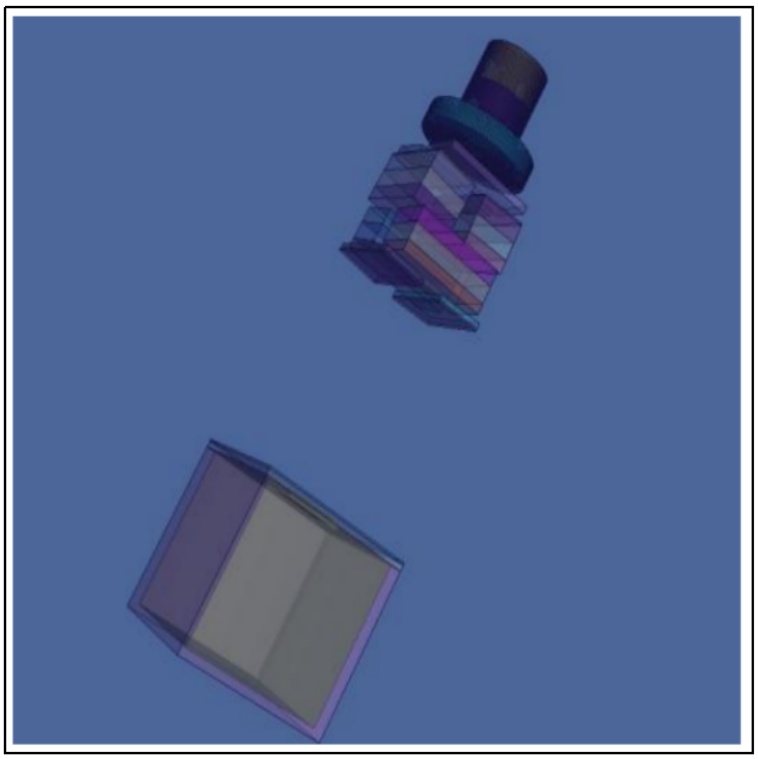

FIGURE 4.4: 3D visualization of head's linac SATURNE 43 with the water phantom.

maximum field size of irradiation beam. This is the first collimation to stop the maximum scattered radiation to healthy tissue that could be irradiated the patient unnecessarily and leave only the useful beam of photons for treatment field.

We have modeled the primary collimator by the intersection of a cylinder and a cone. The cone contains air to allow the passage of photons from the target. The volume collimator consisting of the cone and the cylinder is divided into two parts. The first part is made of material XC10 and the second part of Denal. Figures 4.6 represents the primary collimator modeled with BEAMnrc code.

4.1.3.3 Flattening filter and secondary collimator

The role of the flattening filter component is to homogeneize the dose at the level of the irradiation field size. The photons produced in the target have a preferred direction towards the front. The flattening filter has the conical shape and generates a flat dose distribution at depth of 10 cm in the water. Various studies have been interested on the modeling of flattening filter to evaluate the effect of the cone on the spatial and energetic fluence distribution of photons [115–117].

We modeled the flattening filter as a set of cones and cylinders. The cone has the height of 4.6 cm and its base is confused with a cylindrical support of height 0.65 cm and 5.4 cm radius. The geometry of the cone is symmetrical with respect to the axis of the beam. The cone and its support are made of stainless steel.

The cone is inserted in a collimator of lead conical shape. The modeling of the flattening filter and the secondary collimator are presented in 2D in figure 4.7.

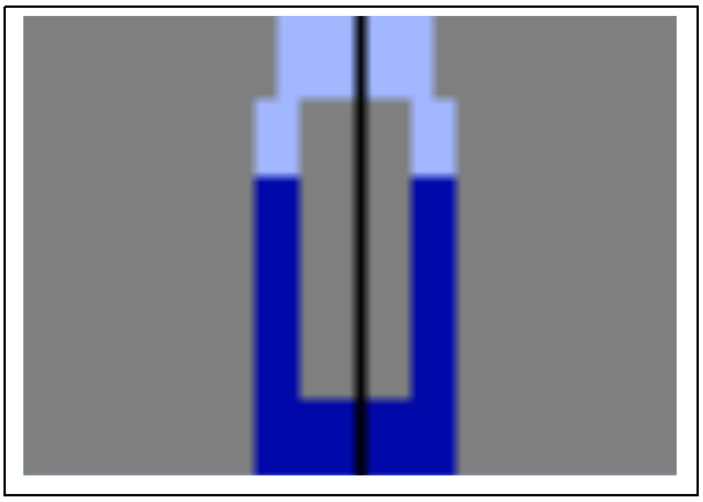

FIGURE 4.5: Target and Titanium window modeled with BEAMnrc.

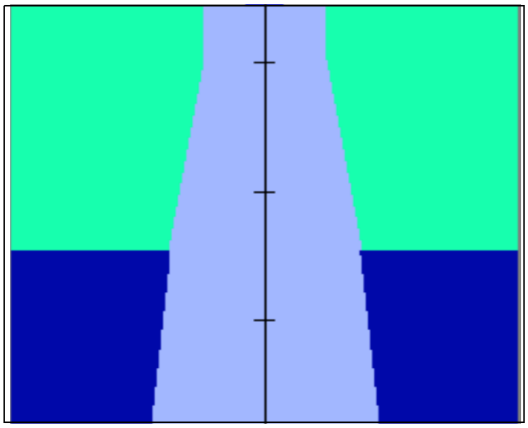

FIGURE 4.6: Primary collimator modeled with BEAMnrc code.

4.1.3.4 Monitor chamber

Figures 4.8 shows the two chambers with air cavities with aluminum-kapton walls and a aluminum anti-backscattering window.

A set of ion chambers called monitor chambers aiming to measure the dose delivered to patient and control the system to stop irradiation when the prescribed dose is reached. They also regulate the dose rate delivred and control the beams homogeneity and symmetry. For patient safety, two ion chambers connected to two independent reading systems are used. The response of the chambers to the dose rate is expressed in monitor unit (UM). Below the ionization chamber, we find an anti-backscattering window which is used to avoid the contamination of the ionization chamber by backscattered electrons on the jaws.

4.1.3.5 Jaws X and Y

The field size of the irradiation beam is provided by pairs movable jaws whose edges are oriented so as to minimize the geometric penumbra.

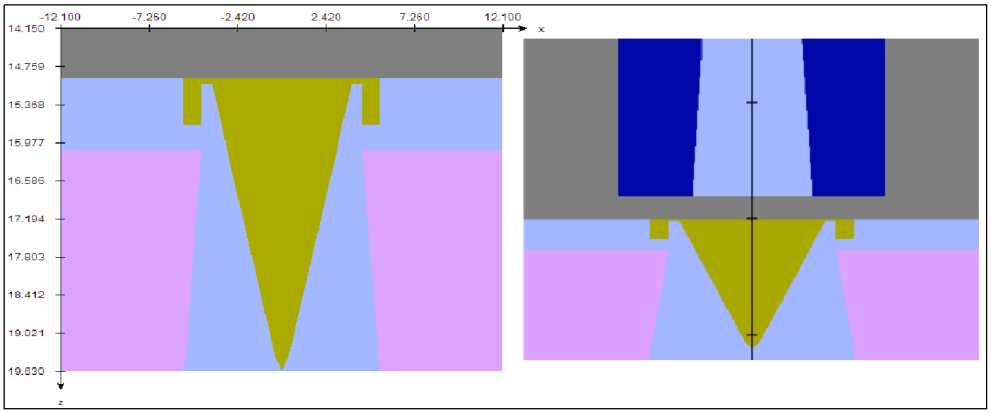

FIGURE 4.7: Visualization 2D (XZ) of flattening filter and secondary collimator modeled with BEAMnrc code.

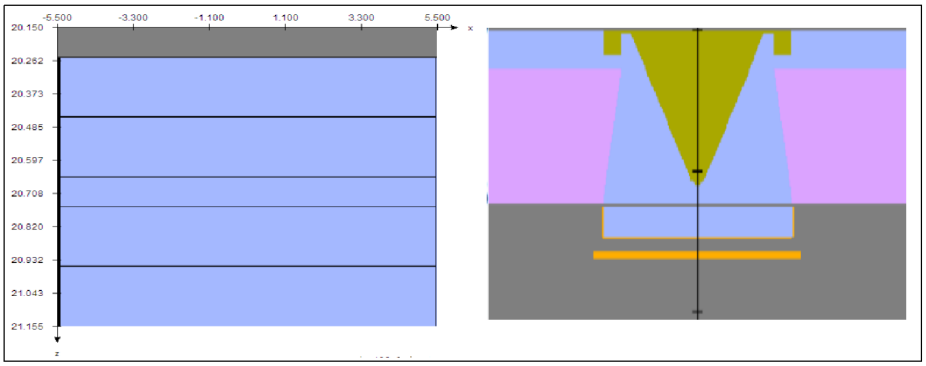

FIGURE 4.8: Visualization 2D (XZ) of ionization chamber and anti-backscattering window modeled with BEAMnrc code.

A pair of jaws consists of two blocks of heavy material placed at two different position. By changing these pairs of jaws, we modify the aperture forming the treatment field size. In this way, with each pair of jaws, the field size is limited along a given axis. As the pairs of jaws are oriented perpendicularly to beam axis, the field size is controlled along the X and Y axises. Generally, the movements of the blocks are independent of each other; the opening of the jaws can form symmetric and asymmetric field size. Figures 4.9 and 10 show the pairs jaws X and Y modeled with BEAMnrc code in two dimension views XZ and YZ.

4.1.4 Materials of SATURNE 43 head's linac

The composition of different materials and its densities forming the components of SATURNE 43 linac are shown in table 4.1. For example, the flattening filter was composed of stainless steel of density 7,8 g.cm^{-3} with the following compositions Mn(2%), Si(1%), Ni(10%), Cr(18%), Fe(69%).

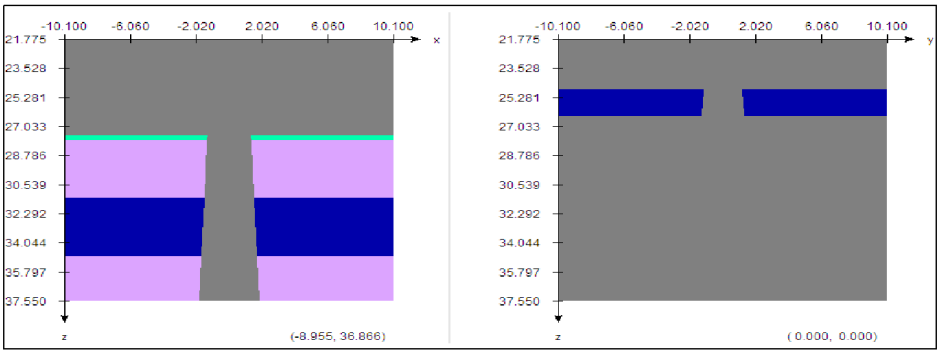

FIGURE 4.9: Visualization 2D of jaws1 modeled with BEAMnrc code.

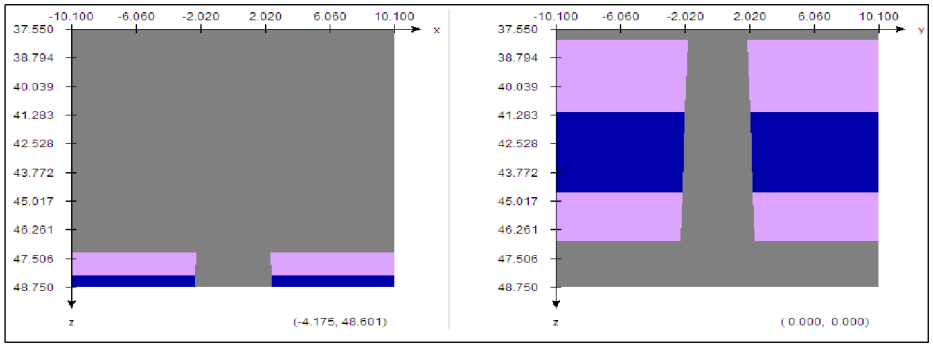

FIGURE 4.10: Visualization 2D of jaws2 modeled with BEAMnrc code.

4.2 Influence of initial properties of incident beams

4.2.1 Introduction

In order to calculate the dose distributions with BEAMnrc/DOSXYZnrc code, the BEAMnrc must be first used to generate the PHSP file at the output of the head's linac. Two steps are then necessary: (1) the geometrical modeling of the irradiation head and (2) the determination of the characteristics of the primaries electrons beam at the exit of the magnetic deflection chamber.

Unfortunately, data on the linac is not always known precisely. For example, the mutiple characteristics of the primaries electrons beam (energetic, spatial and angular distributions of these electrons) are relatively poorly known and difficult to measure.

This section therefore proposes a new method for adjusting the initial energy distribution of a linear accelerator. The aim is to determine the energy spectrum of the primaries electrons by using MC BEAMnrc simulations in order to better adapt the dose distributions calculated to those measured. This new method has been applied to the simulation of beams from the LNHB SATURNE 43 linac. The gamma index was used to assess the concordance between simulated and measured dose distributions.

The first part of this section gives a brief overview of previous works on MC simulation of linac beams, with emphasis on the results sensitivities to the initial parameters (energy, spatial and angular distributions of primary electrons) and to the details of the geometry of the irradiation head. The second part describes the

TABLE 4.1: Material, composition and density constituting the component of SATURNE 43 linac.

Components	**Materials**	**Composition (%)**	**Density (g/cm^3)**
Window	Titan	–	4.54
Target support	Tungsten	–	19.3
Target	Tungsten	–	19.3
Primary collimator	Denal XC 10	W(90,5), Ni(7), Cu(2,5) C(0,1), Mn(0.6), Fe(99.3)	16.8 7.8
Flattening filter	Stainless Steel	Mn(2), Si(1), Ni(10), Cr(18), Fe(69)	7.8
Secondary collimator	Lead	–	11.35
Monitor chamber	Kapton	H(2,64), C(69,11), N(7.33), O(20.92)	1.42
Window anti-backscattering	Aluminum	–	2.7
Jaws	Denal Plomb	W(90,50), Ni(7), Cu(2,5) –	16.8 11.35

method developed to optimize and determine various parameters of the primary electrons beam. After this parity, the third part deals with the validation of this method applied for the respective simulation of the beams from the SATURNE 43 accelerators.

4.2.2 Effect of incident beam parameters on the dose distributions

4.2.2.1 Source beam parameters and dose distributions

The sensitivity of dose distributions to the parameters of the initial beam of a linac has already been the subject of many studies. The influence of these parameters on dose distributions depends both on the type of accelerator, the nature of the beam (electron or photon) and the size of the field.

There are various previous studies, those of Lovelock et al., Sheikh-Bagheri et al., Sheikh-Bagheri and Rogers, Verhaegen and Seuntjens, Pena et al., Tzedakis et al. [118–123] who focused on different types of accelerators (Varian, Siemens and Elekta) and different energy points in electron and photon modes. This work shows that four main parameters characterizing the primary electron source can have an influence on the dose distributions: the average energy, the energy distribution, the spatial distribution and the angular distribution of the primary electron beam.

4.2.2.2 Mean energy

The mean energy of the primary electrons is the parameter that has important effect on the percentage depth dose. The sensitivity of the percentage depth dose to this parameter is of the order of 200 keV for the electron beams (that is, a change in the initial energy of 200 keV corresponds to a change of 1 mm the practical path of the electron beam in the water). This sensitivity is lower for photon beams.

Sheikh-Bagheri and Rogers [120] studied the effect of altering this parameter on large-field dose profiles, for several photon energy points produced by different accelerators (Elekta, Varian and Siemens). The results show that an increase in beam energy rounds the profile by decreasing the dose at the edge of the plateau and in the penumbra and this linearly as a function of energy. Bjork et al. [124] have been studied electron beams on an Elekta accelerator and found that the DP has less variations in the energy of the primary electron source.

4.2.2.3 Energy distribution

For a constant average energy of the primary electron beams, the modification of energy distribution influences the percentage depth dose. Some authors have noted changes in the local dose of up to 1.5% for an 18 MV photon beam [121].

Other studies on photon beams by Sheikh-Bagheri and Rogers [120], on electron beams by Bjork et al. [124], have shown that the electronic equilibrium zone (build-up) is sensitive to the distribution in energy of the spectrum of primary electrons. A slight asymmetry in the energy distribution had a direct effect on depth dose in first depths. The effects are very low on dose profiles.

4.2.2.4 Spatial distribution

Many literature studies have shown that percentage depth dose with photon Lin et al., Sheikh-Bagheri and Rogers, Tzedakis et al. [121, 123], and electron modes with Bjork et al. [124] are insensitive to variations in the spatial distribution of primary electron beams. This is justified by the fact that the dose along the axis is mainly deposited by particles near the axis.

For dose profiles influences, the results of studies by Sheikh-Bagheri and Rogers, Tzedakis et al. [120, 123] for large fields with photon mode show that increasing the diameter of the source leads to a decrease in the off-axis dose values. That explained by the fact that the central region of the profile is directly subjected to the photons coming from the beam.

For incident electron beams, the influence of this parameter on simulated dose distributions has been studied by Bjork et al. [124] for an Elekta accelerator. This work shows that dose profiles are insensitive to changes in the spatial distribution of primaries electrons.

4.2.2.5 Angular distribution

For photon beams, it has been shown that a change in the divergence of the primary electron beam has no effect on the percentage depth dose and poor effect on the dose profiles [119, 120]. In large field profiles, a 1 $^{\circ}$ divergence may result in less than 1% decrease in off-axis doses for 18 MV photons from a Varian accelerator [120].

For electron beams, Bjork et al. [124] have shown that the influence of the angular beam distribution on MC results is very small.

4.2.2.6 Dose distributions and geometrical linac components

With regard to the influence of various geometrical components of the irradiation head (dimensions, atomic compositions and densities) on the MC results of photon beams simulation.

In photon mode, the primary electron beam strikes a high atomic number to produce bremsstrahlung photons. The photon beam then passes through a FF to homogeneize the energy deposition distribution. Previous studies; Lin et al., Ding, Sheikh-Bagheri and Rogers, Libby et al., and Franchisseur [120,125–128] have shown that the DP are very sensitive to the geometry, composition and density of the FF. Moreover, the attenuation of the photon beam by the monitor chamber and mirror was negligible. They also showed that the collimation jaws do not have a significant effect on the energetic and angular distributions of photons.

4.2.3 Conclusion

In conclusion, in order to perform a precise MC simulation of a beam resulting from a linac and thus to have results comparable to the experimental measurements, two conditions are necessary: the geometrical parameters of the components of the the accelerators must be rigorously modeled according to the information provided by the manufacturer; the properties of the primary electron beams must be optimized with precision.

This review of literature studies has shown that there are a large number of parameters to adjust in order to achieve the precision required for the calculation of the dose. The existing methods of optimizing parameters are empirical methods, based on a priori knowledge of the solution and long in computing time. These methods used the various and dependent adjusted parameters to optimize the simulated results with experiments.

4.3 Simulation of SATURNE 43 linac with BEAMnrc

4.3.1 Introduction

Many authors have been studied the influence of the parameters of the initial beam of a linac to the dose distributions. The influence of these parameters on dose distributions depends on the nominal energy of accelerator, the nature of the beam (electron or photon) and the field size.

Lovelock et al., Sheikh-Bagheri and Rogers, Verhaegen and Seuntjens, Pena et al., Tzedakis et al., Lin et al. [118, 120–123, 125] have been worked on different types of linacs (Varian, Siemens and Elekta) with different nominal energies for both electron and photon modes. These previous authors have been established that the main parameters characterizing the primary electron source can have an influence on the dose distributions: the mean energy, the energy distribution, the spatial distribution and the angular distribution of the primary electrons beams.

The energy and the spatial distribution of the beam at the exit of the bending magnet are unknown parameters. It is therefore necessary to optimize the previous parameters to reproduce the experimental dosimetric results of the linac.

The medical accelerator SATURNE 43 works in photon and electron modes. The nominal energy of the electron beam is 12 MV. The knowledge of real energy, which may be slightly lower or higher than the nominal energy, is decisive for an adequate dosimetry with the MC method. The characteristics (mean energy, distribution of energy, spatial distribution and angular distribution of the primaries electrons beam) of these distributions must be accurately known to improve the agreement between experiment and MC calculation in gamma index comparison.

In our simulations of dose distributions in the homogeneous water phantom, we have adopted an elementary volumes in the form of cubes (voxels) of $0.5 \times 0.5 \times 0.5$ cm^3. The calculation of the absorbed dose is done by the code DOSXYZnrc which gives the energy deposited in a voxel.

For the calculation of the percentage depth dose, we normalized the dose at the depth of 10 cm from the entrance surface of the phantom (z = 90 cm) as (D_z/D_{10}). The first voxel, smaller in size than the others due to the presence of a plexiglass window (PMAA) at the entrance surface of the phantom, will not be considered in the analysis and comparison of the results. For the calculation of the profile dose at a depth of z = 10 cm, the dose was calculated along the x axis of the water phantom between x = - 11 cm and x = + 11 cm.

All the studies characterizing the electron beam for the SATURNE 43 medical linac concern a 10×10 cm^2 square field size were realized by the BEAMnrc code. In fact, the experimental data available for the values of the percentage depth doses and the profile doses measured on irradiation field of 10×10 cm^2.

4.3.2 Methodology of the simulation

4.3.2.1 Model of SATURNE 43 with BEAMnrc/DOSXYZnrc code

The model of the SATURNE 43 linac is divided into two parts:

¶Model M1: modeling of the components of the accelerator head with the BEAMnrc code by registering a PHSP file at the distance of 50 cm below the bottom jaws.

¶Model M2: use the PHSP file scored at the distance of 50 cm as a source and modeling the water phantom with the code DOSXYZnrc.

¶Simulation of 3×10^9 histories to score the PHSP file at a plan placed at distance of 50 cm from the Tungsten target using the M1 model.

¶Calculation of the absorbed dose in a water phantom for the model M2 where, particles generated from the PHSP file are: the number of incident particles from original sources, number of particles in PHSP files, number of photon and electron were 3×10^9, 75671419, 75337150 and 334269, respectively. PHSP file was placed at a distance of 40 cm from the entrance surface of the phantom. DOSXYZ parameters such as the particle production threshold and transport energies for electron (ECUT) and photon (PCUT) were 521 and 10 keV respectively. The particles in each phase space were recycled 10 times in order to achieve a statistical 1 σ uncertainty less than 1% in all dose points. Default EGSnrc transport parameters are applied in our simulations.

The total simulation times (for the creation of the PHSP file and the simulation in the phantom) on a desktop core i7 CPU with 8 GHz RAM on Ubuntu 14.04 system is about 144 hours.

4.3.2.2 Experimental data

The experimental measurements of the dose distributions was given by the National Laboratory Henri Becquerel (LNHB) [114]. PDD and DP were measured in a 40 $\times$ 40 $\times$ 40 cm^3 water phantom using a PTW-31002 cylindrical ionization chamber (see the figure 4.11). The entrance surface of the phantom was placed 90 cm from the tungsten target and a square field size of 10 $\times$ 10 cm^2 was defined at 100 cm from the target [129]. PDDs were measured on the beam axis between depth 0 and 24 cm and the DPs were measured at 10 cm depth perpendicular to the beam axis. Figure 4.12 and 13 illustrate the PDDs and DPs distributions of medical linac SATURNE 43 in a homogeneous water phantom. Experimental errors are less than 1% for 1σ.

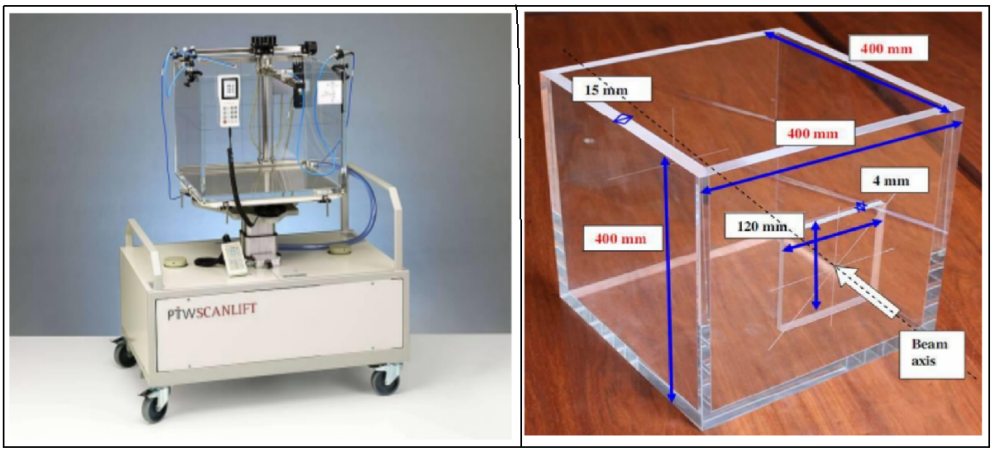

FIGURE 4.11: Water phantom MP3-P used for experimental measurement in LNHB.

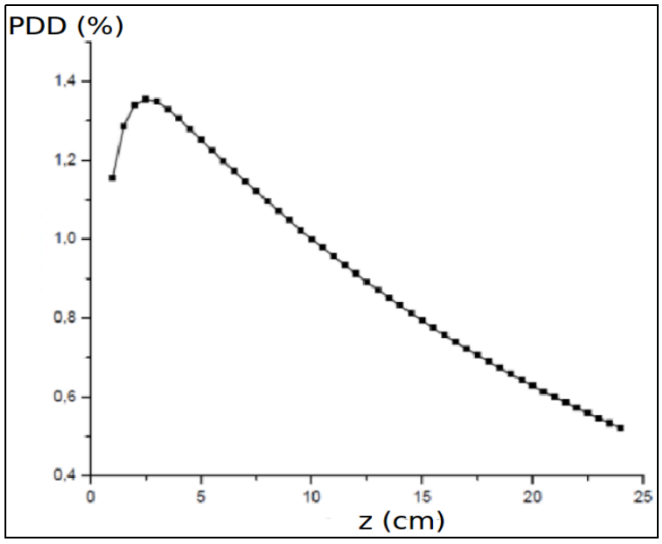

FIGURE 4.12: Curve of experimental PDD on a 12 MV SATURNE 43 linac normalized at depth 10 cm on field size of 10 $\times$ 10 cm^2.

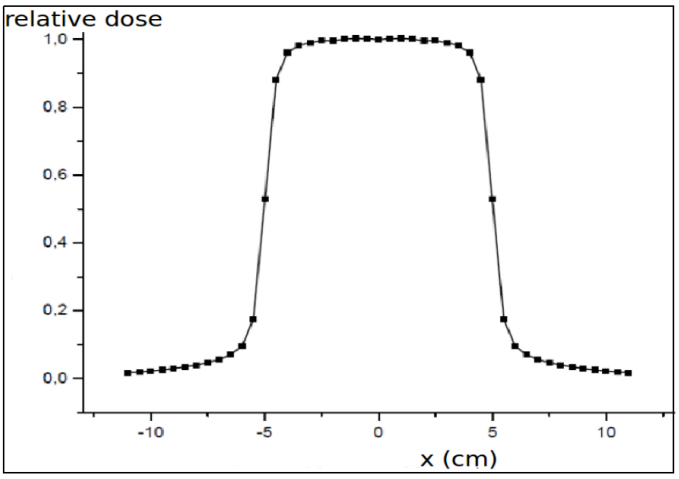

FIGURE 4.13: Curve of experimental DP on a 12 MV SATURNE 43 linac normalized at depth 10 cm on beam axis on a field size of $10 \times 10\ cm^2$.

4.3.3 Results and discussions

4.3.3.1 Spectrum of energy at the exit of SATURN 43 head's linac

Figure 4.14 shows the energy spectra of the different types of particles (photons, electrons and positrons) obtained at the exit of the accelerator SATURNE 43 placed at the distance 50 cm from the tungsten target. These spectra are relative to the photon beam of 12 MV, field size of $10 \times 10\ cm^2$, considering the energy spectrum of the primary electrons previously determined.

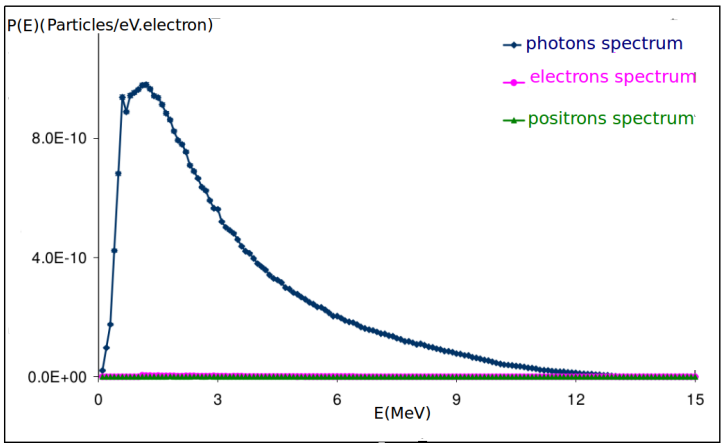

FIGURE 4.14: Energy spectrum of photons, electrons and positrons at the distance 50 cm below the bottom jaws on a field size of $10 \times 10\ cm^2$.

From this figure, we note that the electron and positron components in the spectrum are negligible compared to the photon component. It is a continuous spectrum of x-rays which the energy shows a maximum energy of the primary electrons. The peak observed at 511 keV is due to the annihilation of the positrons resulting from the creation of pairs. The mean energy of beam is 3.26 MeV. This value is compatible with that found by Blazy [130], 3.24 MeV.

4.3.3.2 Distributions of the dose

For the 12 MV photon beam, the manufacturer considers a mean energy of 12 MeV. Mazurier [131] was found the mean energy of the initial electrons at the origin of this photon beam was very close to the energy of 12 MeV announced by manufacturer. More recently, Blazy [130] has chosen a Gaussian energy distribution of primary electrons, with an average energy of 12 MeV and a standard deviation of 450 keV.

The first parameter to optimize is the energy of the electron beam with uniform distribution. We tested 5 energy values distributed in the range of 11.4 to 12.2 MeV in steps of 200 KeV, every test is carried out in three steps. firstly, we construct the PHSP file for these energies. In the second step, we calculate, depending on the depth in the water phantom, the dose deposited by each PHSP for a field size of $10 \times 10\ cm^2$ and a water source surface distance of 90 cm. Finally, the third step is to compare calculated DPs to those measured for the SATURNE 43 accelerator. We determine the mean kinetic energy of the incident electron beam, when there is a good agreement between the different quantities of comparison by adopting the different criteria discussed previouly (the gamma index, the quality index and z_{Dmax}).

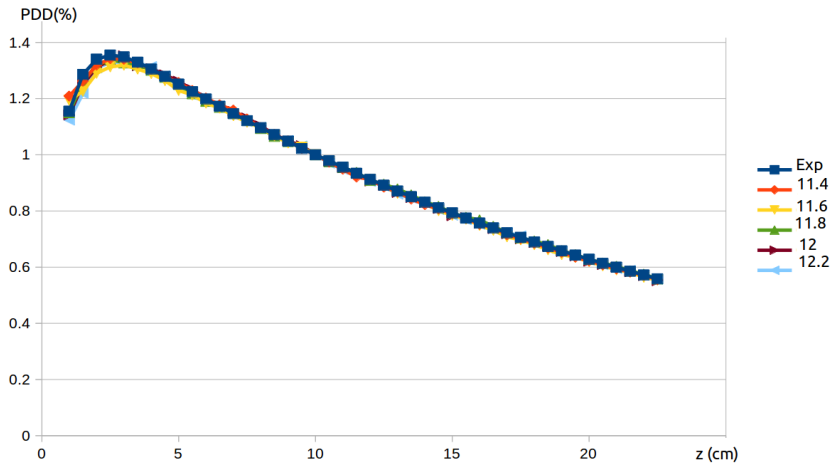

FIGURE 4.15: Variation of PDD with energy normalized at depth 10 cm on a field size of $10 \times 10\ cm^2$.

Figures 4.15 and 16 give the calculated PDD for different beam energies and the DP for 11.8 MeV energy. We have chosen some energy values in these figures, to study the evolution of the PDD and profile dose with the energy of the incident beam. Clearly, we see in Figure 4.15 that the absorbed dose increases when the incident electron energy increases. Similarly, the difference between the different curves increases from the surface dose to the maximum dose. Beyond the maximum dose, the curves of PDD seems to be reduced with depth. Also, figure 4.15 shows that the surface dose decreases with the energy of incident radiation.

Figure 4.16 shows the DP for different energy. We note that the profile dose is also very sensitive to the energy of the incident electron beam. The results show that an increase in beam energy tends to increase the dose in both regions: central and penumbra regions. On the other hand, out-field doses of the profile are less sensitive to incident energy.

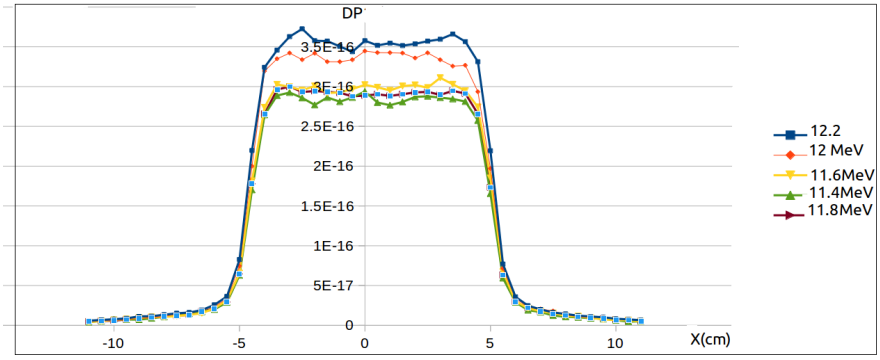

FIGURE 4.16: Variation of the DP with energy on a field size of 10×10 cm^2.

All our calculations was have a tolerance of 1% as an acceptable criterion for our MC simulations with respect to the reference measurements, because the LNHB experimental results measures the absolute doses with uncertainties of the order of 0.4% at 1 σ. The region of the build-up of the PDD was evaluated to 1%. These uncertainties associated with measurements and calculations are very small, so they are not represented in the figures 4.15 and 16. The statistical uncertainties associated with different calculation regions for PDD and DP are summarized in Table 4.2.

TABLE 4.2: The statistical uncertainties associated with different calculation regions for PDD and DP.

Depth (cm)	**Statistic incertitude (%) for PDD**	**Distance from the beam axis**	**Statistic incertitude (%) for DP**
1	1.1	0	1
2.5	1	2	1
10	1	5	1.2
20	1.1	8	3*

* region out field

Figures 4.17, 18, 19, 20, and 21 show the comparison of the measured and calculated dose when changing the incident electron energy between 11.4 and 12.2 MeV by step of 0.2 MeV as well as the gamma index of each comparison. The curves are normalized to a depth of 10 cm and are given for a field size of 10×10 cm^2 and a water source-surface distance of 90 cm.

Figures 4.22 presents the comparison of measured and calculated DP for mean energy value of 11.8 MeV as well as the gamma index obtained in comparison. The curve is normalized to the dose on the beam axis; it is calculated for a field size of 10×10 cm^2 at a depth of 10 cm in the water phantom.

To analyze the results obtained for the PDD we add two criteria: the depth of maximum dose Z_{Dmax} and the $TPR_{20,10}$ by calculating the relative difference Δ corresponding to the difference between the $TPR_{20,10}$ calculated and measured:

$$\Delta = \left| \frac{TPR_{20,10}(BEAMnrc) - TPR_{20,10}(measured)}{TPR_{20,10}(measured)} \right| \tag{4.1}$$

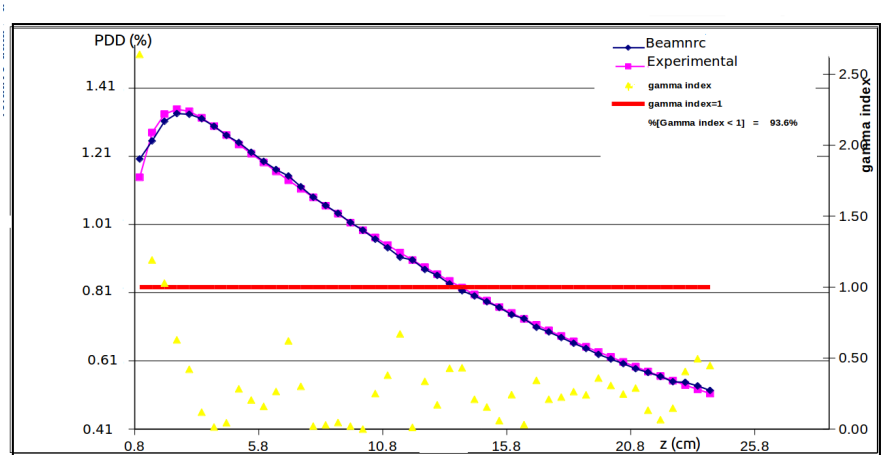

FIGURE 4.17: PDD normalized at depth 10 cm on a field size of 10×10 cm^2 and gamma index for 11.4 MeV.

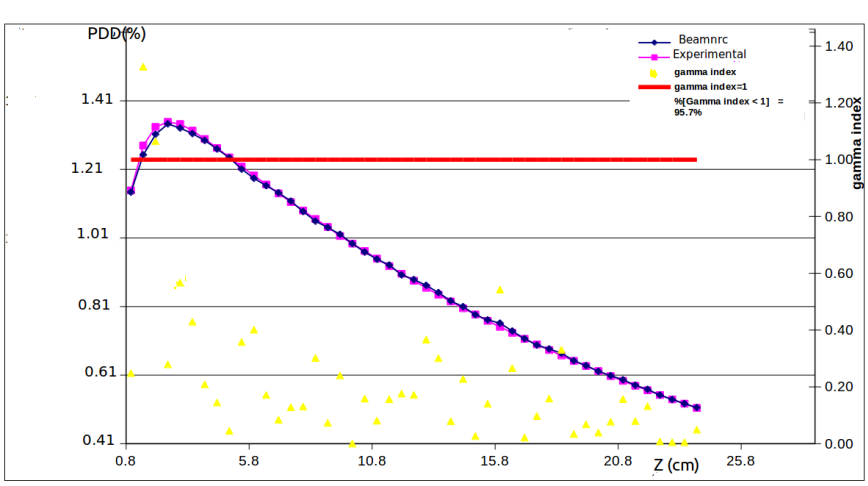

FIGURE 4.18: PDD normalized at depth 10 cm on a field size of 10×10 cm^2 and gamma index for 11.6 MeV.

Table 4.3 summarizes the different comparison tests: the gamma index for the PDD and the DP as well as the $TPR_{20,10}$ and the estimated Z_{Dmax} depths.

From Figures 4.17, 18, 19, 20, 21, 21 and 22 and from results in table 4.3, we can make the following comments:

¶ The influence of the energy of electron beam on the variation of the PDD and $TPR_{20,10}$ is obviously shown. Similarly, some authors sign the DP is also influenced by the incident energy of the beam. We find that when the energy 11.8 MeV, the DP at 10 cm in the water, agree well with experimental (for gamma index less than 1 is equal 91.8%). We also note that the depth of the maximum dose changes slightly with the energy of the incident electrons.

¶ It is noted that for energy 11.8 MeV, the values of Z_{Dmax} and $TPR_{20,10}$ of our simulations agree well with experimental measurements. We eliminate the 11.4 and 11.6 MeV energies. The energies of 12 and 12.2 MeV are also to be eliminated, because at theses energies 11.4 and 11.6 MeV, we find a good result for the Z_{Dmax}

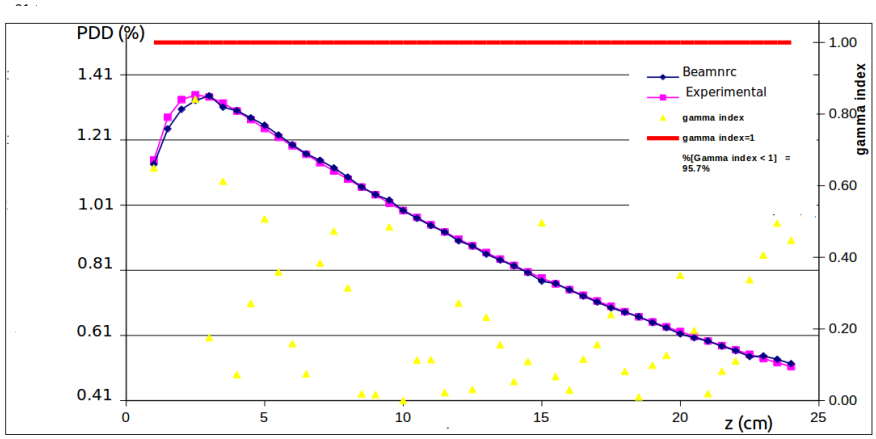

FIGURE 4.19: PDD normalized at depth 10 cm on a field size of 10 × 10 cm^2 and gamma index for 11.8 MeV.

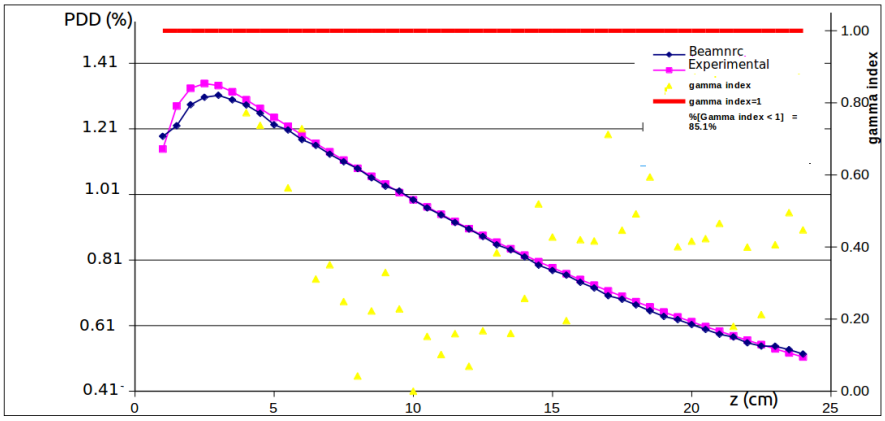

FIGURE 4.20: PDD normalized at depth 10 cm on a field size of 10 × 10 cm^2 and gamma index for 12 MeV.

value with energies, although the DP and the $TPR_{20,10}$ are not well reproduced. For energies 12 and 12.2, the PDD have a good agreement with experimental data but the DP, $TPR_{20,10}$ and Z_{Dmax} didn't. The first results make it possible to eliminate the energies 11.4, 11.6, 12 and 12.2 MeV but it is not sufficient for the rigid determination of the incident electron beam energy.

¶ A comparison of the depth of maximum dose and the $TPR_{20,10}$ don't make it possible to highlight the appropriate energy to define the characteristics of the beam. The conclusion about the energy of the beam is based on the best PDD calculated leading to a gamma index less than 1%.

¶ For the PDD, we found that energy 11.8 MeV give a better percentage of gamma index 95.7%.

¶ Finally, these observations led to consider an optimal energy of the incident electrons beam for 11.8 MeV, because, in this energy, we obtain a better compromise between the three comparison quantities criteria: high percentage of the gamma index, $TPR_{20,10}$, and depth of the maximum dose of the simulation are close to the reference values.

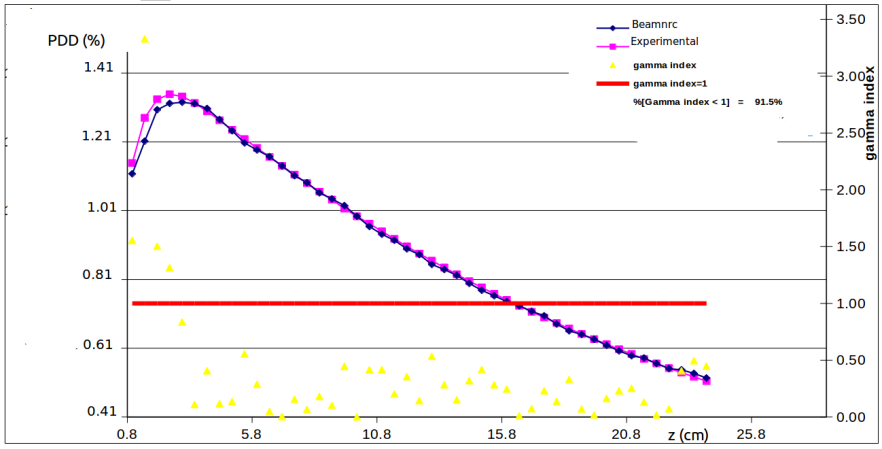

FIGURE 4.21: PDD normalized at depth 10 cm on a field size of 10×10 cm^2 and gamma index for 12.2 MeV.

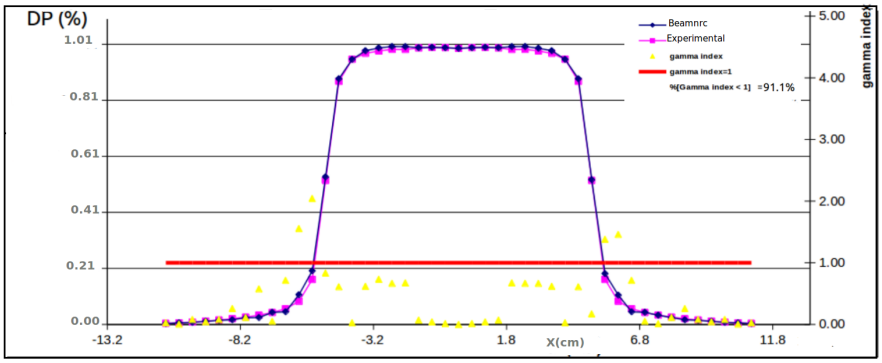

FIGURE 4.22: DP normalized on beam axis at the depth 10 cm on a field size of 10×10 cm^2 and gamma index for 11.8 MeV.

4.3.3.3 Determination of the energy distribution of the initial electrons

The influence of the primary electron source size on the DP was evaluated for all the beams studied, namely the 12 MV photon beams of the SATURNE 43 accelerator.

Mazurier and Blazy [130, 131], showed that the mean energy of initial electrons for the photon mode beam of 12 MV, was very close to energy of 12 MeV announced by the manufacturer. They found that the best agreement between the measured and calculated values is obtained for the Gaussian beam with FWHM of 450 keV. Sheikh Bagheri et al [119] have shown that the electronic equilibrium zone is sensitive to the energy distribution of the primary electron spectrum.

The hypothesis of energy distribution of the incident electrons is issued from that, a dispersion, generally Gaussian of the energy of accelerated particles in the accelerating part of the liac produced by the statistical fluctuations of the magnetic and electric fields at the level of the deflection coils.

When we minimize the range of energy that may contain the appropriate value, we proceeded to find the best agreement between the calculation and experiment results by introducing Gaussian distributions of different values of FWHM for mean energy in the previous study 11.8 MeV.

Figures 4.23, 24, 25, 26, 27, 28, 29 and 30 represent our DP results obtained in the

TABLE 4.3: Comparison of gamma index tests for calculated PDD and DP for mono-energetic electron beams.

	Mean energy of incident electrons beam (MeV)	11.4	11.6	11.8	12	12.2
Gamma index <1%	PDD	93.6%	95.7%	95.7%	85.1%	91.5%
	DP	64.4%	75.6%	91.1%	64.4%	64.4%
$TPR_{20,10}$	0.6282 (experiment)	0.6220	0.6198	0.6275	0.6211	0.6249
$\Delta(TPR_{20,10})$		0.98%	1.33%	0.11%	1.13%	0.52%
$\mathbf{Z}_{max}$**(cm)**	2.5 (experiment)	2.5	2.5	2.5	3	3

simulations with different values of FWHM for the Gaussian energy distribution from 0.05 cm to 0.19 cm by step 0.02 cm with energy 11.8 MeV. We have chosen to present the results in these figures, in order to study the evolution of the dose distributions with the variation of FWHM for the mean energy 11.8 MeV by using the index gamma < 1% and choose the best value of FWHM for DP which agree well with experiment DP result.

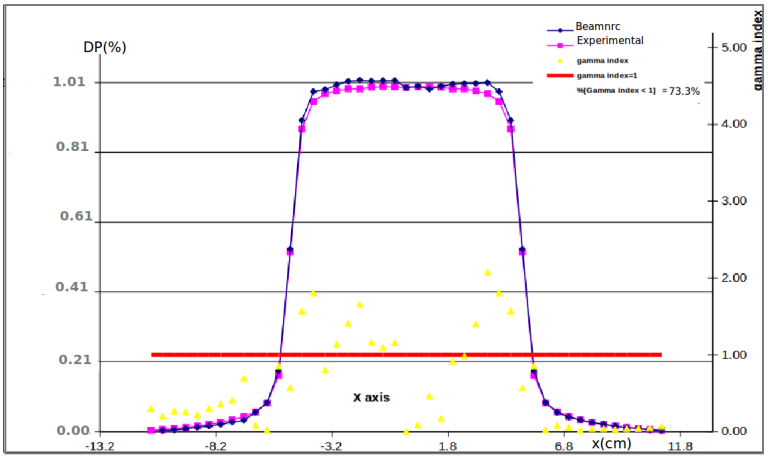

FIGURE 4.23: DP normalized on beam axis at the depth 10 cm for FWHM = 0.19 cm and mean energy 11.8 MeV.

Firsts remarks from theses previous figures show that the DP vary significantly with the FWHM. From Figures 4.24, we note that the gamma index <1% is equal to 91.1% that establish the DP calculated with BEAMnrc agree well with the DP measured in LNHB for energy 11.8 MeV and FWHM equal to 0.17 cm. From the previous criterion we conclude that for future work with BEAMnrc code in modeling the SATURNE 43 linac, we work for all our simulations with the energy 11.8 MeV and FWHM with 0.17 cm.

4.3.3.4 Sensitivity to field size on the dose distributions

Asghar Mesbahi [133] studied the effect of irradiation field size on PDD and DP.

In this study, we adopted three configurations of the jaw pairs to define the three square field size $2 \times 2\ cm^2$, $10 \times 10\ cm^2$ and $20 \times 20\ cm^2$, respectively. PHSP are

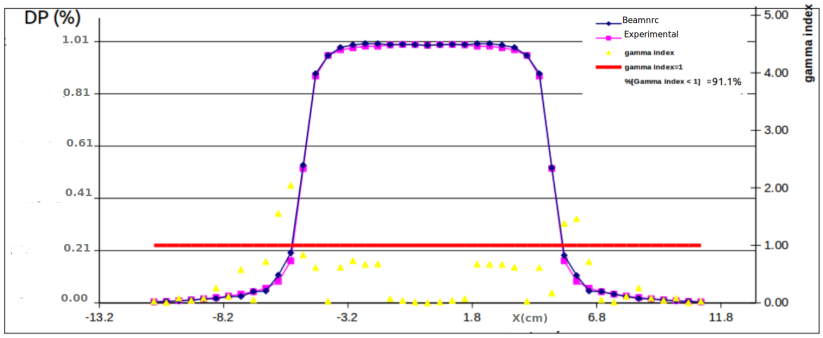

FIGURE 4.24: DP normalized on beam axis at the depth 10 cm for FWHM = 0.17 cm and mean energy 11.8 MeV.

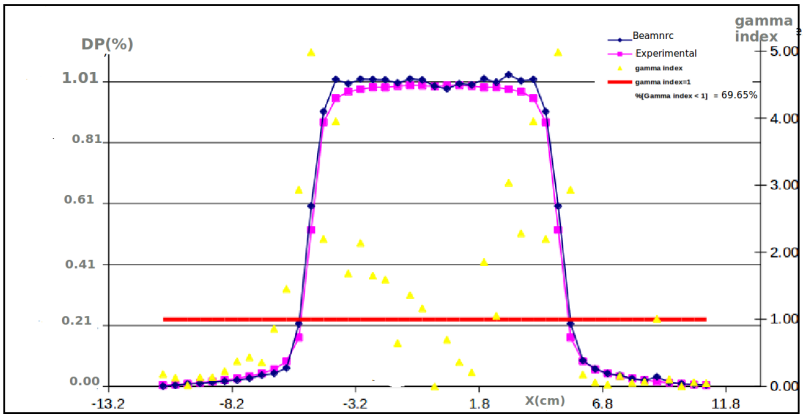

FIGURE 4.25: DP normalized on beam axis at the depth 10 cm for FWHM = 0.15 cm and mean energy 11.8 MeV.

scored for different numbers histories simulated in order to have approximately the same size of PHSP file (the size of PHSP file increases with the field size). We simulated enough histories for the absorbed dose calculations to obtain a relative statistical error less than 1%. Figures 4.31 and 32 illustrate the results obtained for the PDD and the DP for the three fields size studied.

We remark in figures 4.32 and 33 that, the dose increases with the field size. Indeed, for the large field, the scattered photons augment in the beam irradiation. So, large fields allow irradiation of phantom with high energy photons.
Similarly, we remark that the surface dose increases with the field size. This increase is due to the secondary electron contamination created in the materials of the head's components, in the air, and phantom surface for large field size.

4.3.4 Conclusion

In this chapter, we have proposed a new methodology to adjust the parameters of the 12 MV photon beam produced by the accelerator SATURNE 43, through the comparison of the PDD and DP and measurements made by LNHB in France on a homogeneous water phantom. Our simulation results showed that all beam parameters, mean energy and FWHM of the energy and spatial distributions...etc, have a significant effect on the PDD and DP. Our study on the initial parameters of

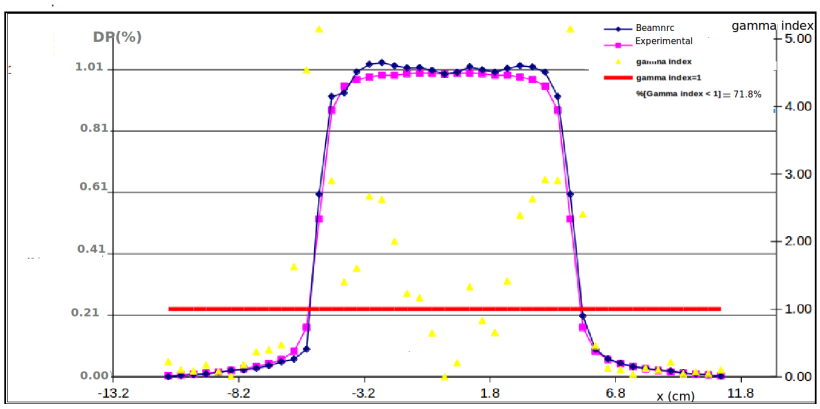

FIGURE 4.26: DP normalized on beam axis at the depth 10 cm for FWHM = 0.13 cm and mean energy 11.8 MeV.

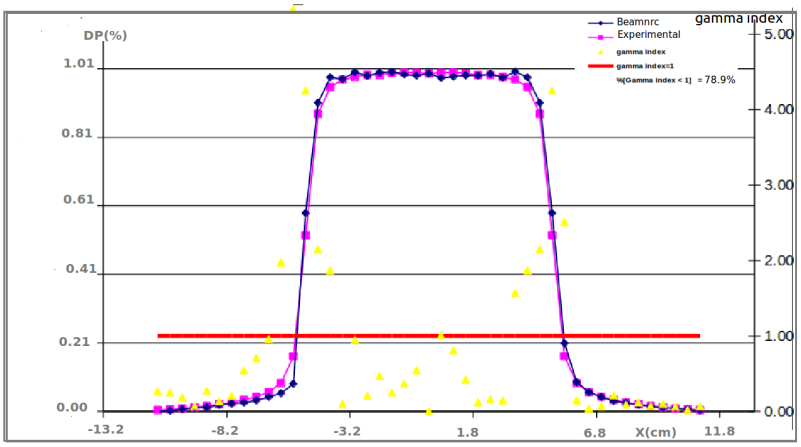

FIGURE 4.27: DP normalized on beam axis at the depth 10 cm for FWHM = 0.11 cm and mean energy 11.8 MeV.

SATURNE 43 accelerator has led to the conclusion that the 12 MV photons of this accelerator originate from the bremsstrahlung of a Gaussian energy distribution of electron beam with a energy of 11.8 MeV and a focal spot size that can be described by a Gaussian spatial distribution perfectly symmetrical around the beam axis of the geometry and having a FWHM value of 0.17 cm.

An analysis of the effects of certain components of the accelerator head as FF component on the shape of the photon spectrum and dose distributions was conducted. This simulation highlighted the potential of Monte Carlo computation to correctly reproduce dose distributions produced experimentally.

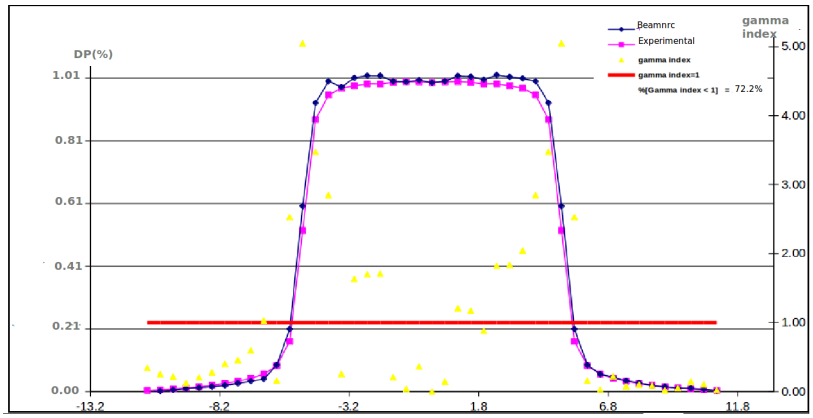

FIGURE 4.28: DP normalized on beam axis at the depth 10 cm for FWHM = 0.09 cm and mean energy 11.8 MeV.

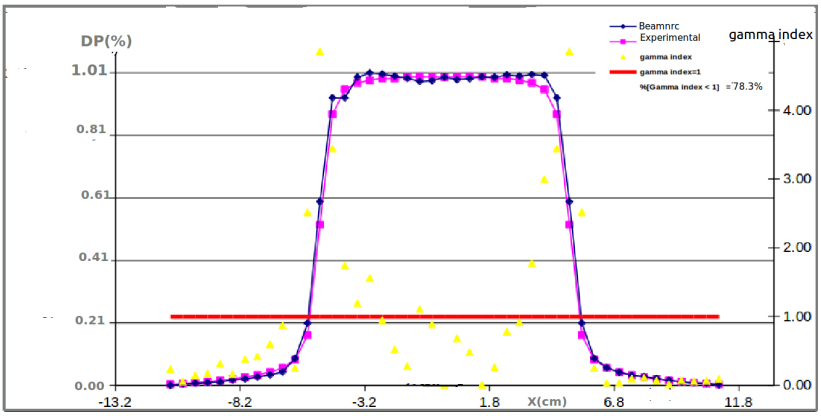

FIGURE 4.29: DP normalized on beam axis at the depth 10 cm for FWHM = 0.07 cm and mean energy 11.8 MeV.

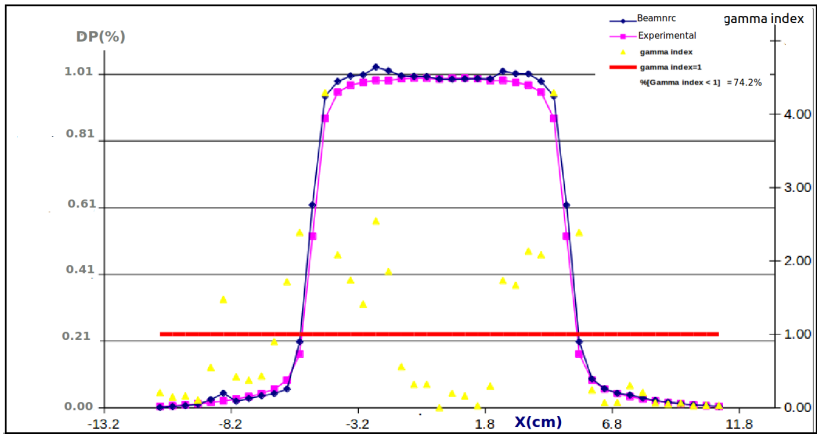

FIGURE 4.30: DP normalized on beam axis at the depth 10 cm for FWHM = 0.05 cm and mean energy 11.8 MeV.

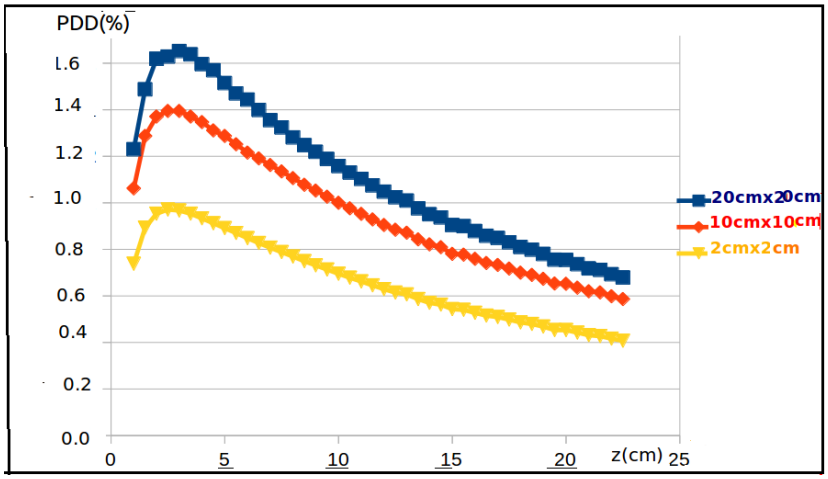

FIGURE 4.31: Variations of PDD with the field size on a cubic water phantom. The PDD was normalized at the depth 10 cm on the field size $10 \times 10\ cm^2$

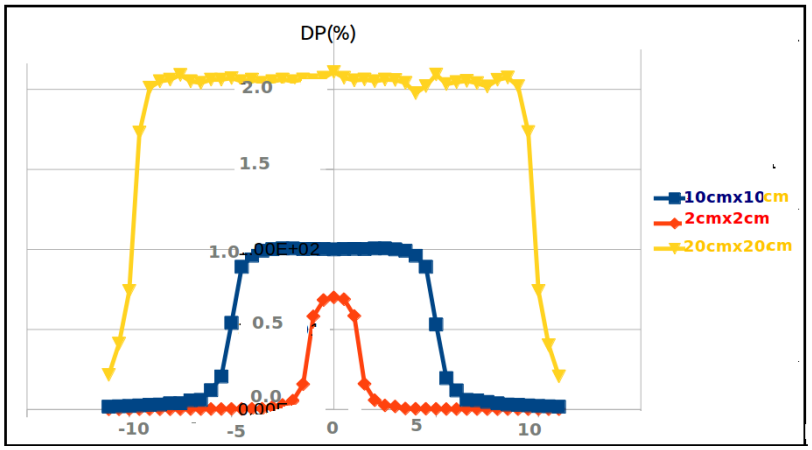

FIGURE 4.32: Variations of DP with the field size. The DP was normalised on beam axis at the depth 10 cm on $10 \times 10\ cm^2$ field size

Chapter 5

Efficiency and Dosimetric Properties of SATURNE 43

5.1 Efficiency optimization for 12 MV photon beam

5.1.1 Introduction

The MC technique is, by its nature, has a disadvantage to their application in the field of radiotherapy because it needs more time to finish the calculation. That made MC methods prohibitive for routine clinical use. The computation time depends on many parameters as the number of particles generated, their types, their energies and the material in which they are transported. So to get good statistics it is required to simulate thousands or hundreds of millions of particles. In the last years, there have been rapid developments in computer technology that lead to exponential increase in processor speed, as well as improvements in software optimization and networking technology and have made MC technique treatment planning a feasible choice [133,134]. A number of MC codes are now in clinical use, such as BEAMnrc; VMC++ [135]; PENELOPE [136,137]; GEANT4 [138]; and MCNPX [139].

The development of advanced computers for parallel calculations is becoming increasingly accessible to medical physicists. However, for various medical physic applications is not enough, because CPU is still large.

The uncertainty of the dose computation procedures for external photon beams radiotherapy obtained with MC code is mainly given by the approximations used. This uncertainty can be reduced by introducing more precise physical models. But that require more calculation times. In the literature, there are different techniques to reduce the statistical fluctuations of MC calculations without increasing the number of particle simulated. These techniques are known as VRTs [86].

In the simulation of photon beams inside a head of medical linac, a VRT that is often used involves "splitting" bremsstrahlung interactions [141][. Bremsstrahlung splitting can importantly reduce the uncertainty in all photon quantities calculated (e.g., dose due to photons, photon fluence, photon energy spectrum) at the bottom of the accelerator for a given number of electrons incident striking the target. The decrease in uncertainty is greater than the increase in CPU time/history required by bremsstrahlung splitting simulation.

The BEAMnrc offers several VRTs and AEITs [86]. The DBS technique speeds up the BEAMnrc treatment head simulations and considered as the most published investigations VRT in the recent literature [86,141]. In this project, we applied these techniques in the head of SATURNE 43 linac simulation in order to determine the

computing time gain, reduce uncertainties and improve the statistical results. We investigated the influence of different photon and bremsstrahlung cross-section data available in BEAMnrc user code on the precise calculated fluence and computed dose distributions on 12 MV SATURNE 43 head's linac.

Firstly, we run the simulation without any VRTs (the analogue simulation) and secondly we do the simulation in parallel processing in computer with VRTs. In the third step, we combined the VRTs and AEITs with parallel processing computer and compare the efficiency gain. DOSXYZnrc [72], an EGSnrc MC user code, was used to calculate dose distributions in a water phantom, which were compared with measured data. This was performed to validate the accuracy of dose distribution calculated with the various VRTs parameters.

5.1.2 Materials and methods

5.1.2.1 Modeling of SATURNE 43 head's

Specifying the geometry of the head's linac is an important step, upon which the accuracy of the simulation is largely based. It requires the specific geometry of each component of the system to be modeled accurately, like as: materials, dimensions in (x, y, z) directions, and the position of each component inside the system. In most cases, such information can be obtained from the manufacturer. More than 20 precoded components defined as component modules (CMs) were implemented in BEAMnrc code to facilitate the modeling linac components with a high degree of precise. We modeled a head linac of 12 MV SATURNE 43 with the BEAMnrc MC code.

Beams simulated for this study was a 12 MV photon beam from a SATURNE 43 accelerator with a $10 \times 10\ cm^2$ field at SSD = 100 cm. The aperture of treatment fields is defined by using a pair of jaws.

All BEAMnrc parameter simulations have been used as ECUT = 0.521 and 0.700 MeV, PCUT = 0.01 MeV, and use range rejection with varying ECUTRR everywhere except the target, with ESAVE = 0, 1, 2, and 3 MeV for the 12 MV beam. No range rejection is done in the target. Such parameters settings have been shown to provide the best compromise between simulation speed and accuracy. All simulations are carried out using the latest version of BEAMnrc. DBS splitting number (NBRSPL) is set to 500 for our simulation of 12 MV SATURNE 43 linac.

These splitting numbers have been shown to maximize the dose and fluence efficiency at these beam energies [71]. We used BCSE Factor of 2 and 20. The initial histories were 3×10^9 particles for analogue simulation and 6×10^6 particles for VRTs simulation.

Simulations using the BEAMnrc and DOSXYZnrc codes were run on a desktop core i7 CPU with 8 GHz RAM on Ubuntu 14.04 system.

The photon energy spectra were obtained by using the BEAMDP (BEAM Data Processor) user code analyzing the scored PHSP file generated by the BEAMnrc user code at the depth z = 50 cm on the bottom jaws for square field size $10 \times 10\ cm^2$ using 100 energy bins, and graphs were plotted with the 2D graph plotting software QT-GRACE.

5.1.2.2 Phase space plan scoring

A PHSP plan is a space in which all possible states of a system are registered, and each state of the system is a single point in space. It defined the scored particles with their characteristic states, which including: their energy, their type (photon, electron, positron), their position, their direction of propagation, and their statistical weight [71]. The collection is done by a surface placed at bottom of the accelerator, which records the particles that cross it. The information collected is written in a digital file whose size depends on the number of simulated particles. The file can then be used by another simulation in which the recorded particles serve as source particles. It is therefore possible to split a simulation into several. In the case of the simulation of a photon beam for a fixed nominal energy, only the geometric description of the secondary collimation (X and Y jaws) and the presence of accessories in the beam (filter, cache-holder, caches, boluses, etc.) vary from one irradiation to another. By using a PHSP, the calculations of the transport of the electrons and photons will be realized only once.

In practice, the modeling of the photon beam by the PHSP consists of two stages:

¶ First step: Create a PHSP plan: A PHSP plan will be placed at the bottom of the linac at the end of the simulation, that a PHSP file will be written and available for reading by another simulation.

¶ Second step: Use the PHSP file that was previously obtained, it can be used as many times as necessary for needed simulation.

Our PHSP files were scored at the z = 50 cm below the pair jaws of linac for every simulation.

5.1.2.3 Computing efficiency

The efficiency (ϵ) of an MC simulation is defined as [71]:

$$\epsilon = \frac{1}{T.s^2} \tag{5.1}$$

Where s is an estimate of the uncertainty of the quantity of interest (e.g., fluence or dose) and T(min) is the total CPU time for the simulation. As s proportional to 1/N and T proportional to N (number of histories used in simulation), therefore the efficiency is independent of N used to determine it. The efficiency comparisons only make sense for the same situation and parameter simulation on the same hardware. The technique that improves the efficiency without introducing significant noise to the result, by changing the s^2 for given N, is VRT. This is not to be confused with such efficiency enhancement methods where the improved efficiency is achieved by implementing different approximations into radiation transport calculations.

5.1.2.4 Variance reduction techniques

The name " variance reduction " can be justified as follows: When comparing two distinct MC procedures used to estimate the same quantity, it is convenient to assign efficiency to each one. Intuitively, this efficiency should increase, for example, as the amount of time (computing time) required for each trial decreases and also should increase as the variance associated with the estimate decreases (all MC estimates

have an inherent sampling variance). VRTs improve the efficiency without changing the physics [71,86,143].

When VRTs are implemented correctly, they are given the same result as without using these VRTs. Examples of VRTs: forcing photon interactions; bremsstrahlung splitting; Russian Roulette; photon splitting; and bremsstrahlung cross section enhancement [71].

♣ **Directional Bremsstrahlung Splitting**

DBS technique began from the philosophy in which bremsstrahlung photons aimed into an field size of interest (encompassing the treatment field size) are split at the moment of their creation, while those aimed away from the field size of interest are not considered. So the main concept behind the bremsstrahlung (brem) splitting technique was to increase the number of photon beams in the field size of interest in order coincidence to reduce the uncertainty value and achieve the simulation within a minimum time. With the splitting technique, we can save the time required for complete simulation by splitting brem photons produced by some electrons into many photons. This splitting technique can be made choosing one of the three different techniques implemented in BEAMnrc code UBS (uniform bremsstrahlung splitting), SBS (selective bremsstrahlung splitting), or DBS [71,86,142]. Comparison of these techniques has established that DBS, to be the efficient technique at low and high energies [71,86].

In order to utilize the DBS technique for photon splitting, three main parameters should be provided by the user: the splitting number (NBRSPL), the radius of the FS of splitting, i.e., the field size of interest, and the source to surface distance (SSD) at the field size. The investigation of this technique means that the majority of the simulation time is spent on tracking the particles that contribute to the quantity of interest, and avoids wasting time in simulating the other particles. So the splitting technique saves the time required to simulate a large number of electrons to obtain many photons. We used the following parameter for DBS simulation as follows: The DBS NBRSPL was set to 500, the radius of field size was 7, 10, and 13 cm, and SSD was equal to 100 cm.

DBS uses a combination of interaction splitting for bremsstrahlung, annihilation, Compton scattering, pair production, and photo-absorption to achieve an optimal efficiency of photon beam simulations.

♣ **Photon and Bremsstrahlung cross sections**

We used the different photon cross sections: -Storm-Israel (PEGS4), which is the standard PEGS4 cross sections and the default photon cross section; -EPDL, which uses the cross sections from the evaluated photon data library (EPDL) from Lawrence Livermore National Laboratory; and -XCOM, which used XCOM photon cross sections from Berger and Hubbell [71]. Also, we investigated the differential cross section for the bremsstrahlung interactions implemented in BEAMnrc which is Bethe-Heitler (BH), NIST, and NRC [71,88]. In the megavoltage energy range, the BH cross section is obtained from the first Born approximation with an empirical correction factor. In the range of 2 and 50 MeV, the NIST cross section uses the cubic spline interpolations.

PHSP files were generated for the different photon cross sections, keeping all

other parameters with their default values with VRTs. When changing bremsstrahlung differential cross section from BH to NIST and NRC, default photon cross section was used, i.e. PEGS4.

♣ **Bremsstrahlung Cross Section Enhancement**

BCSE is implemented into BEAMnrc in 2007 to gain and improve the efficiency of simulations that involve the production of x-ray from bremsstrahlung thin targets in the x-ray tubes and clinical linac [71, 87, 88]. BCSE could be used in combination with all VRTs (e.g., range rejection, DBS...etc) already implemented in BEAMnrc MC code [88]. An important efficiency gain are completely obtained when the BCSE is optimally combined with DBS. For typical simulations of interest in medical physics, the efficiency gains can be up to five orders of those obtained with such analogue simulations. For our simulation, we used BCSE Factor of 2 and 20 as recommended in some literatures [71].

5.1.2.5 Approximate efficiency improving techniques

♣ **Charged particle range rejection**

Range rejection is a VRT which terminates a charged particle history (depositing all of its energy at that point) if its remaining energy is not sufficient to leave the current region.

Range rejection is used to save computing time during simulations [71,143]. The basic method is to calculate the range of a charged particle and terminate its history. Range rejection technique introduces an approximation because, in terminating a charged particle's history and depositing all of its energy in the current region, it is assumed that any bremsstrahlung photons that would have been created by the charge particle, do not leave the current region or reach the scoring plane at the bottom of the accelerator. The effect of this approximation is minimized by ESAVE allowing charged particles with insufficient energy to leave the region to still be able to create bremsstrahlung photons exiting the region.

The appropriate selection of ESAVE is dependent on the situation. It has been shown that with ESAVE = 2 MeV only 0.1% of photons attaining the phantom surface is ignored (Rogers et al., 2013) [71]. In our simulation we used the following parameter as ECUT = 0.521 and 0.700 MeV, PCUT = 0.01 MeV, and using the range rejection with varying ECUTRR everywhere except the target, with ESAVE = 0, 1, 2, and 3 MeV for the 12 MV beam.

♣ **Boundary Crossing Algorithm (BCA)**

The boundary crossing algorithm together with the electron transport algorithm constitutes the condensed history technique used by a particular MC code system. In BEAMnrc, we have the choice of two different BCA: PRESTA-I and EXACT, where the latter is the default option [72,142]. We investigated the differences between the PRESTA-I and EXACT BCA implementation in the calculated spectral fluence and energy distribution.

5.1.3 Results and discussion

The uncertainty s was estimated on the photon fluence at scoring plan below the lower jaws and absorbed dose at 10 cm. Our results are summarized in the following tables.

Two options (DBS and UBS) were compared when we have simulated 6×10^6 histories. It has been applied with other techniques as (rang rejection, enhancement cross section and splitting of photon and electron). Table 5.1 contains a summary of the results obtained in our simulation. Normally, the uses of those techniques in conjunction with others are useful to enhance the efficiency of simulation.

From table 5.1, it is clear that, the simulation efficiency for the UBS with RR has increased by 3800 times in comparison to analogue simulation. We note that, UBS technique split the higher order bremsstrahlung photons and annihilation events that have the splitting number equal to use for primary bremsstrahlung events. Consequently, there is a CPU time consuming to follow up the particles.

Splitting of electron or positron $ICM\_SPLIT(e^-/e^+)$ parameter has been tested without other techniques. It is clear in table 5.1, that the efficiency of simulation was improved about 140 times compared to analogue simulation and about 3800 times for UBS with RR. In $ICM\_SPLIT(e^-/e^+)$, the splitting component and the splitting number of electron and positrons must be determined.

The BCSE efficiency was improved about 3900 times comparing with analogue simulation. The DBS efficiency was improved about 5200 times comparing with analogue simulation and 1.5 times UBS with RR. And 35 times $ICM\_SPLIT(e^-/e^+)$.

TABLE 5.1: Photon fluence efficiency for VRTs and AEIT simulation for 12 MV photon beam.

VRTs and AEIT	**S(%)**	**T(s)**	ϵ
Analogue(3×10^9 histories)	6.5	623764.2	0.02
Splitting of e^-/e^+	1.9	936.2	2.95
BCSE	0.2	3156.1	79.21
Bremsstrahlung splitting:			
+Uniform(NBS=200) with RR	0.2	3226.7	77.48
+Directional(NBS=500)	0.2	2367.2	105.61

Table 5.2 shows the efficiency of photon fluence for the boundary crossing algorithm PRESTA-I and EXACT. We have seen that the efficiency was higher for PRESTA-I by a factor 1.12 in comparison to BCA_EXACT.

Table 5.3 shows the efficiency of photon fluence as a function of the radius of the FS of splitting for the 12 MV beam with a square FS of $10 \times 10\ cm^2$. We have seen that the efficiency for R = 7 cm has higher value in comparison to the value of radius of 10 and 13 cm.

The efficiency of DBS in the broad radius is significantly lower with photon fluence efficiency inside the field which decreases by a factor of 1.05.

In this study, we tested the different photon and bremsstrahlung cross sections, and we compared its influences in the efficiency. We found that the efficiency for different photon cross sections; PEGS4, epdl, and xcom implemented in BEAMnrc

TABLE 5.2: Photon fluence efficiency for BCA_EXACT and $BCA\_PRESTA-I$ with DBS simulation for 12 MV photon beam on a $10 \times 10\ cm^2$ FS.

	S(%)	**T(s)**	ϵ
BCA_EXACT	0.2	2367.2	105.61
BCA_PRESTA-I	0.2	2111.5	118.40

TABLE 5.3: Comparison of photon fluence efficiency with the radius of the field size of splitting for 12 MV photon beam on a $10 \times 10\ cm^2$ square field size.

Radius	**S(%)**	**T(s)**	ϵ
R = 7 cm	0.2	2302.7	108.57
R = 10 cm	0.2	2367.2	105.61
R = 13 cm	0.2	2426.7	103.02

code have the same value in the efficiency as indicated in table 5.4 with a slight different.

Bremsstrahlung Photon Splitting is a technique that has a significantly contribute to enhance the statistics of bremsstrahlung photons generated by interaction the electrons with matter.

TABLE 5.4: Photon fluence efficiency for different photon cross sections for 12 MV photon beam on a $10 \times 10\ cm^2$ field size.

Simulation type	**S(%)**	**T(s)**	ϵ
PEGS4	0.2	2364.1	105.74
EPDL	0.2	2356.3	106.09
XCOM	0.2	2367.2	105.61

We have obtained an equal value for the efficiency with different bremsstrahlung cross sections BH, and NRC but for the NIST bremsstrahlung cross sections, we have seen a light less value see the table 5.5.

In table 5.6, we calculate the efficiency for different value of ESAVE in two case 521 KeV and 700 KeV. We have shown that the photon fluence efficiency for the case 521 KeV from the value of ESAVE = off to ESAVE = 3 MeV was increased by a factor about 3.7. For the case 700 KeV the efficiency was increased by a factor about 4 when we change the value of ESAVE = off to the value ESAVE = 3 MeV.

We conclude that DBS, BCSE, ICM_SPLIT, and UBS improve the efficiency of simulations when the techniques have been applied individually.

From table 5.7 we calculate the efficiency for the dose at the depth of 10 cm. We have seen that the efficiency for DBS (VRTs + AEITs + parallel) was increased about 19000 times and about 4300 times when DBS(VRTs + AEITs + without parallel) in comparison to analogue simulation.

TABLE 5.5: Photon fluence efficiency for different Bremsstrahlung cross sections for 12 MV photon beam on a $10 \times 10\ cm^2$ field size.

Simulation type	**S(%)**	**T(s)**	ϵ
BH	0.2	2367.2	105.61
NIST	0.2	2485.3	100.59
NRC	0.2	2360.9	105.89

TABLE 5.6: Comparison of photon fluence efficiency with different values of ESAVE for 12 MV photon beam.

Case	**PCUT(MeV)**	**ECUT(MeV)**	**ESAVE(MeV)**	**T(s)**	**S(%)**	ϵ
1	0.01	0.700	0	1159.5	0.2	215.61
2	0.01	0.700	1	315.5	0.2	792.39
3	0.01	0.700	2	288.1	0.2	867.75
4	0.01	0.700	3	208.6	0.2	906.21
5	0.01	0.521	0	2367.2	0.2	105.61
6	0.01	0.521	1	739.7	0.2	337.97
7	0.01	0.521	2	646.8	0.2	386.51
8	0.01	0.521	3	630.1	0.2	396.76

Mohammed et al. [143] found a rising of efficiency by 1130 time compared with analogue simulation. Zoubair et al. [138] found a rising of efficiency for accelerated simulation by 737 times compared with analogue simulation.

Fragoso et al. [145] found the highest relative efficiencies were 935 times compared to simulation without VRTs on a single 2.6 GHz processor. Kawrakow [146] found that a DBS simulation would be roughly 10,000 times more efficient than a simulation without VRT. Kawrakow et al. [86] found that the efficiency with DBS in a central axis depth dose curve was improved by a factor of 6.4 over SBS and by a factor of 20 over UBS for 6 MV of $10 \times 10\ cm^2$ field size.

Figure 5.1 delineates the comparison of the PDD curves for experimental, VRT combined, and analogue simulation results. The absolute dose value at the depth of 10 cm on the water phantom was 3.190E-16 and 3.143E-16 Gy for analogue and VRTs simulation, respectively (see table 5.7).

From Figure 5.1, we note that the representative data obtained with analogue simulation suffers from irregularities in the relative dose distribution, in contrast, the PDD curve obtained with VRTs combined is characterized by uniformity with experimental PDD.

Figure 5.2 delineates the comparison of PDD curves for VRTs combined, and analogue simulation.

The gamma index analysis performed for PDD curves for VRTs and analogue simulation at the central beam axis shows that about 90 % points are passing the test for 1%/1 mm. It is seen that from figure 5.2, the VRTs techniques give the same results as with obtained with analogue simulation except for a few points in the buildup region.

TABLE 5.7: Comparing between MCNPX and BEAMnrc dose efficiency at the depth of 10 cm for 12 MV photon beam on a $10 \times 10\ cm^2$ FS.

Simulation type	**N of histories**	**T(min)**	**Absorbed dose at 10 cm (Gy)**	**S(%)**	ϵ
Analogue	3×10^9	10396.0	3.190E-16	6.5	0.023
MCNPX (Meriem et al.)	15×10^8	58226.4	3.59E-16	4.3	0.009
DBS(with VRTs and AEITs) +without Parallel	6×10^6	220.6	3.143E-16	0.6	98.029
DBS(with VRTs and AEITs)+Parallel	6×10^6	50.1	3.143E-16	0.6	431.060

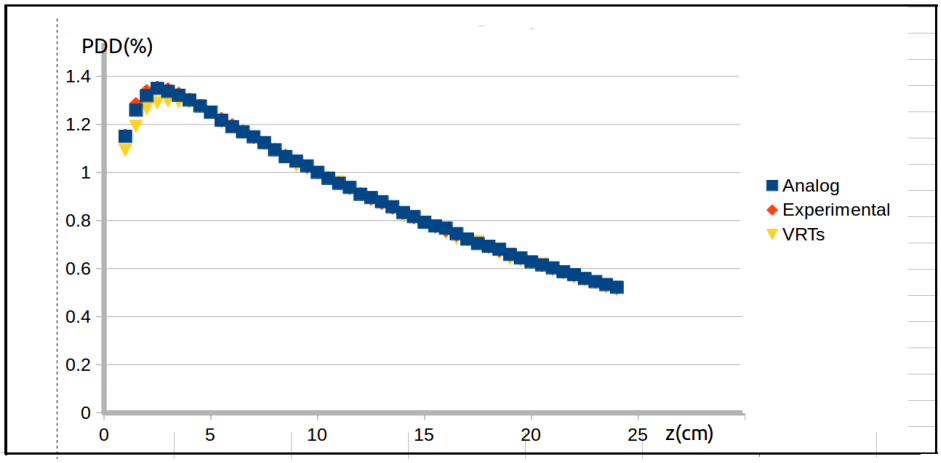

FIGURE 5.1: A Comparison of VRTs, Experimental, and analogue PDD normalized at the depth of 10 cm on a water phantom with the field size of $10 \times 10\ cm^2$ for 12 MV beam.

5.1.4 Conclusion

This work investigates the efficiency of photon beam dose and fluence calculations with BEAMnrc for SATURNE 43 linac. The main result of this work is to show that, when employed VRTs parameters combined in BEAMnrc, the difference in the efficiency between simulations using VRTs parameters combined in parallel and analogue simulation becomes more important. Employing VRTs combined on a parallel simulation with BEAMnrc code improves the photon beam dose calculation efficiency about 19000 times in comparison to analogue simulation. In addition, we have demonstrated that DBS offers a significant improvement in photon fluence efficiency in comparison to BCSE, ICM_SPLIT(e-/e+), and UBS, respectively. DBS increases the photon fluence efficiency about 5200 times compared to the analogue simulation.

We have partly demonstrated that our results showed a higher photon beam dose calculation efficiency with BEAMnrc than MCNPX code in case of analogue simulation (without VRTs).

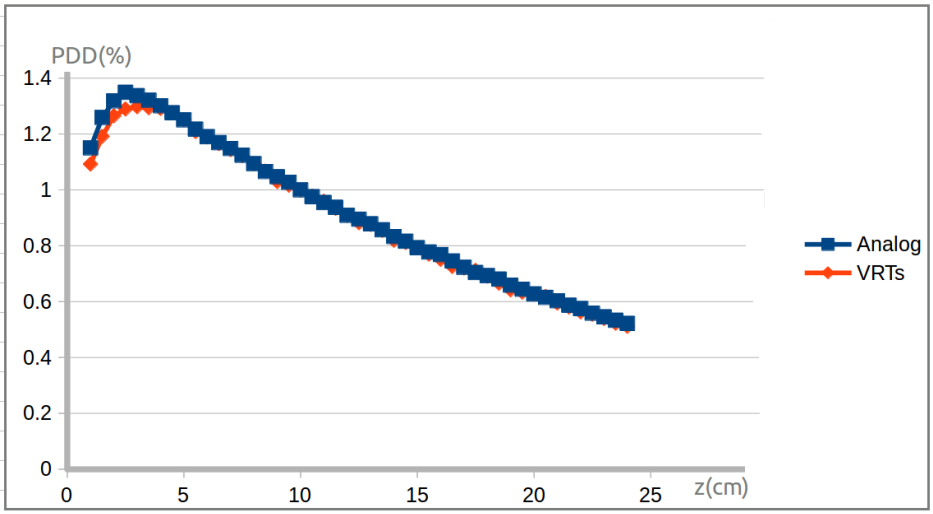

FIGURE 5.2: A Comparison of VRTs and analog PDD normalized at the depth of 10 cm by using the gamma index method on a water phantom with the field size of $10 \times 10\ cm^2$ for 12 MV beam.

The major advantage of using aggressive VRTs combined in parallel simulation is the significant improvement gain in calculation time without a compromise in the accuracy of the patient dose computation. This is essential if one is considering real time MC simulation of the treatment head and patient.

5.2 Free flattening filter beam and dose distribution

5.2.1 Introduction

The cancer treatment will continue to be one of the greatest health challenges of the 21st century. One of the most important and commonly treatment techniques used is radiotherapy using the medical linac. In this linac, the angular distribution of the bremsstrahlung photons is modified by the component of FF. The latter is designed to generate a uniform lateral dose distribution inside a water phantom at the depth of z = 10 cm. In the most clinical linac, the materials which formed the flattening filters are aluminum, Iron, copper, tungsten, or a mixture of these components, that are all characterized by a high Z material. What is more, these materials are specific to each particular beam energy. Generally, neither tumours nor patients are flat; therefore, it is necessary to use the FFF beams which can have more benefits than utilizing conventional filtered beams due to the non-uniform intensity across the field size.

A multiple FFF medical linacs (Varian True Beam, Siemens...etc.) for multiple energies of 6, 7, 10, 15, and 18 MV are basically a standard linacs with the FFF mode. The multiple FFF commercial medical linacs were simulated for the application of stereotactic radiosurgery and radiotherapy, as well as IMRT [147–152].

Recently, many works have been studying the effect of FFF x-rays in the field of physics especially in the clinical domain. For example, using FFF photon beams for treating lung cancer is feasible. Moreover, it decreases beam-on time by 50%

for both IMRT and Rapid Arc modern technique [153–157] that can be an important benefit for the management of organ mobilization. The treatment planning quality using flat conventional x-ray and FFF mode has been reported to be dosimetrically equivalent. The FFF beams are proposed to be applicable to whole-breast irradiation as well.

Many authors have been reviewing the photon energy spectra, backscattering, and beam steering effects of the FFF beams. It has also been reported that other researchers were able to reduce the neutron production in many previous literatures using FFF photon beam.

According to these benefits and advantages features, the FFF beams can have a major contribution to decrease unwanted exposure and cause the secondary cancers owing to the absence of the dominant component of FF responsible for scattering radiation in the photon beam [154].

Several studies have found by MC simulations that removing the FF component from a head's linac can cause excessive amounts of contaminating electrons to be excited from the primary collimator and target and passed to the patient surface. To reduce these amounts of contaminating electrons, they include a thin metal plate in the same position as the FF in the head of linac, which is necessary to reduce the electron contaminations.

In our linac model, the thin metal plate is substituted for the flattening filter by a thin plate of aluminium (Al) or tungsten (W) in the beam line that we have obtained a replacement flattening filter (FFF) [147, 148, 158]. After entering a plate of Al, a number of electrons have been absorbed and stopped before affecting and entering the patient body [147, 148, 159, 160]. In this work, the head of SATURNE 43 linac is simulated using BEAMnrc and DOSXYZnrc Monte Carlo (MC) codes. Then, we have the effects of FFF mode on the photon energy spectra, PDD, DP, mean energy, and the tissue phantom ratio for the 12 MV unflattened photon beam.

5.2.2 Materials and Methods

5.2.2.1 Monte Carlo modeling of SATURNE 43 linac

The MC modeling of a head's linac is a main step in radiotherapy field. The MC model constructed and verified can have an opportuneness to predict a multitude dosimeters characteristics. However, the detailed created and constructed model of a head's linac is a difficult step due to its complex geometry and it is necessary to have a detailed modelling approach to obtain a discrepancy of the dose-calculation of 2%/2mm or less in the gamma index method. To fulfill this purpose, we used BEAMnrc MC Code to generate and analyze the phase space file registered below the bottom jaws of linac.

In the first step of this MC work, we successfully modeled precisely the head's geometry of SATURNE 43 accordingly to the fabricator's data. In the second step, we modeled the head of SATURNE 43 in FFF mode (the complete head's geometry of Saturne 43 without FF).

The Dose distributions was computed by the DOSXYZnrc MC code on a water phantom using the scored PHSP file obtained from the BEAMnrc code at Z = 50 cm. A cubic water phantom with (x, y, z) dimension of $40 \times 40 \times 40\ cm^3$ was then modeled under the treatment head with the DOSXYZnrc user code. The source

surface distance (SSD) was 90 cm between the target component and the phantom surface. The jaws were set to create a field size of $10 \times 10\ cm^2$, $5 \times 5\ cm^2$, and $2 \times 2\ cm^2$ at the distance of 100 cm from the target component (at the depth of 10 cm inside the water phantom) [128]. The voxels dimension (x,y,z) of the cubic water phantom with the DOSXYZnrc MC code were $5 \times 5 \times 5\ mm^3$ for both depth and profile dose calculations.

The photon and electron low-energy cutoffs parameter used in this simulation were 10 keV, and 521 keV, respectively.

To investigate the following dosimetric characteristics, including DPs at the depth of 10 cm, PDD, and photon energy spectra with the different field sizes of $10 \times 10\ cm^2$, $5 \times 5\ cm^2$, and $2 \times 2\ cm^2$, the FF component was replaced by a metal plate of Al or W of 2 mm in the modeled linac head on a 12 MV photon beam linac .

The photon energy spectra on the bottom jaws were calculated using the scored PSF obtained from the BEAMnrc code at Z = 50 cm with BEAMDP(BEAM Data Processor) user code for FF and FFF modes using 100 energy bins.

The photon energy spectra from PSF was obtained using the BEAMDP code and graphs were plotted with the 2D graph plotting software QT-GRACE.

The initial histories were 3×10^9 particles on a $10 \times 10\ cm^2$ field size. Simulations using the BEAMnrc and DOSXYZnrc MC code were run on a desktop core i7 CPU with 8 GHz RAM on Ubuntu 14.04 system. The time was 144 hours for every PHSP file obtained by FF mode and 8 hours for every PHSP file with FFF mode.

5.2.3 Results

The statistical uncertainty of the MC BEAMnrc and DOSXYZnrc codes results was less than 1% for a range of depth from z = 0 cm to z = 25 cm. The discrepancy between measurements and MC for PDD and DP data was 1.5%/1mm for gamma index method (A. Zeghari, R. Saaidi, and R. Cherkaoui El Moursli, 4th International Conference on Automation, Control Engineering and Computer Science (ACECS - 2017)).

Figure 5.3 shows a comparison of MC which calculated PDD for FF and FFF modes and experimental results versus water phantom for 12 MV photon beam of SATURNE 43 linac with a field size of $10 \times 10\ cm^2$. At the depth of z = 0.5 cm, the fractional buildup dose was 31.56 % while it was 39.92 % for FFF mode. This demonstrated that for the 12 MV with FFF mode, the dose was higher than the flattened beam at depth of 0.5 cm.

The DP data in the figure 5.4 was normalized to the dose at central axis depth of 10 cm [129]. Beam profile data on $10 \times 10\ cm^2$ square field size were calculated at a depth of 10 cm for experimental data , FF, and FFF modes on 12 MV photon beam energy.

Figures 5.5, 6 and 7 show the photon energy spectra for FF and FFF modes on the bottom jaws of SATURNE 43 linac head for field sizes of $10 \times 10\ cm^2$, $5 \times 5\ cm^2$, and $2 \times 2\ cm^2$, respectively.

Figure 5.8 shows the electron energy spectra for FF and FFF modes on the bottom jaws of SATURNE 43 linac head for field size of $10 \times 10\ cm^2$.

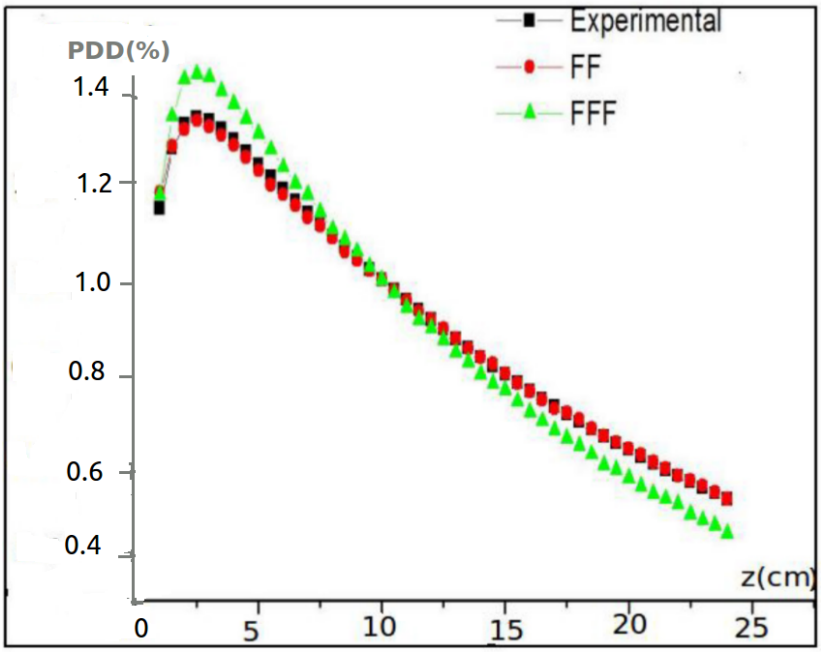

FIGURE 5.3: Comparison between PDD curve for experiment, FF, and FFF modes results in the water phantom for a 12 MV photon beam with a square field size of $10 \times 10\ cm^2$.

The photon fluence spectra were obtained by the BEAMDP user code analyzing the phase space file below the lower jaws for the following field sizes $10 \times 10\ cm^2$, $5 \times 5\ cm^2$, and $2 \times 2\ cm^2$, respectively.

The beam quality index (Q) specified by $TPR_{20,10}$ [130, 159, 161] for FF mode was kept the same for FFF mode defined as the absorbed dose ratio to water at the depth of 10 and 20 cm inside a water phantom along the beam axis. $TPR_{20,10}$ calculates the effective attenuation coefficient of the photon fraction inside the water phantom, and approximately indicates the description exponential decrease of the photon depth-dose curve and it is defined by the following equation [129]:

$$TPR_{20,10} = 1.2661.PDD_{20,10} - 0.0595 \tag{5.2}$$

where $PDD_{20,10}$ is the ratio of the percent depth-doses at 20 cm and 10 cm depths for a field size of $10 \times 10\ cm^2$ defined at the phantom surface with an SSD of 100 cm.

$TPR_{20,10}$ was calculated for FF and FFF modes for Al metal plate of 2 mm or by a W metal plate of 2 mm, which were to be 0.73, 0.66 and 0.67, respectively.

The calculated mean energies for all photon energy spectra for the FFF case were 2.48 MeV for Al metal plate of 2 mm and 2.74 MeV for a W metal plate of 2 mm on $10 \times 10\ cm^2$ field size.

5.2.4 Discussion

The Figure 5.3 shows the PDD data obtained on $10 \times 10\ cm^2$ square field size. In this figure, a difference between PDD values is observed that increased along the z axis. This results demonstrate that the PDD values for the FFF mode are slightly higher than FF mode on the same voxels along the z axis. The electron contaminations

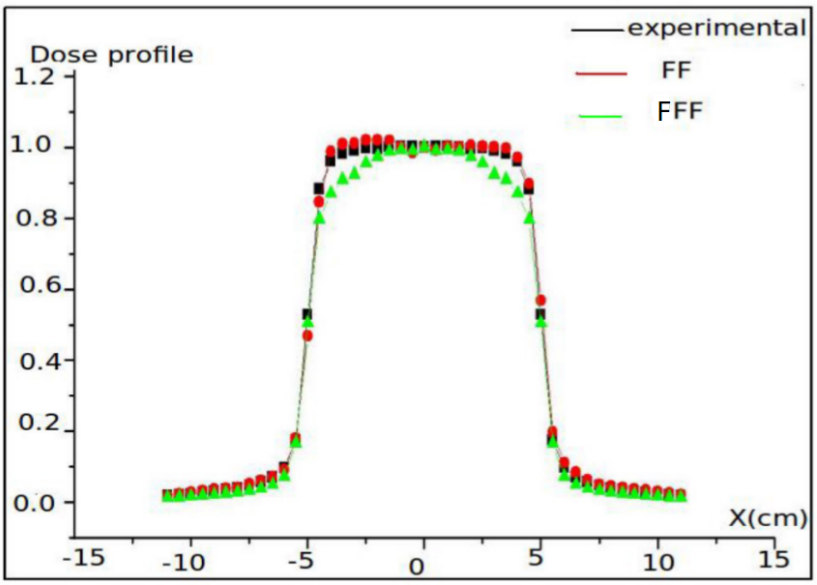

FIGURE 5.4: Comparison between cross-plane profiles dose for experiment, FF, and FFF modes results in the water phantom at 10 cm depth on 10 × 10 cm^2 field size for 12 MV photon beam.

have a significant effect in the build-up region and phantom surface and also lead to higher fluence of contamination electrons with FFF mode.

The dose rates at the maximum depth between filtered and unfiltered beams were calculated as the ratio of absorbed dose between the FF and FFF modes at the depth of maximum dose z_{Dmax} with the same number of initial electrons incident. The unfiltered dose rates were 3.94 and 2.74 times higher for 2 mm metal plate of Al and 2 mm for W metal plate, respectively on a 10 × 10 cm^2 field size.

Other authors found that for FFF mode, the dose rate increased by 5.5 and 2.31 for 18 and 6 MV [151, 153], respectively. Moreover, for a linac of 15 MV, the PDD rate increased by a factor of about 4 with field size of 10 × 10 cm^2 [117,149,157,158]. A study of a linac of 10 MV beam [130, 161] at the depth of z_{Dmax} showed that the difference varied from 3.4 % to 10.7 % for the 25 × 25 cm^2 and 2 × 2 cm^2 fields, respectively. For a 6 MV beam [130], the dose increased from 6.0 % to 14.6% for 25 × 25 cm^2 and 2 × 2 cm^2 square field sizes. The beam energy difference between the FFF and FF modes is the essential cause for the superficial dose difference between the FF and FFF modes, that FFF produces a higher superficial dose.

In another study, the buildup (defined between the depth of z = 0 cm and z = 1.5 cm) dose for energy 6 MV has showed a slight expanded dose on the both of square field sizes 2 × 2 cm^2 and 10 × 10 cm^2 for FFF mode than that with FF mode. However, the difference was not important. In the buildup region, at the depth of z = 0.5 cm, the fractional buildup doses for 6 MV FF mode varied from 85% to 87% which did not have an important distinction in comparison with 6 MV FFF mode which varied from 90 % to 91 %. A study for energy 10 MV also has leaded to a slight augmentation with FFF mode than that with FF mode for different depths in the buildup region. In the depth of z = 0.2 cm, for 10 MV flattened photon beam on a field size 10 × 10 cm^2, the dose increased from 20 % to 49 %. In parallel, for 10 MV FFF photon beam on the same field size, the fractional dose increased from

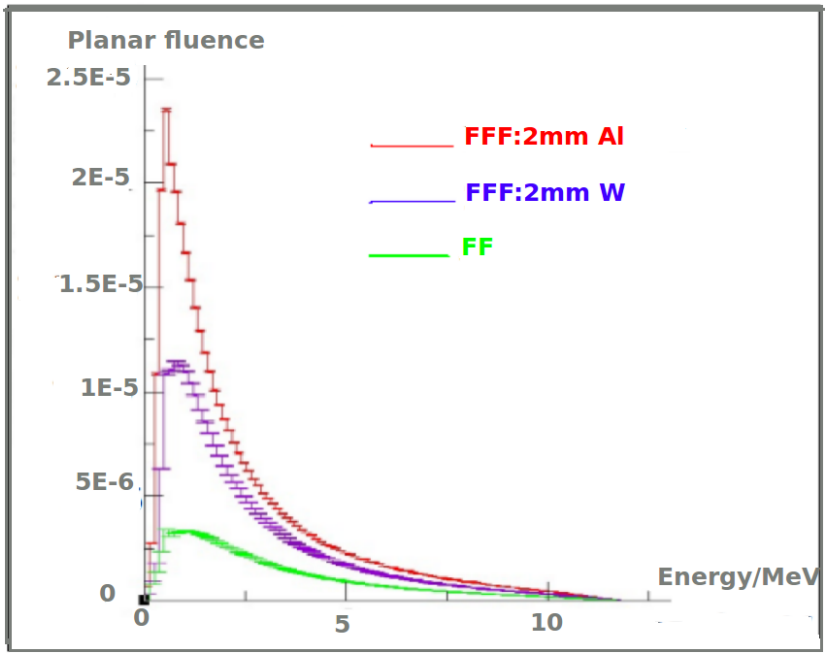

FIGURE 5.5: Photon fluence spectra: 2 mm of Al FFF mode, 2 mm of W FFF mode, and FF beam with the field size 10 × 10 cm^2 for 12 MV photon beam.

24% to 57%. At the depth of z = 0.5 cm for field size 10 × 10 cm^2 , the fractional doses in the buildup region for both 10 MV FF and 10 MV FFF modes varied from 75 % to 78 %. At the same depth for field size 2 × 2 cm^2 , the fractional doses varied between 67% and 72%. The advantages of the FFF mode consist of higher dose rate in surface and buildup regions and the decrease in the leakage of radiation photon in expanded treatment field. The using of FFF mode can be an advantage of treatment some types of cancer as prostate, brain, larynx, and pharynx, cranial or extra-cranial stereotactic treatments with small and medium field sizes.

In the cubic water phantom, the dose can be precisely calculated at any depths in the build-up and surface region. In contrary with clinical cases using the CT dataset, it is not easy to precisely measure the surface and buildup dose of the patient's dose.

Dose profile distribution was computed at depth of 10 cm on a 10 × 10 cm^2 square field size. The dose profile distribution in the penumbra region between the FFF and FF modes was slightly different, but the difference is not important [150, 156, 157, 160].

The distribution of the photon fluence and relative dose with FFF mode would be lower than dose received by the non-targeted area. The distribution of the profile dose in the out-of-field region was computed. It found that the DP distribution in this region was lower for FFF mode (Figure 7.37). This reason was supported in other studies by many authors [115, 149, 152, 155, 159].

$TPR_{20,10}$ data calculated for FF and FFF modes for an Al metal plate of 2 mm or by a W metal plate of 2 mm were 0.73, 0.66, and 0.67, respectively. It is seen that $TPR_{20,10}$ slightly decreased [130, 151, 160, 162] for the FFF beams. Some authors have been exploited the relationship between beam quality specifies and stopping power ratios of FFF beams and demonstrated that using % $dd(10)_x$ as beam quality

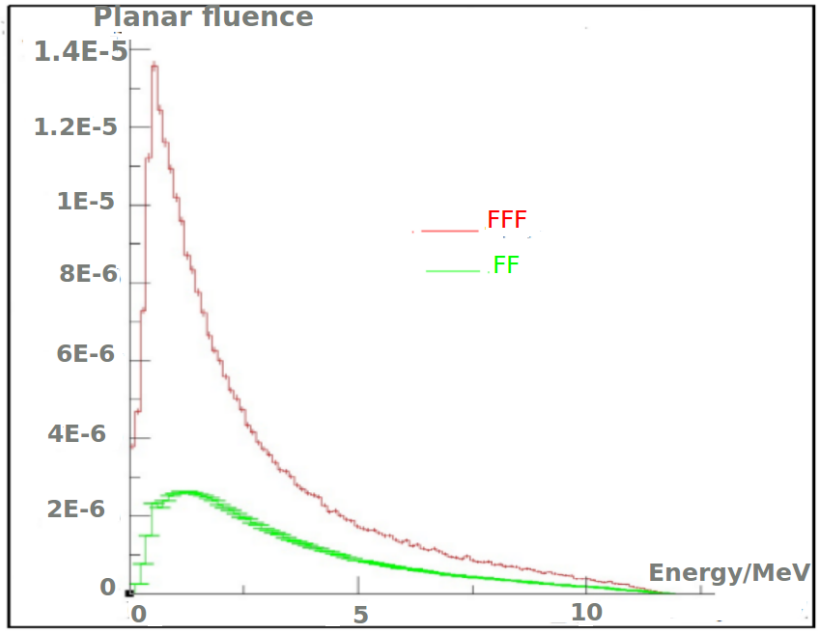

FIGURE 5.6: Photon fluence spectra: FFF mode and FF mode with the field size $5 \times 5\ cm^2$ for 12 MV photon beam.

specifier Spencer Attix stops power ratios for both FFF and FF modes leading to the same values of % dd(10)x within the acceptable calculation errors [128].

The ratios of photon fluence of FFF/FF beams were 7.44, 5.22 and 4.74 for the field size of $10 \times 10\ cm^2$, $5 \times 5\ cm^2$ and $2 \times 2\ cm^2$, respectively. This results for the ratios of photon fluence demonstrated that the photon fluence increases with the field size [115, 129, 155].

The FF component has a considerable responsibility of the attenuation of the photon fluence with FF mode. An important fraction of photons with low energy was absorbed by the thick central part of the flattening filter component, but with decreasing field size. Thus less fraction of photons with low energy can pass of thin lateral part of flattening filter component.

Our study shows that energy spectra with the FF mode are less soft than FFF mode. The calculated mean energy for all spectra shows that mean energy for the FFF case decreases from 3.29 to 2.48 MeV for Al metal plate for 2 mm and 3.29 to 2.74 MeV for a W metal plate of 2 mm on a $10 \times 10\ cm^2$ field size. The bremsstrahlung photons with low-energy level produced inside the target were absorbed by the two components, including flattening filter and primary collimator. When the flattening filter was replaced by a metal plate of Al, low-energy photons and the contaminating electrons can pass into the patient body and then contribute to the treatment beam. The contaminating electrons increased for FFF mode by 246.4 % in comparison to FF mode on a field size of $10 \times 10\ cm^2$.

The mean energy of the flattened beam decreased by a ratio of 1.33 for a metal plate of Al and 1.2 for a metal plate of W with $10 \times 10\ cm^2$ field size. We conclude that the mean energy decreased for the FFF mode. Many studies have been carried out on Elekta precise and Varian clinac 2100C linacs. There were some differences between previous works for mean energy and photon energy spectra with FFF mode [117, 147, 154, 162, 163]. The most previous studies were based on simulation with

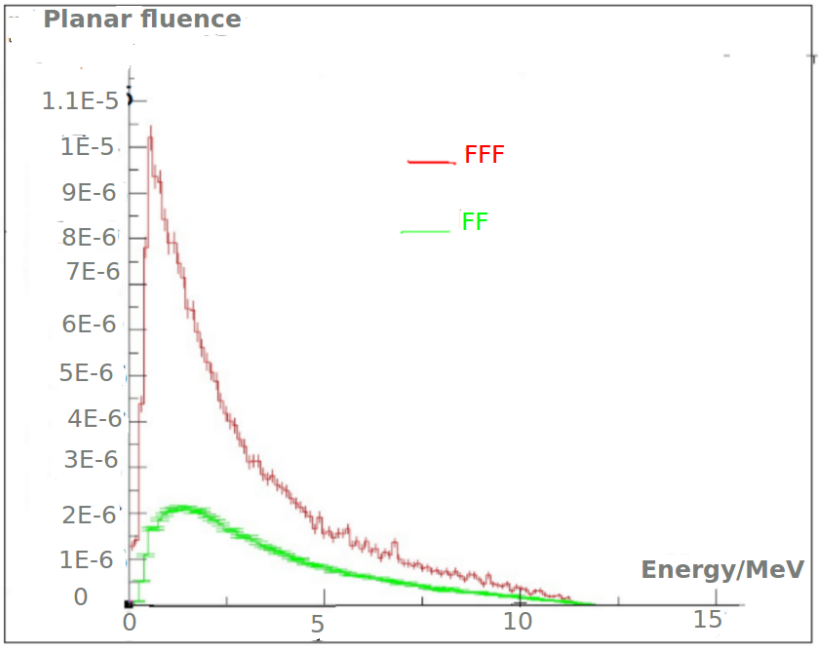

FIGURE 5.7: Photon fluence spectra: FFF mode and FF mode with the field size $2 \times 2\ cm^2$ for 12 MV photon beam.

FF removed from conventional flattened beam accelerators as our work but not on a real commercially clinical accelerators with FFF capability.

5.2.5 Conclusion

We have developed two models with FF and FFF modes for head linac SATURNE 43 with energy of 12 MV photon mode using the BEAMnrc MC User code. Our PDD calculations at the depth of maximum dose for FFF mode found an increase factor more than 3.94 in the dose rate with $10 \times 10\ cm^2$ field size. This increase in the buildup region dose for FFF mode was owing to contamination electrons generated in the FFF mode. Our computation of the dose profiles distribution has revealed a decrease in out of field doses for unflattened beams. The time was reduced more than 50 % for the FFF mode. The spectra of photon energy for both the flattened and unflattened modes were significantly different for all field sizes. In addition, the mean energy and the tissue phantom ratio decreased, and the photon fluence for the FFF mode was higher than FF mode. In conclusion, the actual study demonstrates directions for future researches related to the original questions about dosimetric properties of FFF beam of SATURNE 43 linac head.

5.3 Application to heterogeneous medium

5.3.1 Introduction

By using the BEAMnrc code, we have adjusted and validated the simulation parameters of the SATURNE 43 irradiation head in a homogeneous medium, by comparing the calculated and measured dose distributions using the gamma index

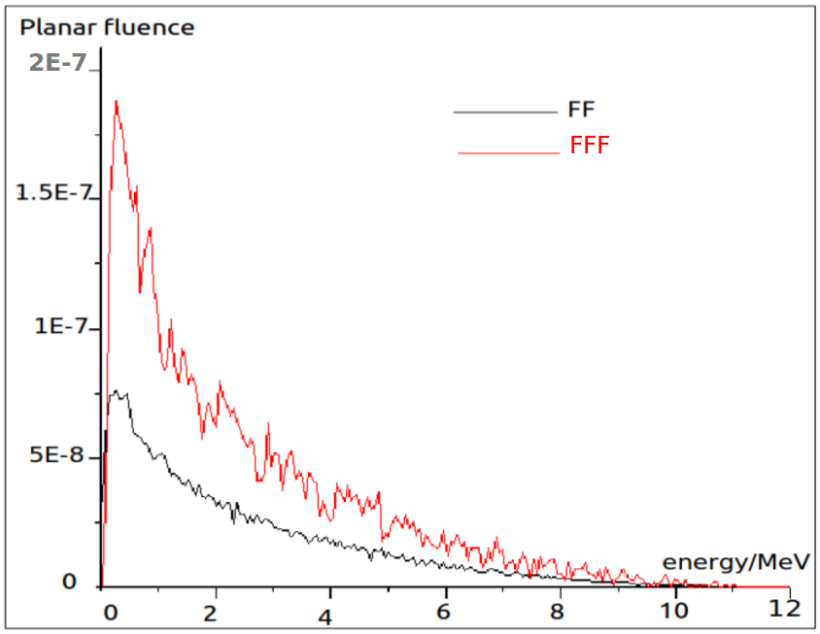

FIGURE 5.8: Electron fluence spectra for FFF mode and FF mode with the field size $10 \times 10\ cm^2$ for 12 MV photon beam.

criterion set at 1.5%/1mm. In practice, treatment planning systems (TPS) perform dose calculations in the different tissues constituting human body (heterogeneous media). The dose distributions are strongly modified by the presence of these tissues when they are irradiated by high energy photons beams. The attenuation of these beams varies with the structures encountered (bone, lung, ...) and comes mainly from Compton scattering. The human body has tissues such as bones, which having a very high attenuation coefficient and also composed by structures of low Z like the lung. Since the lung is essentially composed of air, it allows the totality of photon radiation to pass through it.

5.3.2 Materials and methods

5.3.2.1 Thickness and density of models OTP A, B, C and D

The DOSXYZnrc code was used to calculate and compare the dose distributions in heterogeneous phantom called Physical Test Objects (OTP) with homogeneous phantom.

The three OTP (A, B and C) make it possible to reproduce the majority interfaces encountered during radiotherapy treatments (water- bone, water-lung and water-bone-lung) and to check the dose calculations at the heterogeneities and the vicinity of the interfaces. A schematic representation of the three heterogeneous OTP (A, B and C) are shown in Figure 5.9, 10 and 11.

The (D) OTP (Figure 5.12) defines a clinical situation; it is a typical configuration of lung cancer mediatic localization. The water, PMMA, lung equivalent and bone equivalent media composition and densities used to define these OTPs are described in Table 5.8.

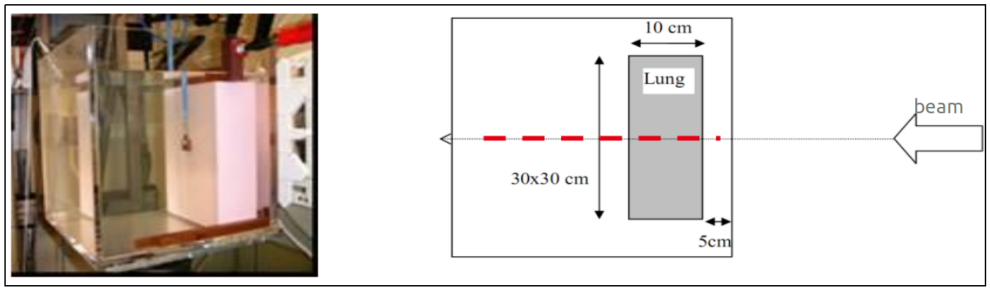

FIGURE 5.9: Schematic representation of heterogeneous OTP (A): water-lung.

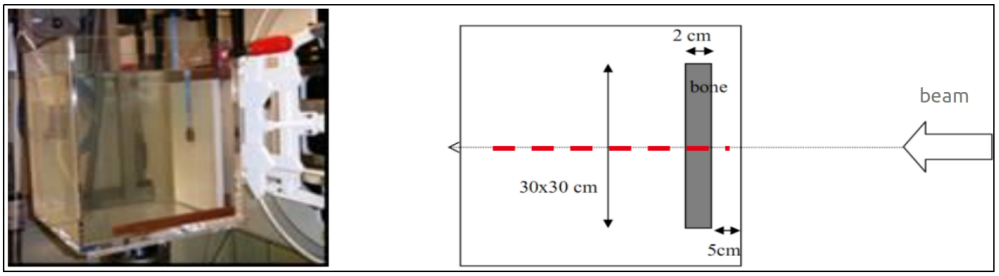

FIGURE 5.10: Schematic representation of heterogeneous OTP (B): water-bone.

5.3.2.2 DOSXYZnrc simulation for heterogeneity

The DOSXYZnrc code was originally designed for dosimetry in medical physics. With our present work we wish to exploite the reliability and the flexibility of the DOSXYZnrc code in the real dosimetry in medical physics generally and in external radiotherapy especially.

The simulation parameters of SATURNE 43 linac have been adjusted and validated in a homogeneous water phantom, by comparing the calculated and measured results using the gamma index creterion.

The PHSP file scored in the M1 model (which corresponds to mean energy of 11.8 MeV and a focal spot size of 0.17 cm during the adjustment of incident electron beam characteristics), will be used as a input source of radiation in DOSXYZnrc code for dose distribution calculations with the four OTP objects that are already described with details in section before. For the first three OTP objects, we considered 2×10^8 particles to be simulated (each particles is recycled 10 times), which improve the statistical calculation of the PDD for the different clinical situations (water-lung, water-bone, water-lung-bone). The volume chosen for the calculations of PDD in the first three objects was a parallelepiped of dimension $40 \times 40 \times 40\ cm^3$ voxelized as $0.5 \times 0.5 \times 0.5\ cm^3$.

In our first test calculation of PDD (see figure 5.13) in a heterogeneous phantom (A), we observed that, the dose exhibits an unpredictable variation in the interface between two regions of different materials (water-lung); so we get a dose peaks in the points near boundaries between water and lung. This phenomenon is known as the Interfaces artifact. The condensed histories algorithm was used to simulate boundaries traversing by charged particles.

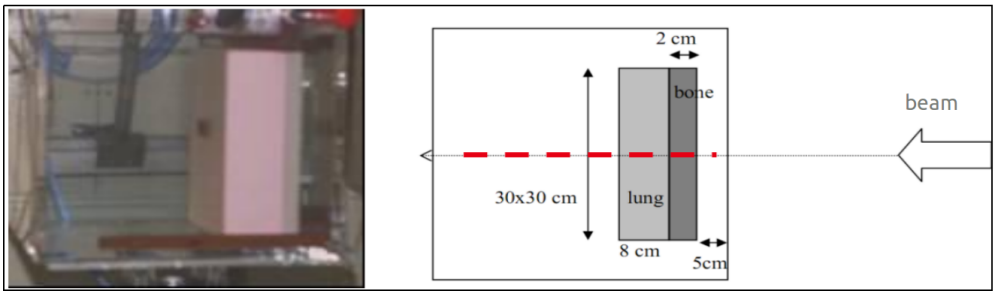

FIGURE 5.11: Schematic representation of heterogeneous OTP (C): water-bone-lung.

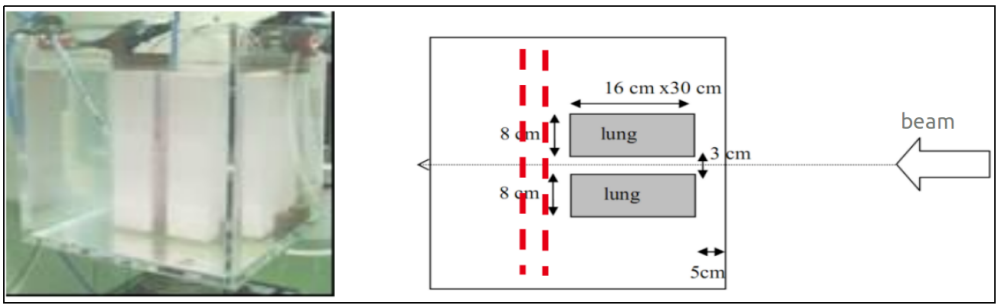

FIGURE 5.12: Schematic representation of heterogeneous OTP (D).

To fully explain the effect of the interface artifact, we consider the following example. The accuracy of the electron transport is crucial to ensure the accuracy of the dose calculation in a heterogeneous medium. This accuracy requires that the step size be very fine which causes a long calculation time. In order to avoid the incorrect calculation of the dose in the interfaces of medium heterogeneity, we minimize the step size parameter for charged particles to 0.1 mm in traversing the boundaries of phantom for object (D) in our simulation, that we simulated 5×10^8 particles (each history was recycled 10 times) for the calculation of the DP at depth 22 cm and 25 cm, respectively. We used the voxels size of $0.1 \times 0.1 \times 0.1\ cm^3$ in this calculation of DP.

5.3.3 Results and discussion

In this simulation, We compared the PDD data obtained in a homogeneous water phantom with those calculated for every heterogeneous phantom of A, B, and C configuarions. After that, we compared the DP calculated in a homogeneous water phantom with that of a heterogeneous phantom of D configuration. For All these simulations, we used the DOSXYZnrc code to model these configurations (A, B, C, and D) to study the dose distribution.

In the case of A, B and C configurations, the results are given by the ratio of the dose in heterogeneous cases to the dose at depth 10 cm in a homogeneous case (water phantom). The normalization formula for these cases is given as:

$$PDD(z) = \frac{Dose(z)_{heterogeneous}}{Dose(10cm)_{homogeneous}} \tag{5.3}$$

TABLE 5.8: Characteristics (density and composition) of medium used for models OTP A, B, C and D.

	Density (g/cm^3)	H	C	N	O	Mg	P	Cl	Ca
Lung equivalent	0.3	8.33	60.08	2.73	23.04	4.8		1.02	
Bone equivalent	1.8	3.73	30.11	1.08	33.55	2.02	7.83	0.04	21.57
water	0.9982	11.11			88.89				
PMMA	1.19	8	60		32				

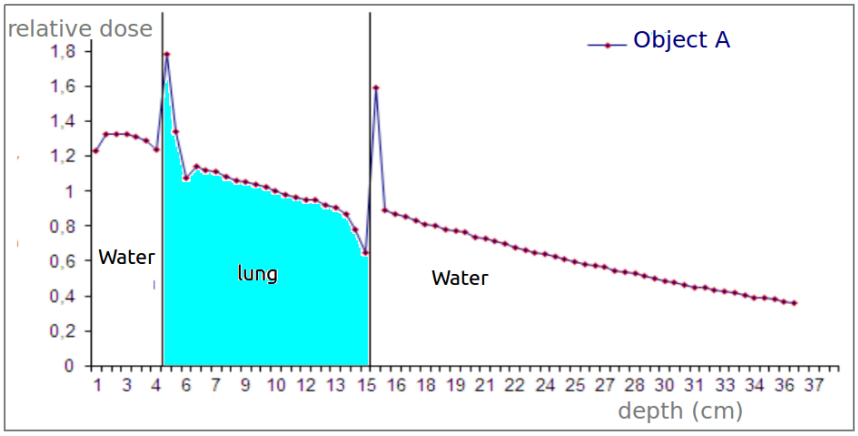

FIGURE 5.13: Illustration of artifact effect in calculation of PDD in a heterogeneous phantom (water-lung-water).

For object D, the DP calculated at z_1 = 22 cm and z_2 = 25 cm are normalized at the dose value in the beam axis. The value of $DP(z_1 or z_2)$ is given by:

$$DP(z_1, z_2) = \frac{Dose(z_1, z_2)_{heterogeneous}}{Dose(10cm)_{homogeneous}} \tag{5.4}$$

5.3.3.1 Interface water-lung-water (object A)

A comparison between the PDD calculated in a homogeneous water phantom with the PPD calculated in a heterogeneous phantom (which presents a water-lung-water interface) with the DOSXYZnrc code for SATURNE 43 on 12 MV photon beam is shown in Figure 5.14. For PDD calculation, we used the maximum step 1 mm. We noticed that for both PDD curves, the dose is normalized to a reference depth of 10 cm.

If we compare the calculated PDD in object A illustrated in the figure 5.14 above with that of figure 5.13, we can find that the artifact phenomena at the interfaces have been disminished, this is due to the maximum size step which has been minimized to 1 mm.

In addition, there are less fluctuations in the boundaries interfaces water-lung that can be solved again by admitting a very fine step size (some um or nm), but this can cost a long calculation times.

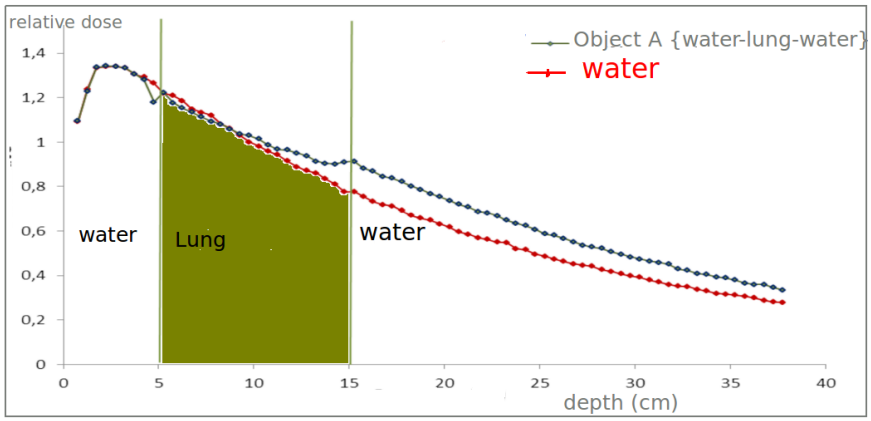

FIGURE 5.14: Comparison of PDD calculated between a heterogeneous water phantom (water-lung-water) and homogeneous water phantom on 12 MV photon beam, a $10 \times 10\ cm^2$,field size and SSD of 100 cm.

Now, we make a comparison between two PDD curves obtined on water only and water-lung-water, see figures 5.14. To ensure a good interpretation of the results, we will divide the PDD curves to three regions:

¶Region 1: 1 cm $\leq depth \leq$ 5 cm:

For this region, the PDD points for both curves are calculated in water, we note that both curves coincide perfectly. This can be explained by the fact that this region is not influenced by the presence of a material of different density, since this density is low (Lung, 0.3 g/cm^3), so it will not have any contamination of charged particles backscattered by this heterogeneity (lung).

¶Region 2: 5 cm $\leq depth \leq$ 15 cm:

For this second region, we introduced a thick lung of 10 cm at the depth 5 cm in the case of object A, the spectrum of photons from the irradiation head is multi-energy and difficult to explain. The attenuation of this clinical beam is described by the attenuation coefficients that depending on photon energy and absorbing medium depth. Since the lung density is low, the most incoming photons will cross this region. Therefore, the secondary electrons created by the high energy photons were the principals contributors of the dose in this region. At the first depth of lung thickness modeled 5 cm $\leq$ *depth* $\leq$ 8 cm , it is remarked that the dose is lower in heterogeneous water phantom than that in homogeneous water phantom, it is possible to explain this result as; the lung has a low density; the electrons of high energy moved by the photons in region 1 have a path relatively higher than that in water only which deposit their energies at a distance of 8 cm of the modeled lung. The dose for heterogeneity phantom (lung) is lower than that calculated in water phantom only for the first depth of the lung thickness. The dose for heterogeneity phantom (lung) is higher than calculated in water phantom only at a depth greater than 8 cm of the thickness of the lung.

¶Region 3 : depth $\geq$ 15 cm:

For this region, it is noted that the absorbed dose calculated in the case of a medium A (lung) is higher than that calculated in a homogeneous water. To traverse the thickness of lung 10 cm by an electron, it must have a kinetic energy greater or equal to 6 MeV, this energy represents a half maximum energy of the photons 12

MV transferring to secondary electrons. Assuming that the majority of the electrons moved by the 12 MV photons in region 1 have an energy greater than 6 MeV in the boundaries of the water-lung interface, these electrons will deposit their energies in region 3 (without interact with the modeled lung) which contribute to increase the dose at the exit since the secondary electrons will not be stopped in the lung of low density. On the other hand, the attenuation coefficient of the lung is very low, so the most photons which aren't attenuated in region 1 have a high probability of crossing region 2 (low density) and to transfer their energies to the secondary electrons that can be created in the region 3, which therefore contributes to increasing the dose in this region.

5.3.3.2 Interface water-bone (object B)

A comparison between the PDD calculated in a homogeneous water phantom with the PDD calculated in a heterogeneous water phantom (interface water-bone-water) with DOSXYZnrc code relative to a 12 MV photon beam produced by SATURNE 43 linac. The results are shown in Figure 5.15. We have considered the maximum size of the step equal to 1 mm.

For both PDD curves, the dose is normalized to a reference depth of 10 cm.

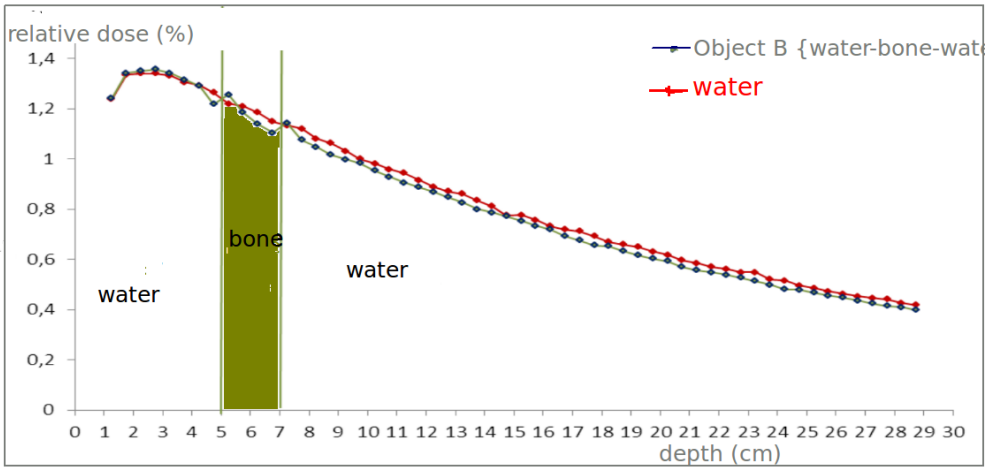

FIGURE 5.15: Comparison of PDD calculated between a heterogeneous water phantom (water-bone-water) and homogeneous water phantom on 12 MV photon beam, a 10×10 cm^2,field size and SSD of 100 cm.

If we compare the calculated PDD in object B with that in a homogeneous medium of water illustrated in the figure above 5.15, the curves can be divided into three regions:

¶Region 1 : 1 cm $\leq$ *depth* $\leq$ 5 cm:

For this first region, where the PDD points for both PDD curves are calculated in water, it is noted that there is a slight increase in the dose in this region for the case of the heterogeneous medium B. This increase can be explained by the fact that the electrons backscattered by the bone will be deposited their energies in the region 1.

¶Region 2: 5 cm $\leq$ *depth* $\leq$ 7 cm:

For this second region, we add a bone thickness of 2 cm at the depth of 5 cm in the water phantom (interfaces water-bone-water), we noted a slight decrease in dose for

the heterogeneous region in comparison to the dose calculated for the homogeneous water phantom. We note that the bone having a high attenuation coefficient, so this decrease can be explained.

¶Region 3 : depth $\geq$ 7 cm:

For this region, the PDD points for both curves are calculated in water region, it is remarked that there is a slight decrease in the dose distribution for the case of heterogeneous phantom (water-bone-water) in comparison to the dose in the same region in a homogeneous water phantom. The importance of this decrease depends on the thickness of the modeled bone, when this thickness increases, the dose in this region decreased because some high energy photons that will move the electrons in region 3, will be attenuated in the bone because it has a high attenuation coefficient.

5.3.3.3 Interface water-bone-lung (object C)

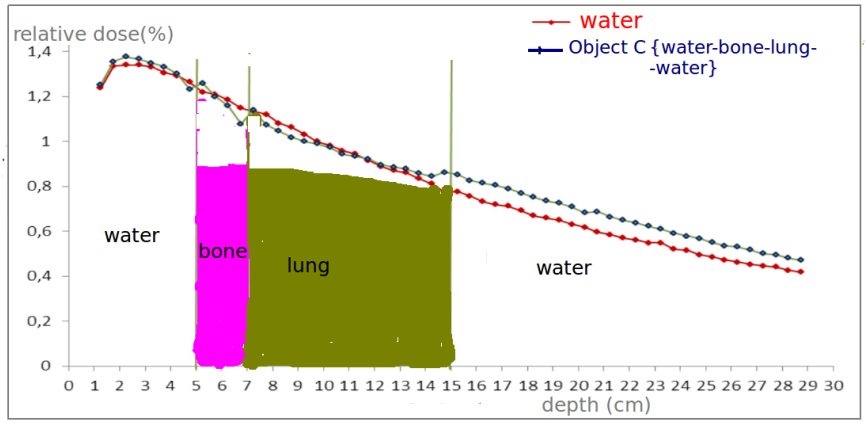

FIGURE 5.16: Comparison of PDD calculated between a heterogenous water phantom (water-bone-lung-water) and homogenous water phantom on 12 MV photon beam, a 10 $\times$ 10 cm^2,field size and SSD of 100 cm.

If we compare the calculated PDD in the OTP (C) with that in a homogeneous water phantom illustrated in the figure 5.16, we can divide the curves into four regions:

¶Region 1: 1 cm $\leq$ *depth* $\leq$ 5 cm:

For the first region, the dose points for both curves are calculated in a water region, we observe a light increase in dose for the case of heterogeneous phantom (medium C) in comparison to homogeneous water phantom. This can be explained by the backscattered electrons from the bone which deposited their energies in the region 1.

¶Region 2: 5 cm $\leq$ *depth* $\leq$ 7 cm:

For the second region, we introduced a bone plaque thickness of 2 cm in the phantom water, we remark a light decrease in the dose for this region (medium C) in comparison to the dose calculated in the same region for the homogeneous water phantom. We know that the bone have a high attenuation coefficient, so this decrease was refereed to this high attenuation coefficient.

¶Region 3: 7 cm $\leq$ *depth* $\leq$ 15 cm:

For this region, the dose exhibits the same variation such as of the dose in region 2 of object B, but the presence of a low thickness of bone (high density) plaque to backscattered photons in this region decreases slightly the dose.

¶Region 4 : depth≥ 15 cm:

The fourth region exhibits the same variation as region 3 of object A, but the dose increased slightly in comparison to the dose in the same region for object A, because of the presence of a high density medium for the photons, also the dose in this region depends on the previous dose regions.

5.3.3.4 Mediastinum configuration (object D)

For the object D, we modeled the heterogeneous phantom with voxels dimensions of $0.1 \times 0.1 \times 0.1\ cm^3$ to calculate the DP. We know that when the spatial resolution of the detection volume increases, we have to simulate more particles to minimize the statistical uncertainties but the time increases more. After two days of calculation, we have obtained a DP calculated in a heterogeneous medium D in two depths: 22 cm and 25 cm. Figures 5.17 and 18 give the DP calculated by the MC DOSXYZnrc user code.

It is noted that the doses generated by the calculation points were normalized to the dose at the central axis.

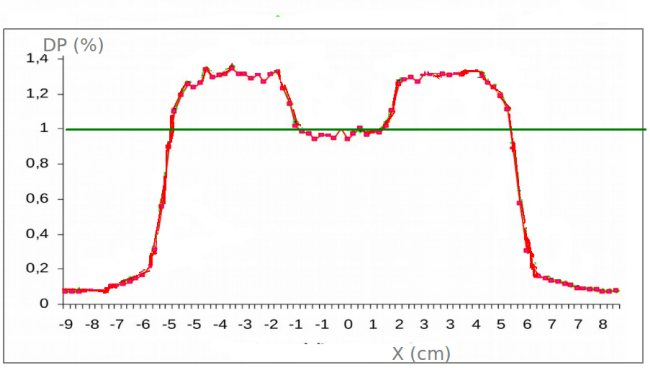

FIGURE 5.17: Curve of DP calculated with DOSXYZnrc at the depth 22 cm on 12 MV photon beams, a $10 \times 10\ cm^2$ field size and SSD of 100 cm.

The figure 5.17 and 18 showed that the DP calculated with the DOSXYZnrc code have some statistical fluctuations, this fluctuation can be explained by insufficient number of histories simulated. To solve this problem we must increase the number of histories to eliminate statistical fluctuations or using the VRTs that can optimize the simulation efficiency.

5.3.4 Conclusion

We entirely finished our study in this section, by simulating and analyzing the dose distributions in the heterogeneous water phantoms for the following configurations: (water-lung-water (object A), water-bone (object B), water-bone-lung (object C) and mediastinum configuration (object D)) practically adopted in the beam quality control for clinical radiotherapy. This simulation highlighted the potential of the

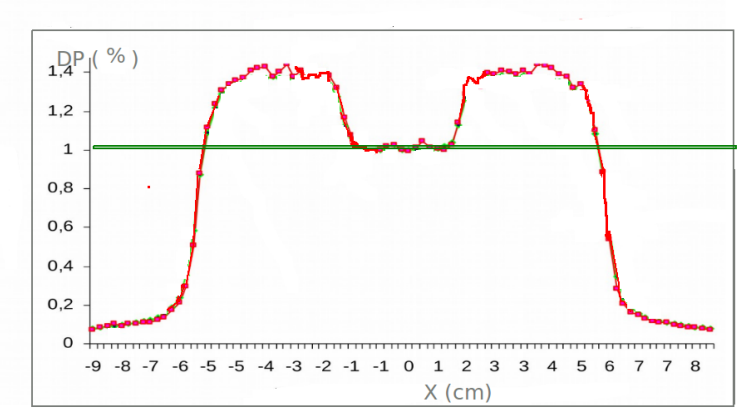

FIGURE 5.18: Curve of DP calculated with DOSXYZnrc at the depth 25 cm on 12 MV photon beams, a 10 $\times$ 10 cm^2 field size and SSD of 100 cm.

DOSXYZnrc MC calculation to correctly reproduce the dose distributions and, more specifically, the effect of the interface artifact, that pose problems for conventional TPS.

Conclusion and further works

Conclusion

In radiotherapy, the accuracy of the dose calculation for the treatment planning for the patient is important. MC method is considered as the most accurate technique for this purpose if the radiation source and the patient are well modeled. Indeed, the advantage of the MC calculation of the dose is its ability to accurately simulate the transport of radiation in the accelerator head and in the heterogeneous structures of the patient.

In this work, we have been modeled a 12 MV photon mode for SATURNE 43 accelerator with an irradiation field size of $10 \times 10\ cm^2$. We presented a method of adjusting characteristics of the incident electron beam. Our methodology of the calculation is designed to be fast and precise, which allowed us to validate our MC BEAMnrc results with experimental data generated by SATURNE 43 linac in LNHB/France.

Our results showed a good agreement between the MC and experimental data for incident electrons with energy 11.8 MeV and FWHM = 0.17 cm. So the impact of incident electron beams on the tungsten target is principally characterized by these parameters: nominal energy and focal spot size described by the Gaussian spatial distributions. MC simulation of the treatment head of SATURNE 43 machine was successfully done using BEAMnrc code. The linac dosimetric characteristic obtained with our simulations studies such as PDD and DP were in good agreement with the experimental measures and the $TPR_{20/10}$ was well matching with the published values with others MC codes (PENELOPE, GEANT4, MCNPX...). That shows the efficacy and accuracy of the method of changing the initial properties of electron source to obtain the discrepancies results within 1%/1 mm in this present project.

After that, our works focused on improving the efficiency of MC calculation by applying different VRTs in our models. VRTs implemented in BEAMnrc/DOSXYZnrc are more efficient in comparison to other codes. Also, we noted that when these techniques are used in combination in parallel, the simulation efficiency becomes very important. These techniques are applied on the SATURNE 43 linac to optimize the calculation time and improve the statistical errors on the results.

This project have been investigated the efficiency of the photon beam dose and fluence calculations with BEAMnrc for SATURNE 43 linac. The main result of this work was to demonstrate that, when employed VRTs parameters combined in BEAMnrc, the difference in efficiency between the simulations utilizing the VRTs combined in parallel and analogue simulation becomes more important. In this way, employing VRTs combined in parallel simulation with a BEAMnrc code have been improved the photon beam dose efficiency about 19000 times in comparison to

these of the analogue simulation. In addition, we have been demonstrated that the DBS have been presented a significant improvement in photon fluence efficiency in comparison to BCSE, $ICM\_SPLIT(e^-/e^+)$, and UBS, respectively. Also, DBS have been increased the photon fluence efficiency by 4652 times compared to analogue simulation. Therefore, we have demonstrated that our results have a higher photon beam dose calculation efficiency than MCNPX code in case of analogue simulation (without VRTs).

The major advantage of employing of VRTs combined in parallel simulation was the significant improvement gain in calculation time without a compromise in the accuracy of the patient dose computation.

After having characterized the photon beams of the accelerator, we determined the energy spectra of the photons produced and the effect of certain parameters, such as the field size and the FFF, on the photon spectra and the dose distribution of the accelerator SATURNE 43. So, we have developed two models with FF and FFF modes for head's linac SATURNE 43 with energy of 12 MV photon mode using the BEAMnrc MC User code. Our PDD calculations at the depth of maximum dose for FFF mode found an increase factor more than 3.94 in the dose rate with $10 \times 10\ cm^2$ field size. This increase in the buildup region dose for FFF mode was mainly due to the contamination electrons generated in the FFF mode. Our computation of the DP distribution has revealed a decrease in out of field doses for unflattened beams. The time was reduced more than 50% for the FFF mode. The spectra of photon energy for flattened and unflattened modes were significantly different for all field sizes. In addition, the mean energy and the tissue phantom ratio decreased, and the photon fluence for the FFF mode was higher than FF mode.

In conclusion, the actual work demonstrated the directions for future research works related to the original questions about dosimetric properties of FFF beam of 12 MV SATURNE 43 linac head.

We completed our studies on the 12 MV SATURNE 43 accelerator, by evaluating the behavior of dose distributions in the presence of heterogeneities (water-lung-water (object A), water-bone-water (object B), water-bone-lung-water (object C) and Mediastinum configuration (object D)) when they are irradiated by a beam of photons 12 MV from the irradiation head SATURNE 43.

Further works

Further to the different investigations presented in this study, various aspects may be studied in the future. One of these studies might be related to:

1. Implementation of the MLC component to SATURNE 43 linac for supplying intensity modulated fields in recent techniques.

2. Implementation of Wedge component on 12 MV SATURNE 43 linac to alter the photon beam intensity and provide oblique isodose distribution.

3. Utilization of other codes such GEANT4 and FLUKA for modeling 12 MV SATURNE 43 linac to study the neutron contamination.

4. Utilization of combined VRTs in cluster for calculations of dose distribution inside a homogeneous and heterogeneous phantoms.
5. Monte Carlo study of out-of-field dose distributions on 12 MV SATURNE 43 linac operating with and without a flattening filter.

Appendix A

list of Publications

1. Zeghari A, Saaidi R, Mghar M, Cherkaoui ElMR, "Monte Carlo Study of Photon Dose Distributions Produced By 12 MV Linear Accelerator", *J of Biosens Biomark Diagn*, vol. 3, no. 1, pp. 1-5, 2018.
2. A. Zeghari, R. Saaidi, R. Cherkaoui El Moursli "Investigation of variance reduction techniques parameters to enhance the efficiency for a 12 MV photon beam", *Journal of Radiation Research and Applied Sciences*, vol. 12, no. 1, pp. 192-199, 2019.DOI:10.1080/16878507.2019.1623573.
3. Zeghari A, Saaidi R, Cherkaoui El Moursli R., "Enhancement of the Dose on 12 MV Linac with Free Flattening Filter Mode", *J Biomed Phys Eng*, vol. 9, no. 4, vol. 9, no. 4, pp. 437-444, 2019.Doi.org/10.31661/jbpe.v0i0.924.
4. Zeghari A, Saaidi R, Cherkaoui El Moursli R., "Monte Carlo study of a free flattening filter to increase surface dose on 12 MV photon beam", *International Journal of Radiation Research*, Vol. 18, no. 2, pp. 307-313, 2020. DOI: 10.18869/acadpub.ijrr.18.2.30
5. Rahal SAAIDI, Yassine TOUFIQUE, Abdelkrim ZEGHARI, Abderrahman EL KHARRIM, Rajaa Cherkaoui EL MOURSLI, "GATE Simulation Study of the Siemens Biograph mCT 20 Excel PET/CT System", *Pol J Med Phys Eng*, vol. 25, no. 1, xx-xx, 2018. Doi: 10.2478/pjmpe-2019-00xx.
6. A Zeghari, R Saaidi, M Mghar, A Marouani, A Darif, S Kadouch and R Cherkaoui el Moursli, "'Monte Carlo study of photon dose distributions produced by saturne 43 linear accelerator", *3 rd International Conference on Medical Physics Biomedical Engineering*, November 07-08, Barcelona, Spain, 2016.
7. A.ZEGHARI*, R.SAAIDI, M.MGHAR, R. CHERKAOUI EL MOURSLI, "Modeling of a Linear Accelerator Saturne 43 and Study of Photon Dose Distributions", *4 th International Conference on Automation, Control Engineering and Computer Science (ACECS - 2017) Proceedings of Engineering and Technology - PET*, Vol. 19, pp. 104-110., March 28-30, Tangier, Morocco, 2017.
8. A. Zeghari, R. Saaidi, R. Cherkaoui El Moursli, "Investigation of nanoparticle to increase skin dose on a 12 MV free flattening filter photon beam", *The third International Conference on Electromagnetic Radiation & Impact on the Environment JREMIE'3*, April 28, Tetouan, Morocco, 2018.

Appendix B

SATURNE 43 treatment head

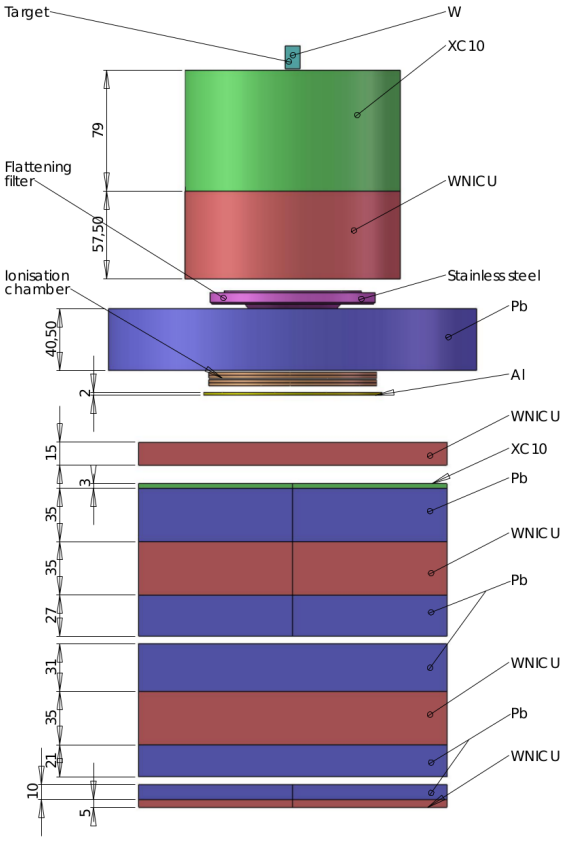

Cross-sectional (YZ) view of SATURNE 43 treatment head.

Bibliography

[1] Amaldi U., Rana A. L. U. Amaldi, A.LA. Rana, "Particle Accelerators: From Big Bang Physics to Hadron Therapy", *Springer International Publishing Switzerland*, 2015.

[2] http://en.wikipedia.org/wiki/File:Roentgen-x-ray-1896-01-23.jpg

[3] E. F. De los Santos et al., Medical Physics Practice Guideline 4.a: Development, implementation, use and maintenance of safety checklists,*J Appl Clin Med Phys* , vol. 16, no. 3, pp. 37–59, 2015.

[4] Report 23, "Measurement of absorbed dose in a phantom irradiated by a single beam of X-ray", *Journal of the International Commission on Radiation Units and Measurements*, vol. 12, no. 2, 1973.

[5] D. G. Kate-Louise and P. Gray ,"Radiation In Medicine: A Need For Regulatory Reform", *Journal of the International Commission on Radiation Units and Measurements*, pp. 1–326, 1996. ISBN-10:0-309-05386-2.

[6] I. C. R. P., International Commission on Radiological Protection), "Radiation In Medicine: A Need For Regulatory Reform", *Oxford: Pegamon Press* , ICRP Publication 1, 1958.

[7] A. S. Pradhan, Evolution of dosimetric quantities of International Commission on Radiological Protection (ICRP): Impact of the forth coming recommendations, *J Med Phy*, vol. 32, no. 3, pp. 89–91, 2007.

[8] K. M. Khan, J. P. Gibbons "The Physics of Radiation fifth edition", *Wolters Kluwer Philadelphia Hong Kong London Buenos Aires Sydney Tokyo* , 2014.

[9] D. I. Thwaites and J. B. Tuohy, " Back to the future: the history and development of the clinical linear accelerator", *Phy Med Biol* , vol. 51, no. 13, pp. 343–62, 2006.

[10] R. Mohan and D. Grosshans, "Proton Therapy – Present and Future", *Adv Drug Deliv Rev* , vol. 109, pp. 26–44, 2017.

[11] J. D. Bourland, "Chapter 6 - Radiation Oncology Physics", *Clinical Radiation Oncology* , vol. 4, pp. 93–147, 2016.

[12] T. V. Ajithkumar, "Principles of radiotherapy", *Specialist Training in Oncology* ,vol. 51, no. 13, pp. 15–29, 2011.

[13] S. F. Kry et al. "AAPM TG 158: Measurement and calculation of doses outside the treated volume from externalbeam radiation therapy", *Med Phys* , Suzhou, China, vol. 44, no. 10, pp. 1–41, 2017.

[14] B. Cho, "Intensity-modulated radiation therapy: a review with a physics perspective", *Radiat Oncol J* , vol. 36, no. 2, pp. 1–10, 2018.

[15] J. UrRehman et al., "Intensity modulated radiation therapy: A review of current practice and future outlooks", *J of Radiat Res and Appl Sci* , vol. 11, no. 4, pp. 361–67, 2018.

[16] A. Pirzkal, M. Carol, F. Lohr, A. Hoss, M. Wannenmacher and J. Debus, "Comparison of intensity-modulated radiotherapy with conventional conformal radiotherapy for complex-shaped tumors", *International Journal of Radiation Oncology Biology Physics* , vol. 48, no. 5, pp. 1371–80, 2001.

[17] Y. Zhao et al.,"A clinical study of lung cancer dose calculation accuracy with Monte Carlo simulation", *Radiation Oncology* , vol. 9, no. 1, 2014.

[18] D. I. Thwaites and J. B. Tuohy, "Back to the future: The history and development of the clinical linear accelerator", *Physics in Medicine and Biology* , vol. 51, no. 13, pp. 343–62, 2006.

[19] E. B. Podgorsak, "Radiation Oncology Physics: A Handbook for Teachers and Students", *INTERNATIONAL ATOMIC ENERGY AGENCY VIENNA* , pp. 1–696, 2005.

[20] M. Moradian, R. Nath, L. L. Anderson, J. A. Meli, A. J. Olch, J. A. Stitt, J. F. Williamson, "Code of practice for brachytherapy physics: report of the AAPM Radiation Therapy Committee Task Group No. 56. American Association of Physicists in Medicine", *Med Phys* , vol. 24, no. 10, pp. 1557–98, 1997.

[21] J. F. Williamson et al. , "Recommendations of the American Association of Physicists in Medicine regarding the impact of implementing the task group 43 report on dose specification for 103Pd and 125I interstitial brachytherapy", *Med Phys* , vol. 32, no. 5, pp. 1424–39, 2005.

[22] S. Takahashi, "Conformation radiotherapy: Rotation techniques as applied to radiography and radiotherapy of cancer ", *Acta Radiol Diagn (Stockh)* , vol. 242, 1965.

[23] L. D. Lunsford, "The development of the international stereotactic radiosurgery society", *J Radiosurg SBRT* , vol. 1, no. 2, pp. 77–83, 2011.

[24] A. Dimitriadis, "Assessing the dosimetric and geometric accuracy of stereotactic radiosurgery", Thesis, University of Surrey Guildford - Faculty of Engineering and Physical Sciences, Surrey GU2 7XH, U.K, 2016.

[25] A. A. F. De Salles et al., "Evolution of Stereotactic Radiosurgery", *Springer, Berlin, Heidelberg* , pp. 3–10, 2011.

[26] T. Piotrowski, "Total skin electron irradiation-The technique where the electron beams are still irreplaceable", *Rep Pract Oncol Radiother* , vol. 19, no. 2, pp. 69–71, 2014.

[27] T. Piotrowski, P. Milecki, M. Skórska, D. Fundowicz, "Total skin electron irradiation techniques: A review", *Postepy Dermatologii I Alergologii* , vol. 30, no. 1, pp. 50–55, 2013.

[28] A. Pilar, M. Gupta, S. Ghosh Laskar, S. Laskar , "Intraoperative radiotherapy: review of techniques and results", *Ecancermedicalscience* , vol. 11, no. 750, 2017.

[29] E. L. Walter, R. Vikram, A. A. Riccardo, "Modern Management of Cancer of the Rectum", *Springer Londons* , 2015.

[30] P. Mayles, A. Nahum, J. C. Rosenwald,"Chapter: 46-Handbook of Radiotherapy Physics Theory and Practice", *CRC Press taylor & Francis Group* , 2007.

[31] F. Khan, "The Physics of Radiation Therapy", *Williams and Wilkins* , Baltimore, 1984.

[32] E O. Lawrence, N. E. Edlefsen, "The Production of High Speed Protons Without the use of High Voltage", *Science* , vol. 72, no. 1, pp. 376–77, 1930.

[33] D. W. Kerst, "Acceleration of Electrons by Magnetic Induction", *Phys Rev* , vol. 58, no. 1, pp. 841–841, 1940.

[34] R. Wideröe, "About a new principle for producing high voltages", *Archiv für Elektrotechnik* , vol. 21, pp. 387–387, 1928.

[35] R. J. Van de Graaff, "A 1,500,000 volt electrostatic generator", *Phys Rev* , vol. 387, pp. 1919–20, 1931.

[36] R. Anderson, M. Lamey, M. MacPherson, "Simulation of a medical linear accelerator for teaching purposes", *JOURNAL OF APPLIED CLINICAL MEDICAL PHYSICS* , vol. 16, no. 3, pp. 1-19, 2015.

[37] B. Whelan, "Performance of a clinical gridded electron gun in magnetic fields: Implications for MRI-linac therapy", *Med Phys* , vol. 43, no. 11, pp. 5903–14, pp. 5903-14, 2016.

[38] H. E. Johns, J. R. Cunningham, "The Physics of Radiology, 4th edition", *Charles C. Thomas, Springfield, IL* , 1983.

[39] J. Van Dyk, "The modern technology of radiation oncology",*Medical Physics Publishing, Madison WI* , vol. 2, 1999.

[40] IEC (International Electrotechnical Commission), "Guidelines for radiotherapy treatment rooms design", *IEC Report 61859* , Geneva, 1997.

[41] E. Heath, J. Seuntjens,"Development and validation of a BEAMnrc component module for accurate Monte Carlo modelling of the Varian dynamic Millennium multileaf collimator", *Physics in Medicine and Biology* , vol. 48, no. 24 ,pp. 4045–63, 2004.

[42] J. V. Walle, C. Martens, N. Reynaert, H. M. Thierens, "Monte Carlo model of the Elekta SLiplus accelerator: Validation of a new MLC component module in BEAM for a 6 MV beam",*Physics in Medicine and Biology* , vol. 48, no. 3, pp. 371–85, 2003.

[43] M. S. Huq, J. J. Das, T. Steinberg, J. M. Galvin, "A dosimetric comparison of various multileaf collimators", *Phys Med Biol* , vol. 47, , pp. 159–70, 2002.

[44] D. D. Leavitt et al., "Dosimetric parameters of enhanced dynamic wedge for treatment planning and verification", *Med Dosim* , vol. 20, pp. 177–83, 1997.

[45] J. H. Hubbell, "Electron–positron pair production by photons: A historical overview", *Radiation Physics and Chemistry* , vol. 75, no. 6, pp. 614–23, 2006.

[46] J. A. Wheeler, U. Princeton, W. E. Lamb, U. Columbia, "Influence of Atomic Electrons on Radiation and Pair Production", *Erratum: Phys Rev* , vol. 101, 1956.

[47] J. W. MOTZ, H. A. OLSEN, H. W. KOCH, "Pair Production by Photons", *Rev Mod Phys* , vol. 41, no. 4, pp. 581–639, 1969.

[48] W. Tsai, T. Erber, "Photon pair creation in intense magnetic field", *Phys Rev* , vol. 10, no. 2, pp. 492–499, 1974.

[49] A. H. Compton, "Scattering of X-Rays by a Spinning Electron", *Phys Rev* , vol. 50, no. 10, pp. 878–81, 1936.

[50] S. C. Roy, R. H. Pratt, L. Kissel, "Rayleigh scattering by energetic photons: Development of theory and current status", *Radiation Physics and Chemistry* , vol. 41, no. 4–5, pp. 725–38, 1993.

[51] U. Fano, K. McVoy, W. Albers, R. James "Sauter Theory of the Photoelectric Effect", *Phys Rev* , vol. 116, no. 5, pp. 1147–56, 1959.

[52] I. Kawrakow, E. Mainegra-Hing, D. W. O. Rogers, F. Tessier, B. R. B. Walters "The EGSnrc Code System: Monte Carlo Simulation of Electron and Photon Transport", *National Research Council Canada, Ottawa, Canada; NRCC Report PIRS-701* , pp . 1–323, 2011.

[53] F. H. ATTIX, "Introduction to Radiological Physics and Radiation Dosimetry", *Wiley* , New York, 1986.

[54] D. L. Bailey, J. L. Humm, A. Todd-Pokropek, A. van Aswegen, "Nuclear Medicine Physics: A Handbook for Teachers and Students", *International atomic energy agency* , Vienna, pp. 1–766, 2014.

[55] E. G. Anderson, British Institute of Radiology, Institution of Physics and Engineering in Medicine and Biology, "Central Axis Depth Dose Data for Use in Radiotherapy", *BRITISH JOURNAL OF RADIOLOGY* , London, vol. 25, 1996.

[56] L. Apipunyaspon, S. Srisatit, N. Phaisangittisakul, "Equivalent square formula for determining the surface dose of rectangular field from 6 MV therapeutic photon beam", *J Appl Clin Med Phys* , vol. 14, no. 5, pp. 196–204, 2013.

[57] D. Velkley, D. Manson, J. Purdy "Build-up region of megavoltage photon radiation sources", *Med Phys* , vol. 2, no. 1, pp. 14–19, 1997.

[58] B. Nilsson, A. Montelius, "Fluence perturbation in photon beams under non-equilibrium conditions", *Med Phys* , vol. 13, pp. 191–95, 1986.

[59] K. A. Johansson, L. Q. Mattsson, H. Svensson, "Dosimetric intercomparison at the Scandinavian radiation therapy centres. I. Absorbed dose intercomparison", *Acta Radiol Oncol* , vol. 21, no. 1, pp. 1–10, 1982.

[60] NACP (Nordic Association of Clinical Physics), "Procedures in external radiation therapy dosimetry with electron and photon beams

with maximum energies between 1 and 50 MeV", *Acta Radiol Oncol* , vol. 19, pp. 55–79, 1980.

[61] NACP (Nordic Association of Clinical Physics), "Supplement to the recommendations of NACP (1980): Electron beams with mean energies at the phantom surface below 15 MeV", *Acta Radiol Oncol* , vol. 20, pp. 401–15, 1981.

[62] AAPM (American Association of Physicists in Medicine), "A protocol for the determination of absorbed dose from high energy photon and electron beams", *Med Phys* , vol. 10, pp. 741–71, 1983.

[63] M. S. Huq, R. Nath, "Comparison of IAEA 1987 and AAPM 1983 protocols for dosimetry calibration of radiotherapy beams", *Med Phys* , vol. 18, no. 1, pp. 26–35, 1991.

[64] IPSM (Institute of Physical Sciences in Medicine), "Code of Practice for high-energy photon therapy dosimetry based on the NPL absorbed dose calibration service", *Phys Med Biol* , vol. 35, pp. 1355–60, 1990.

[65] AAPM (American Association of Physicists in Medicine), "Task Group 51: Protocol for clinical reference dosimetry of high-energy photon and electron beams", *Med Phys* , vol. 26, pp. 1487–99, 1999.

[66] I. Kawrakow, "Accurate condensed history Monte Carlo simulation of electron transport: I. EGSnrc, the new EGS4 version", *Med Phys* , vol. 27, pp. 485–98, 2000a.

[67] S. G. Mashnik, "Validation and Verification of MCNP6 against intermediate and high-energy experimental data and results by others codes",*International Conference on Mathematics and Computational Methods Applied to Nuclear Science and Engineering Rio de Janeiro* , RJ, Brazil, Latin American Section (LAS) / American Nuclear Society (ANS), 2011.

[68] F. Salvat, J. M. Fernández-Varea, J. Sempau, "PENELOPE-2011 : A Code System for Monte Carlo Simulation of Electron and Photon Transport", *Workshop Proceedings* , Barcelona, Spain, 4-7 July 2011.

[69] L. Maigne, Y. Perrot, D. R. Schaart, D. Donnarieix, V. Breton, " Comparison of GATE/GEANT4 with EGSnrc and MCNP for electron dose calculations at energies between 15 keV and 20 MeV", *Phys Med Biol* , vol. 56, pp. 811–27, 2011.

[70] J. P. Archambaul, E. Mainegra-Hing, "Comparison between EGSnrc, Geant4, MCNP5 and Penelope for mono-energetic electron beams", *Phys in Med and Biol* , vol. 60. no. 13, pp. 4951–62, 2015.

[71] D. W. O. Rogers, B. Walters, I. Kawrakow "BEAMnrc Users Manual ",*Ionizing Radiation Standards National Research Council of Canada* , Ottawa, NRCC Report PIRS-0509(A)revL, 2013.

[72] B. Walters, I. Kawrako, D. W. O. Rogers, "DOSXYZnrc Users Manual ", *Ionizing Radiation Standards National Research Council of Canada* , Ottawa, NRCC Report PIRS-794revB, 2013.

[73] I. Kawrakow, " Accurate condensed history Monte Carlo simulation of electron transport: II. Application to ion chamber response simulations", *Med Phys* , vol. 27, pp. 499–513. 2000b.

[74] R. Hoppe, T. Phillips, M. Roach, "Leibel and Philips Textbook of Radiation Oncology (Third Edition)", *Saunders* , 2010.

[75] E. Jones and T. David, "History and future technical innovation in positron emission tomography",*J Med Imaging (Bellingham)* , vol. 4, no. 1, 2017.

[76] D. W. O. Rogers, "REVIEW Fifty years of Monte Carlo simulations for medical physics", *Physics in Medicine & Biology* , vol. 51, no. 13, 2006.

[77] E. Poon, F. Verhaegen, " TUFFA105: Limitations of the photon and electron transport algorithms in GEANT4 for radiotherapy applications",*Med Phys* , vol. 32, pp. 2114–2114, 2005b.

[78] A. Fogliata et al., "On the dosimetric behaviour of photon dose calculation algorithms in the presence of simple geometric heterogeneities: Comparison with Monte Carlo calculations", *Phys in Med and Biol* , vol. 52, no. 5, pp. 1363–85, 2007.

[79] W. R. Nelson, H. Hirayama, D. W. O. Rogers "The EGS4 code system", *Stanford Linear Accelerator Center Stanford CA* , , Report SLAC-265, 1985.

[80] C. M. Ma and D. W. O. Rogers, "BEAMDP Users Manual", *Ionizing Radiation Standards National Research Council of Canada* , Ottawa, NRCC Report PIRS-0509(E)revA, 2013.

[81] I. Kawrakow et al., "EGSnrcMP: the multi-platform environment for EGSnrc", 2006.

[82] D. W. O. Rogers, B. A. Faddegon, G. X. Ding, G. X. Ma, J. Wei "BEAM: A Monte Carlo code to simulate radiotherapy treatment units", *Med Phys* , vol. 22, pp. 503–24, 1995.

[83] I. Kawrakow, B. Walters, "Efficient photon beam dose calculations using DOSXYZnrc with BEAMnrc",*Med Phys* , vol. 33, pp. 3046–56, 2006.

[84] H. C. E. McGowan, B. A. Faddegon, C. M. Ma, "STATDOSE for 3D dose distributions",*onizing Radiation Standards National Research Council of Canada* , Ottawa, NRCC Report PIRS-0509(F), 2013.

[85] I. Kawrakow, " The dose visualization tool dosxyz_*show* ", *Ionizing Radiation Standards National Research Council of Canada* , Ottawa, NRCC Report PIRS-0624, 2013.

[86] I. Kawrakow, D. W. O. Rogers, B. R. B. Walters, " Large efficiency improvements in BEAMnrc using directional bremsstrahlung splitting", *Med Phys* , vol. 31, pp. 2883–98, 2004.

[87] E. Mainegra-Hing, I. Kawrakow, "Efficient x-ray tube simulations", *Med Phys* , vol. 33, pp. 2683–90, 2006,

[88] E. S. Ali, D. W. O. Rogers, "Efficiency improvements of x-ray simulations in EGSnrc user-codes using bremsstrahlung cross-section enhancement (BCSE)", *Med Phys* , vol. 34, pp. 2143–54, 2007.

[89] M. Bazalova, H. Zhou, P. J. Keall, E. E. Graves, " Kilovoltage beam Monte Carlo dose calculationsin submillimeter voxels for small animal radiotherapy", *Med Phys* , vol. 36, pp. 4991–99, 2009.

[90] B. R. Walterr, I. Kawrakow. Dwari, "HOWFARLESS" option to increase efficiency of homogeneous phantom calculations with DOSXYZnrc",*Med Phys* , vol. 34, no. 10, pp. 3794–807, 2007.

[91] INTERNATIONAL ORGANIZATION FOR STANDARDIZATION, "Guide to the Expression of Uncertainty in Measurement 2nd edn", Geneva, 1995.

[92] M. S. A. Rani, S. K. A. Rahim, M. R. Kamarudin, T. Peter, S. W. Cheung, and B. M. Saad, "PENELOPE-2006: A Code System for Monte Carlo Simulation of Electron and Photon Transport", *Workshop Proceedings Barcelona* , Spain 4-7 July 2006.

[93] M. B. Chadwick et al, "ENDF/B-VII.0: Next Generation Evaluated Nuclear Data Library for Nuclear Science and Technology" *Nuclear Data Sheets* , vol. 107, no. 12, pp. 2931–3060, 2006.

[94] B. Habib, B. Poumarede, F. Tola, J. Barthe, "Evaluation of PENFAST – A fast Monte Carlo code for dose calculations in photon and electron radiotherapy treatment planning", *Physica Medica* , vol. 26, no. 1, pp. 17–25, 2010.

[95] INTERNATIONAL ATOMIC ENERGY AGENCY, " Measurement Uncertainty: A Practical Guide for Secondary Standards Dosimetry Laboratories", *IAEA-* , Vienna,TECDOC-1585, 2008.

[96] T. K. Yeung, K. Bortolotto, S. Cosby, M. Hoar, E. Lederer, "Quality assurance in radiotherapy: evaluation of errors and incidents recorded over a 10 year period", *Radiotherapy and Oncology* , vol. 74, no. 3, pp. 283–91, 2005.

[97] A. F. Peter at al., A. J. Holden, D. J. Robbins, and W. J. Stewart, "The report of Task Group 100 of the AAPM: Application of risk analysis methods to radiation therapy quality management", *Med Phys* , vol. 43, no. 7, pp. 4209–4262, 2016.

[98] R. Marques, F. Medina, R. Rafii el-Idrissi, "Task Group 142 report: Quality assurance of medical accelerators", *Med Phys* , vol. 36, no. 14, pp. 4197–4212, 2009.

[99] J. Venselaar, H. Welleweerd, B. Mijnheer, "Tolerances for the accuracy of photon beam dose calculations of treatment planning systems", *Radiotherapy and Oncology* , vol. 60, , pp. 191–201, 2001.

[100] A. Bakai, M. Alber, F. Nusslin, "A revision of the γ -evaluation concept for the comparison of dose distributions", *Phys Med Biol* , vol. 48, pp. 3543–53, 2003.

[101] J. Van Dyk, R. B. Barnett, J. E. Cygler, P. C. Shragge, "Commissioning and quality assurance of treatment planning computers", *Int J Radiat Oncol Biol Phys* , vol. 26, pp. 261-73, 1993.

[102] D. A. Low, W. B. Harms, J. A. Purdy, "A technique for the quantitative evaluation of dose distributions", *Med Phys* , vol. 25, pp. 656–61, 1998.

[103] K. R. Hogstrom et al., " Dosimetric evaluation of a pencil-beam algorithm for electrons employing a two-dimensional heterogeneity correction", *Int J Radiat Oncol Biol Phys* , vol. 10, pp. 561–69, 1984.

[104] D. A. Low, W. B. Harms, S. Mutic, J. A. Purdy, "A technique for the quantitative evaluation of dose distributions", *Med Phys* , vol. 25, pp. 656–61, 1998.

[105] D. A. Low, "Gamma Dose Distribution Evaluation Tool" *Journal of Physics Conference Series*, vol. 250, no. 1, pp. 1–12, 2010.

[106] J. Van Dyk, R B. Barnett, J. R. Cygler, P. C. Shragge, "Commissioning and quality assurance of treatment planning computers", *Int J Radiat Oncol Biol Phys* , vol. 26, no. 2, pp. 261–73, 1993.

[107] ICRU Report 42, "Use of computers in external beam radiotherapy procedures with high- energy photons and electrons" *International Commission on Radiation Units and Measurements*, Baltimore, Maryland, USA, 1987.

[108] E. C. McCullough, A. M. Krueger "Performance evaluation of computerized treatment planning systems for radiotherapy: external photon beams", *Int J Radiat Oncol Biol Phys* , vol. 6, pp. 1599–605, 1980.

[109] H. Dahlin, I. L. Lamm, T. Landberg, S. Levernes, N. Ulsø, "User requirements on CT-based computed dose planning systems in radiation therapy", *Acta Radiol Oncol* , vol. 22, pp. 397–15, 1983.

[110] A. Brahme et al., "Accuracy requirements and quality assurance of external beam therapy with photons and electrons", *Acta Oncol* , vol. 1, 1988.

[111] B. Fraass et al., " American Association of Physicists in Medicine Radiation Therapy Committee Task Group 53: quality assurance for clinical radiotherapy treatment planning" *Med Phys* , vol. 25, no. 10, pp. 1773–829, 1998.

[112] ESTRO European Society for Therapeutic Radiology and Oncology, "Quality assurance of treatment planning systems practical examples for non-IMRT photon beams", *Brussels: ESTRO* , vol. 7, 2004.

[113] American Association of Physicists in Medicine, "Radiation treatment planning dosimetry verification", *AAPM Report 55 of Task Group 23 of the Radiation Therapy Committee* , Woodbury, NY: American Institute of Physics, 1995.

[114] WORKING GROUP6 : COMPUTATIONAL DOSIMETRY, 'Standard Monte Carlo Modelling of a Medical Linear Acceleror", France, 2010.

[115] A. Mesbahi and F. S. Nejad, " Monte Carlo study on a flattening filter free 18-MV photon beam of a medical linear accelerator", *Radiation Medicine* , vol. 26, pp. 331–36, 2008.

[116] U. Titt et al., "A flattening filter free photon treatment concept evaluation with Monte Carlo", *Med Phys* , vol. 33, no. 6, 2006.

[117] A. Mesbahi, "Dosimetric characteristics of unflattened 6 MV photon beams of a clinical linear accelerator: A Monte Carlo study", *Applied Radiation and Isotopes* , vol. 65, pp. 1029–1036, 2007.

[118] D. M. Lovelock et al., "A Monte Carlo model of photon beams used in radiation therapy", *Med Phys* , vol. 22, no. 9, pp. 1387–94, 1995.

[119] D. Sheikh-Bagheri et al., " Comparison of measured and Monte Carlo calculated dose distributions from the NRC linac", *Med Phys* , Vol. 27, no. 10, pp. 2256–66, 2000.

[120] D. Sheikh-Bagheri, D. W. O. Rogers, " Sensitivity of megavoltage photon beam Monte Carlo simulations to electron beam parameters", *Med Phys* , vol. 29, pp. 379–90, 2002.

[121] F. Verhaegen, J. Seuntjens, " Monte Carlo modelling of external radiotherapy photon beams", *Phys Med Biol* , vol. 48, pp. 107–64, 2003.

[122] J. Pena et al., "Commissioning of a medical linear accelerator photon beam Monte Carlo simulation using wide-field profiles", *Phys in Med and Biol* , vol. 49, no. 21, pp. 4929–42, 2004.

[123] A. Tzedakis et al., "Influence of initial electron beam parameters on Monte Carlo calculated absorbed dose distributions for radiotherapy photon beams", *Med Phys* , vol. 31, pp. 907–13, 2004.

[124] P. Bjork, T. Knoos, P. Tilson, "Influence of initial electron beam characteristics on Monte Carlo calculated absorbed dose distributions for linear accelerator electron beams", *Phys in Med and Biol* , vol. 47, no. 22, pp. 4019–41, 2002.

[125] S. lin et al., " Monte Carlo simulation of a linear accelerator", *Appl Radiat Isot* , vol. 55, pp. 759–65, 2001.

[126] G. X. Ding, " Energy spectra, angular spread, fluence profiles and dose distributions of 6 and 18 MV photon beams: results of Monte Carlo simulations for a Varian 2100EX accelerator", *Phys Med Biol* , vol. 47, pp. 1025–46, 2002.

[127] B. Libby et al., " Validation of Monte Carlo generated phase-space descriptions of medical linear accelerator", *Med Phys* , vol. 26, no. 8, pp. 1476–83, 1999.

[128] E. Franchisseur, " Thesis: Modélisation et validation de l'accélérateur PRIMUS de SIEMENS par le code Monte Carlo PENELOPE dans le cadre de la Radiothérapie du Cancer", University Nice-Sophia Antipolis, 2007.

[129] International Agency of Energy Atomic (IAEA), " Absorbed Dose Determination in External Beam Radiotherapy : An International Code of Practice for Dosimetry Based on Standards of Absorbed Dose to Water", *IAEA* , Technical Report Series n398, 2000.

[130] L.Blazy-Aubignac, " Thèse de doctorat : Contrôle qualité des systemes de planification dosimetrique des traitements en radiotherapie externe au moyen du code Monte Carlo PENELOPE", University TOULOUSE III – Paul Sabatier, France, 2007.

[131] J. Mazurier, " Rapport CEA : Adaptation du code Monte Carlo PENELOPE pour la métrologie de la dose absorbée: caractérisation des faisceaux de photons X de haute énergie et calcul de facteurs de correction de dosimètres de référence",CEA/Saclay, 2009.

[132] A. Mesbahi, " Effect of wedge filter and field size on photoneutron dose equivalent for an 18 MV photon beam of a medical linear accelerator", *Applied Radiation and Isotopes* , vol. 68, 2010.

[133] B. Caccia et al., " Monte Carlo in radiotherapy: Experience in a distributed computational environment", *Journal of Physics: Conference Series* , vol. 74, 2007.

[134] M. J. Foley, E. Conneely, A. Alexander, G. Stroian, J. Seuntjens, " An investigation into the use of MMCTP to tune accelerator source parameters and testing its clinical application", *Journal of Appl Clin Med Phys* , vol. 14, no. 2, pp. 3–14, 2013.

[135] F. Hasenbalg, M. K. Fix, E. J. Born, R. Mini, I. Kawrakow" VMC++ versus BEAMnrc: A comparison of simulated linear accelerator heads for photon beams", *Med Phys* , vol. 35, pp. 1521–31, 2008.

[136] L. Brualla, M. Rodriguez, J. Sempau, P. Andreo, " PENELOPE/PRIMO-calculated photon and electron spectra from clinical accelerators. Radiation Oncology", *Radiation Oncology* , vol. 14, no. 6, 2019.

[137] J. Sempau, A. Badal, L. Brualla, " A PENELOPE-based system for the automated Monte Carlo simulation of clinacs and voxelized geometries—Application to far-from-axis field", *Med Phys* , vol. 38, pp. 5887–95, 2011.

[138] J. EL Bakkali, A. Doudouh, H. Mansouri, K. Bouyakhlef, L. Baddouh, K. Dahmani, " Investigation of the HDF5 C++ library in development of new phase-space I/O for radiotherapy simulation using Monte Carlo Geant4 code, American Journal of Mathematical and Computer Modelling", *American Journal of Mathematical and Computer Modelling* , vol. 1, pp. 25–31, 2016.

[139] M. Zoubair, T. El Bardouni, O. Allaoui, Y . Boulaich, B. El Bakkari, C. El Younoussi, " Computing efficiency improvement in Monte Carlo simulation of a 12 MV photon beam medical LINAC", *World Journal of Nuclear Science and Technology* , vol. 3, pp. 14–21, 2013.

[140] F. Salvat, J. M. Fernández-Varea, J. Sempau, X. Llovet, " Monte Carlo simulation of bremsstrahlung emission by electrons. Radiation Physics and Chemistry", *Radiation Physics and Chemistry* , vol. 75, pp. 1201–1219, 2007.

[141] B. Walters, I. Kawrakow, " Technical note: Over prediction of dose with default PRESTA-I boundary crossing in DOSXYZnrc and BEAMnrc", *Med Phys* , vol. 34, pp. 647–50, 2007.

[142] S. B. Daryoush, Thesis " Monte Carlo Study of Photon Beams from Medical Linear Accelerators: Optimization, Benchmark and Spectra", Carleton University Ottawa, Canada, 1998.

[143] J. Jayamani, N. A. Z. Mohd Termizi, F. N. Mohd Kamarulzaman, M. Z. Abdul Aziz, " Optimisation of 12 MeV electron beam simulation using variance reduction technique", *Journal of Physics: Conf. Series* , vol. 851, 2017.

[144] M. Mohammed, E. Chakir, H. Boukhal, M. Saeed, T. El Bardouni, " Evaluation of variance reduction techniques in BEAMnrc Monte Carlo simulation to improve the computing efficiency", *Journal of Radiation Research and Applied Science* , vol. 9, pp. 424–30, 2016.

[145] M. Fragoso, I. Kawrakow, B. A. Faddegon, D. S. Timothy, J. I. Chetty, " Fast, accurate photon beam accelerator modeling using beamnrc: A systematic investigation of efficiency enhancing methods and cross-section data", *Med Phys* , vol. 36, pp. 5451–5466, 2009.

[146] I. Kawrakow, " Efficiency of photon beam treatment head simulations", *Med Phys* , vol. 32, pp. 2320–26, 2005.

[147] M. Bencheikh, A. Maghnouj, J. Tajmouati, " Energetic properties investigation of removing flattening filter at phantom surface: Monte Carlo study using BEAMnrc code", *Physics of Particles and Nuclei Letters* , vol. 14, pp. 953–62, 2017.

[148] M. Bencheikh, A. Maghnouj, J. Tajmouati, " Photon beam softening coefficients evaluation for a 6 MeV photon beam for an aluminum slab: Monte Carlo study using BEAMnrc Code, DOSXYZnrc Code, and BEAMDP code", *Moscow University Physics Bulletin* , vol. 72, pp. 263–70, 2017.

[149] J. Cashmore, S. Golubev, J. L. Dumont, M. Sikora, M. Alber, M. Ramtohul, " Validation of a virtual source model for Monte Carlo dose calculations of a flattening filter free linac", *Med Phys* , vol. 39, pp. 3262–69, 2012.

[150] J. Hrbacek, S. Lang, S. Klock, " Commissioning of photon beams of a flattening filter-free linear accelerator and the accuracy of beam modeling using an anisotropic analytical algorithm", *Int J Radiat Oncol Biol Phys* , vol. 80, pp. 1228–37, 2011.

[151] S. F. Kry, O. N. Vassiliev, R. Mohan, " Out-of-field photon dose following removal of the flattening filter from a medical accelerator", *Phys Med Biol* , vol. 55, 2010.

[152] Y. Xiao, S. F. Kry, R. Popple, E. Yorke, N. Papanikolaou, S. Stathakis, " Flattening filter-free accelerators: a report from the AAPM Therapy Emerging Technology Assessment Work Group", *J Appl Clin Med Phys* , vol. 16, 2015.

[153] P. Tsiamas, J. Seco, Z. Han, M. Bhagwat, J. Maddox, C. Kappas, " A modification of flattening filter free linac for IMRT", *Med Phys* , vol. 38, pp. 2342-52, 2011.

[154] D. G. Zhang, V. Feygelman, E. G. Moros, K. Latifi, S. Hoffe, J. Frakes, " Superficial and peripheral dose in compensator-based FFF beam IMRT", *J Appl Clin Med Phys* , vol. 18, pp. 151-56, 2017.

[155] D. R. Zwahlen, S. Lang, J. Hrbacek, C. Glanzmann, S. Kloeck, Y. Najafi, " The use of photon beams of a flattening filter-free linear accelerator for hypofractionated volumetric modulated arc therapy in localized prostate cancer", *Int J Radiat Oncol Biol Phys* , vol. 83, pp. 1655-60, 2012.

[156] M. Sidek Jaafar Ariff, Thesis " Monte Carlo investigations of radiotherapy beams: studies of conventional, stereotactic and unflattened beams", University of Birmingham: School of Physics and Astronomy, Birmingham, United Kingdom, 2010.

[157] D. Georg, T. Knoos, B. McClean, " Current status and future perspective of flattening filter free photon beams", *Med Phys* , vol. 38, pp. 1280-93, 2011.

[158] A. Fogliata, R. Garcia, T. Knoos, G. Nicolini, A. Clivio, E. Vanetti, " Definition of parameters for quality assurance of flattening filter free (FFF) photon beams in radiation therapy", *Med Phys* , vol. 39, pp. 6455-64, 2012.

[159] P. Kuess, D. Georg, H. Palmans, W. Lechner, " Technical Note: On the impact of the incident electron beam energy on the primary dose component of flattening filter free photon beams", *Med Phys* , vol. 43, 2016.

[160] G. Budgell et al., " IPEM topical report 1: guidance on implementing flattening filter free (FFF) radiotherapy", *Phys Med Biol* , vol. 61, pp. 8360-94, 2016.

[161] K.Javedan et al., " Monte Carlo comparison of superficial dose between flattening filter free and flattened beams", *Phys Med* , vol. 30, pp. 503-08, 2014.

[162] R. Shende, G. Gupta, G. Patel, S. Kumar, " Commissioning of TrueBeamTM medical linear accelerator: quantitative and qualitative dosimetric analysis and comparison of flattening filter (FF) and flattening filter free (FFF) Beam", *Clinical Engineering and Radiation Oncology* , vol. 5, pp. 51-69, 2016.

[163] M. N. Meshram, S. Pramanik, C. P. Ranjith, S. K. Gopal, R. Dobhal, " Dosimetric properties of equivalent-quality flattening filter-free (FFF) and flattened photon beams of Versa HD linear accelerator", *J Appl Clin Med Phys* , vol. 17, pp. 358-70, 2016.

Résumé

L'objectif de ce travail est de développer une simulation Monte Carlo pour être utilisée dans le calcul et l'analyse de distribution de doses. Dans ce contexte, nous avons utilisé le code Monte Carlo BEAMnrc. Ce code est à l'origine conçu pour l'application de la dosimétrie en physique médicale.
Grâce au code BEAMnrc, la tête de l'accélérateur linéaire médical, 12 MV SATURNE 43, a été simulée et cette simulation a été validée avec des précisions de 1,5% et 1%, respectivement.
Les techniques de réduction de la variance implémentées dans les deux codes BEAMnrc / DOSXYZnrc ont été utilisées pour augmenter considérablement l'efficacité en gagnant sur le temps de calcul de simulation et en réduisant les erreurs statistiques.
Nous avons également calculé et comparé les distributions de doses pour deux modèles : le premier modèle en utilisant pour la tête de l'accélérateur médical linéaire, un filtre égalisateur et pour le deuxième modèle, aucun filtre égalisateur. Nos résultats ont montré que la Distribution de dose en profondeur, à la profondeur de la dose maximale, pour le cas de la tête de l'accélérateur médical linéaire, sans le filtre égalisateur avait une augmentation du débit de dose et une diminution des doses hors champ pour les faisceaux non aplatis (absence du filtre égalisateur) dans le champ de 10 × 10 cm2.
Enfin, la distribution de la dose a été calculée dans le cas du fantôme d'eau homogène et dans le cas d'existence d'hétérogénéité. Une comparaison de ces deux cas de distributions de dose a été réalisée.

Mots-clés : Monte Carlo ; Distribution de Dose ; BEAMnrc ; Sans Filtre Egalisateur; Techniques de Réduction de la Variance.

Abstract

This work is intended to develop a Monte Carlo simulation, which can be used in the calculation and analysis of distribution doses.
In this context, we have used the MC BEAMnrc code. This code is originally designed for application of dosimetry in medical physics.
The Monte Carlo BEAMnrc code for medical linear accelerator: 12 MV SATURNE 43, has been validated with accuracies of 1.5%and 1% respectively.
The variance reduction techniques implemented in BEAMnrc/DOSXYZnrc codes in parallel calculation to increase importantly the efficiency by gaining the time of simulation and reducing the statistical errors.
Two models on free flattening and free flattening filter modes for medical linear accelerator SATURNE 43 with energy of 12 MV photon mode using the BEAMnrc Monte Carlo user code has been developed. Our results found that percentage depth dose at the depth of maximum dose for free flattening filter mode had an increase in the dose rate and a decrease in out of field doses for unflattened beams with 10 × 10 cm2 field size.
Finally the dose deposition has been calculated in homogeneous and heterogeneous phantom.

Keywords : Monte Carlo; Percentage Depth Dose; BEAMnrc; free flattening filter; Variance ReductionTechniques